Formic Acid Decomposition on Cobalt Surfaces

By

Jeffrey J. Sims

Thesis submitted to the Faculty of Graduate and Postdoctoral Studies in Partial Fulfillment of the Requirements for the Degree of M.A.Sc. in Chemical Engineering

Department of Chemical and Biological Engineering

University of Ottawa

May 2015

Abstract

The decomposition of formic acid proceeds via two principal reaction pathways: dehydration and dehydrogenation. Mechanisms and reaction ratios depend on the nature of the catalysts used. This work provides mechanistic insight into the decomposition of formic acid on Co(0001) and a highly stepped cobalt surface. The catalytic systems were studied in ultra-high vacuum by XPS and temperature programmed desorption. On both surfaces, an overall reaction (1) was observed:

$$2\,HCOOH \rightarrow H_2O + CO + H_2 + CO_2 \qquad (1)$$

The surfaces had differing reaction intermediates, reaction temperatures, and activation energies. On Co(0001), formate, carbon, and hydroxyl are intermediates and the reaction has an activation energy of 44.3 ± 0.6 kJ/mol, pre-exponential factor of 0.7 ± 0.05 mbar/s. On highly stepped cobalt, formate and formyl are intermediates and the reaction has an activation energy of 147.2 ± 2.0 kJ/mol and pre-exponential factor of $10^{11.3\ \pm\ 0.2}$ mbar/s. Desorption energies of observed species and mechanisms of observed reactions are reported.

A detailed description and proof of concept of a PM-IRRAS reactor designed for this thesis is also presented.

Sommaire

La décomposition de l`acide formique se dirige vers deux vois chimique principales : déshydration et déshydrogénation. Les mécanismes et les sélectivités des réactions dépendent de la nature du catalyseur utilisé. Cette étude fournit une connaissance mécanique de la décomposition de l`acide formique sur Co(0001) et sur une surface de cobalt fortement étagée. Les systèmes catalytiques ont été étudiés dans un ultra-vide par spectroscopie de photoélectrons X et désorption contrôlée avec température. La réaction observée sur les deux surfaces est :

$$2\,HCOOH \rightarrow H_2O + CO + H_2 + CO_2 \qquad (1)$$

Les intermédiaires, les températures, et les énergies d`activation pour la réaction ont été différent pour les surfaces. Sur Co(0001), formate, carbone, et hydroxyle, sont les intermédiaires et la réaction ont une énergie d`activation de 44.3 ± 0.6 kJ/mol et un facteur pré-exponentiel de 0.7 ± 0.05 mbar/s. Sur la surface fortement étagée, formate et formyle sont les intermédiaires et la réaction ont une énergie d`activation de 147.2 ± 2.0 kJ/mol et un facteur pré-exponentiel de $10^{11.3\pm0.2}$ mbar/s. Les énergies de désorption des composants observés et les mécanismes sont rapportés.

Un réacteur utilisant spectroscopie de réflexion-absorption infrarouge modulation de polarisation été dessiné pour cette thèse. Une description détaillée et une preuve de concept est donné dans la texte.

Acknowledgments

I would foremost like to thank Javier B. Giorgi for his patience, encouragement, guidance, and belief in me. Javier has given me an opportunity to peer into the world of surface science and fundamental catalysis, while simultaneously allowing me to further my technical and practical knowledge, for this I will be ever grateful.

Thanks to my lab mates especially Cherif Aghiles Ould Hamou, who also works on the UHV vessel. Just having someone to run ideas by, who knows the feeling you have when the resistance of a filament is 0 Ω, and understands when you are running a TPD experiment that you will be in the lab for 12-48 hours. Aghiles you have made the never ending rollercoaster of the UHV experience that much more bearable and I thank you for it.

I would also thank my friend and housemate Sean Wilson for the Timmies trips, conversations, and helpful advice.

Thank you, David J. Mandia for helping me gain a greater understanding of surface chemistry, for the opportunities for collaboration, and for all the sweet pool tips.

I would like to thank my girlfriend, Sarah Oddy for pushing me to work and write, when I just wanted to lie in bed and watch adventure time.

Thanks to my family and friends for believing in me and accompanying me through this journey.

Statement of Contributions of Collaborators

I hereby declare that I am the sole author of this thesis. Cherif Aghiles Ould Hamou assisted with the experimental work for Co(0001) in partial fulfilment of his undergraduate thesis. David J. Mandia assisted with the derivation of the surface reaction on the highly stepped Co surface. I performed all experiments, data analysis and interpretation, and wrote all the chapters presented in this work under the supervision of Dr. Javier B. Giorgi. Dr. Javier Giorgi also provided editorial corrections of this work. Chapters 3 and 4 of this thesis are being prepared for submission to the Journal of Physical Chemistry C and American Chemical Society Catalysis, respectively.

Table of Contents

List of Figures

List of Tables

List of Symbols and Abbreviations

Symbol/Abbreviation	Definition
UHV	Ultrahigh vacuum
TPD	Temperature-programmed desorption
XPS	X-ray photoelectron spectroscopy
UPS	Ultraviolet photoelectron spectroscopy
HREELS	High-resolution electron energy-loss spectroscopy
IRRAS	Infrared reflective adsorption spectroscopy
PM-IRRAS	Photo-modulated infrared reflective adsorption spectroscopy
STM	Scanning tunnelling microscope
LEED	Low-energy electron diffraction
QMS	Quadrupole mass spectrometer
TPR	Temperature programmed reaction
RGA	Residual gas analyzer
$E_{binding}$	Binding energy
E_{X-ray}	X-ray energy
$E_{kinetic}$	Electron kinetic energy
φ	Work function
PSD	Position sensitive device
MCP	Microchannel plate detector
R_{des}	Rate of desorption
v	Vibrational frequency factor
θ_x	Surface coverage of species x

E_a^{des}	Energy of desorption
R	Gas constant (J/mol K)
T	Temperature (K)
β	Heating rate (K/s)
dT	Derivative of temperature
t	Time (s)
P	Pressure
k	Rate constant
A	Pre-exponential factor
E_a	Activation energy
VBA	Visual Basic for Applications
HPLC	High performance liquid chromatography
S^*	Available surface site
IR	Infrared
FTIR	Fourier-transform Infrared
δ	Optical path difference
I	Beam intensity
RAIRS	Reflective adsorption infrared spectroscopy
MSSS	Metal surface selection rule
p-	Perpendicular
s-	Parallel
CF	Conflat
MCT	Mercury Cadmium Telluride

ISA	Industry standard architecture

Chapter 1:

Introduction

1.0 Introduction

With the ever growing population of the earth and increasing standards of living the world's energy consumption is drastically increasing. This energy demand is currently being met by fossil fuels, which are quickly depleting. A hydrogen economy has been considered as a possible solution for this problem. Hydrogen has a very high specific energy (energy by mass), however when compared to conventional fuels, hydrogen has a low energy density (energy by volume). In order for hydrogen to be used as a transport fuel it must be pressurized or liquefied to have a more efficient energy density. Pressurization and liquefaction suffer from an inherent energy loss due to high pressure compression and time spent liquefied, respectively. Chemical storage of hydrogen, that is using hydrogen to create another energy carrier or hydrogen vector, allows for easier handling and transportation. Formic acid is one such hydrogen vector.

Formic acid is a liquid at room temperature with a boiling point and melting point similar to water, making it easily adaptable to conventional infrastructure. Formic acid has a hydrogen density of 53.4 g/L at standard temperature and pressure and a 4.4 wt.% hydrogen content.[1–3] It falls short of the US Department of Energy's 2010 requirement for a hydrogen vector (A possible replacement for gas for mobile applications) to contain 5.5 wt.% hydrogen[1], but its hydrogen density is much higher than other conventional hydrogen storage methods. At 85 mol% formic acid is not flammable and non-corrosive.[1]

Formic acid decomposition is also an important model reaction in catalysis. Formic acid provides an ideal framework for understanding decomposition of small organic molecules, as it is known that formic acid can decompose monomolecularly on metals through (1.1) dehydrogenation and (1.2) dehydration pathways producing CO_2 and H_2 or CO and H_2O[4,5]:

$$HCOOH \rightarrow CO_2 + H_2 \quad (1.1)$$

$$HCOOH \rightarrow CO + H_2O \quad (1.2)$$

The decomposition pathways are especially important for fuel cells designed for direct oxidation of carbon containing fuels, as CO is believed to be a poisoning species for most noble metals which are the main catalysts used in fuel cells.[5] The decomposition of formic acid also holds import to bio-derived fuel upgrading as carboxyls are common reactive groups.[6] Thus, it becomes important to understand the conditions which may favour one pathway over the other. Modern ultrahigh vacuum (UHV, $<10^{-9}$ torr[5]) and surface science techniques have given us a stage to explore these pathways on a molecular level, under well-defined conditions.

The most prominent techniques used for these investigations can be organized into two groups: temperature-programmed desorption (TPD) and surface spectroscopy. TPD techniques are used to identify gas-phase products of surface adsorption/reactions as a function of surface temperature. TPD identifies whether decomposition occurs, the pathway it undergoes, and the selectivity of the reactions. The surface spectroscopy group encompasses photoelectron spectroscopy (i.e., X-ray photoelectron spectroscopy (XPS) and ultraviolet photoelectron spectroscopy (UPS)), high-resolution electron energy-loss spectroscopy (HREELS), and both photo modulated and normal infrared reflective adsorption spectroscopy (PM-IRRAS and IRRAS). The spectroscopy techniques can characterize the intermediates of the reaction and the orientation of the adsorbed molecules relative to the surface. These two groups of techniques are complementary and essential for a complete understanding of a surface reaction. Both XPS and TPD will be explained in detail in the experimental chapter.

1.1 Literature Review

The 2009 annual production of formic acid was 720 000 tons/year.[7] Formic acid is used

as a feedstock in the chemical industry, a preservative for food, and an antibacterial agent.[7] The industrial production of formic acid involves the conversion of methanol and carbon monoxide to methyl formate, which is then hydrolysed to formic acid.

$$CH_3OH + CO \rightleftharpoons HCO_2CH_3 \quad (1.3)$$

$$HCO_2CH_3 + H_2O \rightleftharpoons HCO_2H + CH_3OH \quad (1.4)$$

The dehydrogenation reaction (1.1) produces hydrogen and carbon dioxide, with an entropy of 415.42 $\frac{J}{K\ mol}$ and a Gibbs free energy of -92.6 $\frac{kJ}{mol}$ at 300 K. The dehydration reaction (1.2), producing water and carbon monoxide, has an entropy of 257.5 $\frac{J}{K\ mol}$ and a Gibbs free energy of -4.3 $\frac{kJ}{mol}$ at 300 K. The dehydration pathway becomes favourable ($\Delta G>0$) at temperatures above 283 K, whereas the dehydrogenation pathway becomes favourable at 77 K. Therefore, all else being equal, low temperatures should favour dehydrogenation over the dehydration.

Formic acid decomposes extremely slowly at room temperature without the addition of a catalyst; its rate can be attributed to its high activation energy (107.4 kJ/mol).[8] Due to this activation energy, heterogeneous catalysis is an attractive method for lowering the activation energy and increasing the rate of decomposition. The catalysts that have seen the most attention for formic acid decomposition are platinum[9–15], palladium[15–20], ruthenium[2,14,21–28], rhodium[27,29–36], and nickel[37–45].

Catalytic decomposition of formic acid dates back to the early 2000th century with work by Sabatier[46], with an excellent review by Mars[4] and a more recent UHV specific review by Columbia[5]. These reviews have shown that formic acid usually decomposes in two steps: first the molecular formic acid reacts with the metal surface to produce a surface intermediate, and second, the intermediate decomposes to produce CO, H_2O, CO_2, H_2, O, or C. This two-step

adsorption-reaction decomposition suggests the reaction occurs through a Langmuir-Hinshelwood type mechanism (i.e., two adsorbed molecules reacting). CO, H_2O, CO_2, and H_2 can normally be observed as gas-phase products. O and C on the other hand remain on the surface unless a sufficiently high temperature is achieved, in the case of O, or the surface is exposed to an oxidizing species or sputtered, for C. C and O are products of further decomposition, such as dissociative adsorption of CO, whereas the other products are the classical dehydrogenation and dehydration products. Mars also proposes a third decomposition pathway with formaldehyde as a product but suggests that it is insignificant.

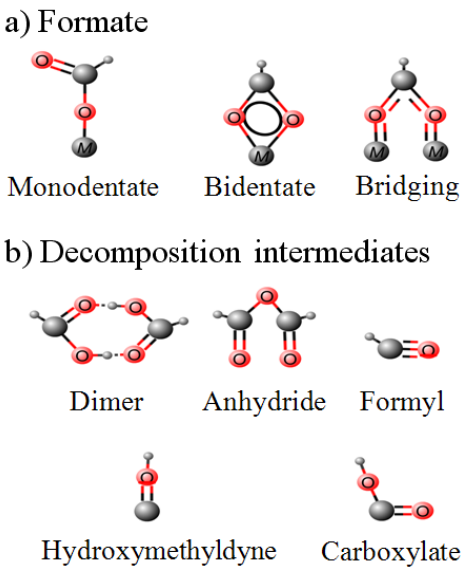

Figure 1.1: Proposed formic acid intermediates on transition metals a) binding orientations of formate, b) decomposition intermediates[5,6,47–50].

The intermediate that is usually identified for the dehydrogenation reaction is usually the adsorbed formate[2,47,51–55,39,37] (HCOO), shown in Figure 1.1a), but there is also some literature supposing that formate is a spectator species[6,50]. Other possible intermediates are shown in Figure 1.1b). Formyl (HCO) and anhydride (OCHOCHO) are both postulated intermediates of the dimer decomposing.[5,6,47–50]

In addition to the dehydration and dehydrogenation reactions there are a number of other

reactions that may occur during or as a result of formic acid decomposition. The most well-known of these reactions is the water-gas shift (WGS) reaction (1.5).

$$CO + H_2O \rightleftharpoons CO_2 + H_2 \quad (1.5)$$

This reaction is a pathway between the products of reaction (1.1) and (1.2). If the goal is to supply hydrogen, then the catalyst must be selective to dehydrogenation and also not facilitate the reverse WGS reaction or the selectivity of dehydrogenation to dehydration may not be as important if one could promote the forward WGS reaction, which is known as the indirect pathway (1.6).

$$HCOOH \xleftarrow{dehydration} CO + H_2O \xleftrightarrow{WGS} CO_2 + H_2 \quad (1.6)$$

Due to the possible presence of the WGS to in formic acid decomposition, it becomes important to understand the reaction. Looking at the WGS reaction intermediates reveals that they are the same as formic acid decomposition, with the exception of the dimer and anhydride.[56–58] Senanayake[59] identified the creation of the formate intermediate to be the rate determining step (rds) in the WGS reaction. The rds for dehydrogenation of formic acid has been identified the decomposition of formate.[4,5] This presents a possible method of separating the reactions on the same catalyst, as the WGS reaction usually occurs between 200-500 ^{o}C[56] and the decomposition of formic acid usually occurs between -44 – 220 ^{o}C[5], depending on the catalyst.

In addition to the aforementioned reactions, another potentially unwanted reaction is the creation of formaldehyde (1.7).

$$2HCOOH \rightleftharpoons CH_2O + CO_2 + H_2O \quad (1.7)$$

Given the various potential species associated with formic acid decomposition it is unlikely that formaldehyde will be seen due to its tendency to disproportionate into formate and methoxy anions.[60]

Further literature, specific to the respective surface, is presented in the introduction section of each of the following chapters concerning the results of this thesis.

1.2 Objectives

The purpose of this thesis is to study, fundamentally, the adsorption and decomposition of formic acid on Co(0001) single crystal and a highly stepped Co single crystal under UHV conditions using XPS and TPD. Experimentally determined surface species are used to corroborate the proposed formic acid decomposition pathways presented herein. Surface coverage calculations based on the TPD and XPS data for the major decomposition products are also reported, as well as desorption energies and pre-exponential factors. Also included is a chapter on the design and proof of concept of a reactor and heat exchanger that was incorporated into the existing UHV vessel. The purpose of the reactor is for both high-pressure and UHV IR measurements, which can be used for further characterization of surface species.

1.3 References

(1) Grasemann, M.; Laurenczy, G. Formic Acid as a Hydrogen Source – Recent Developments and Future Trends. *Energy Environ. Sci.* **2012**, *5*, 8171.

(2) Johnson, T. C.; Morris, D. J.; Wills, M. Hydrogen Generation from Formic Acid and Alcohols Using Homogeneous Catalysts. *Chem. Soc. Rev.* **2010**, *39*, 81–88.

(3) Boddien, A.; Gärtner, F.; Federsel, C.; Sponholz, P.; Mellmann, D.; Jackstell, R.; Junge, H.; Beller, M. CO2-"Neutral" Hydrogen Storage Based on Bicarbonates and Formates. *Angew. Chem. Int. Ed. Engl.* **2011**, *50*, 6411–6414.

(4) Mars, P.; Scholten, J. J. F.; Zwietering, P. The Catalytic Decomposition of Formic Acid. *Adv. Catal.* **1963**, *14*, 35–113.

(5) Columbia, M. R.; Thiel, P. A. The Interaction of Formic Acid with Transition Metal Surfaces, Studied in Ultrahigh Vacuum. *J. Electroanal. Chem.* **1994**, *369*, 1–14.

(6) Xu, J.; Yuan, D.; Yang, F.; Mei, D.; Zhang, Z.; Chen, Y.-X. On the Mechanism of the Direct Pathway for Formic Acid Oxidation at a Pt(111) Electrode. *Phys. Chem. Chem. Phys.* **2013**, *15*, 4367–4376.

(7) Hammes, W. P.; Tichaczek, P. S. The Potential of Lactic Acid Bacteria for the Production of Safe and Wholesome Food. *Z. Lebensm. Unters. Forsch.* **1994**, *198*, 193–201.

(8) Barham, H. N.; Clark, L. W. The Decomposition of Formic Acid at Low Temperatures 1. *J. Am. Chem. Soc.* **1951**, *73*, 4638–4640.

(9) El-Nagar, G. A.; Mohammad, A. M.; El-Deab, M. S.; Ohsaka, T.; El-Anadouli, B. E. Acrylonitrile-Contamination Induced Enhancement of Formic Acid Electro-Oxidation at Platinum Nanoparticles Modified Glassy Carbon Electrodes. *J. Power Sources* **2014**, *265*, 57–61.

(10) Choy M., M.; Hahn, F.; Léger, J.-M.; Lamy, C.; Ortega, J. M. In Situ Fourier Transformed Infrared Reflectance Spectroscopy Study of the Effect of Poly-pDMB Film Modified Platinum Electrodes on the Electrooxidation of Formic Acid. *Thin Solid Films* **2007**, *515*, 3611–3618.

(11) Habibi, B.; Delnavaz, N. Electrocatalytic Oxidation of Formic Acid and Formaldehyde on Platinum Nanoparticles Decorated Carbon-Ceramic Substrate. *Int. J. Hydrogen Energy* **2010**, *35*, 8831–8840.

(12) WANG, Z.; QIU, K. Electrocatalytic Oxidation of Formic Acid on Platinum Nanoparticle Electrode Deposited on the Nichrome Substrate. *Electrochem. commun.* **2006**, *8*, 1075–

1081.

(13) Zhou, X.; Liu, C.; Liao, J.; Lu, T.; Xing, W. Platinum-Macrocycle Co-Catalysts for Electro-Oxidation of Formic Acid. *J. Power Sources* **2008**, *179*, 481–488.

(14) Marković, N. M.; Gasteiger, H. A.; Ross, P. N.; Jiang, X.; Villegas, I.; Weaver, M. J. Electro-Oxidation Mechanisms of Methanol and Formic Acid on Pt-Ru Alloy Surfaces. *Electrochim. Acta* **1995**, *40*, 91–98.

(15) Luo, Q.; Feng, G.; Beller, M.; Jiao, H. Formic Acid Dehydrogenation on Ni(111) and Comparison with Pd(111) and Pt(111). *J. Phys. Chem. C* **2012**, *116*, 4149–4156.

(16) Mazurkiewicz, M.; Malolepszy, A.; Mikolajczuk, A.; Stobinski, L.; Borodzinski, A.; Lesiak, B.; Zemek, J.; Jiricek, P. Pd/MWCNTs Catalytic Activity in the Formic Acid Electrooxidation Dependent on Catalyst Surface Treatment. *Phys. Status Solidi* **2011**, *248*, 2516–2519.

(17) Brandt, K.; Steinhausen, M.; Wandelt, K. Catalytic and Electro-Catalytic Oxidation of Formic Acid on the Pure and Cu-Modified Pd(111)-Surface. *J. Electroanal. Chem.* **2008**, *616*, 27–37.

(18) Mellinger, Z. J.; Kelly, T. G.; Chen, J. G. Pd-Modified Tungsten Carbide for Methanol Electro-Oxidation: From Surface Science Studies to Electrochemical Evaluation. *ACS Catal.* **2012**, *2*, 751–758.

(19) Hosseini, H.; Mahyari, M.; Bagheri, A.; Shaabani, A. Pd and PdCo Alloy Nanoparticles Supported on Polypropylenimine Dendrimer-Grafted Graphene: A Highly Efficient Anodic Catalyst for Direct Formic Acid Fuel Cells. *J. Power Sources* **2014**, *247*, 70–77.

(20) Zhang, L.; Wan, L.; Ma, Y.; Chen, Y.; Zhou, Y.; Tang, Y.; Lu, T. Crystalline Palladium–cobalt Alloy Nanoassemblies with Enhanced Activity and Stability for the Formic Acid Oxidation Reaction. *Appl. Catal. B Environ.* **2013**, *138-139*, 229–235.

(21) Himeda, Y.; Miyazawa, S.; Hirose, T. Interconversion between Formic Acid and H(2)/CO(2) Using Rhodium and Ruthenium Catalysts for CO(2) Fixation and H(2) Storage. *ChemSusChem* **2011**, *4*, 487–493.

(22) Czaun, M.; Goeppert, A.; Kothandaraman, J.; May, R. B.; Haiges, R.; Prakash, G. K. S.; Olah, G. A. Formic Acid As a Hydrogen Storage Medium: Ruthenium-Catalyzed Generation of Hydrogen from Formic Acid in Emulsions. *ACS Catal.* **2014**, *4*, 311–320.

(23) Abdur-Rashid, K.; Clapham, S. E.; Hadzovic, A.; Harvey, J. N.; Lough, A. J.; Morris, R. H. Mechanism of the Hydrogenation of Ketones Catalyzed by Trans-Dihydrido(diamine)ruthenium(II) Complexes †. *J. Am. Chem. Soc.* **2002**, *124*, 15104–15118.

(24) Rice, C. Catalysts for Direct Formic Acid Fuel Cells. *J. Power Sources* **2003**, *115*, 229–235.

(25) Fellay, C.; Dyson, P. J.; Laurenczy, G. A Viable Hydrogen-Storage System Based on Selective Formic Acid Decomposition with a Ruthenium Catalyst. *Angew. Chem. Int. Ed. Engl.* **2008**, *47*, 3966–3968.

(26) Menashe, N.; Shvo, Y. Catalytic Disproportionation of Aldehydes with Ruthenium Complexes. *Organometallics* **1991**, *10*, 3885–3891.

(27) Himeda, Y.; Miyazawa, S.; Hirose, T. Interconversion between Formic Acid and H(2)/CO(2) Using Rhodium and Ruthenium Catalysts for CO(2) Fixation and H(2) Storage. *ChemSusChem* **2011**, *4*, 487–493.

(28) Loges, B.; Boddien, A.; Junge, H.; Beller, M. Controlled Generation of Hydrogen from Formic Acid Amine Adducts at Room Temperature and Application in H2/O2 Fuel Cells. *Angew. Chem. Int. Ed. Engl.* **2008**, *47*, 3962–3965.

(29) Fukuzumi, S.; Kobayashi, T.; Suenobu, T. Efficient Catalytic Decomposition of Formic Acid for the Selective Generation of H2 and H/D Exchange with a Water-Soluble Rhodium Complex in Aqueous Solution. *ChemSusChem* **2008**, *1*, 827–834.

(30) King, R. B.; Bhattacharyya, N. K. Catalytic Reactions of Formate 4. A Nitrite-Promoted Rhodium (III) Catalyst for Hydrogen Generation from Formic Acid in Aqueous Solution. *Inorganica Chim. Acta* **1995**, *237*, 65–69.

(31) Balan, B. K.; Sathe, B. R. Significant Enhancement of Formic Acid Oxidation Using Rhodium Nanostructures. *J. Nanosci. Nanotechnol.* **2012**, *12*, 8994–8998.

(32) Somasunderam, A.; Alper, H. Use of Rhodium on Carbon and 1,3-Bis(diphenylphosphino)propane to Catalyze the Regioselective Hydroformylation of Alkenes with Formic Acid as the Hydrogen Source. *J. Mol. Catal.* **1994**, *92*, 35–40.

(33) Horozova, E.; Dimcheva, N.; Miteva, M.; Jordanova, Z. Rhodium Deposits on Graphite: The Impact of the Graphite Pad on the Electrocatalytic Activity in the Electrooxidation of Formic Acid. *Bulg. Chem. Commun. 40*, 129–136.

(34) Guseva, E. V.; Sokolova, A. V.; Saifutdinov, A. M.; Naumova, A. A.; Polovnyak, V. K. Kinetics of Homogeneous Dehydrogenation of Formic Acid in the Presence of Supramolecular rhodium(III) Complex with P-Functionalized calix[4]resorcine. *Russ. J. Gen. Chem.* **2012**, *82*, 827–834.

(35) De Martinez, M. C.; Beden, B.; Hahn, F.; Lamy, C. Effect of the Bulk Concentration of Formic Acid on the Distribution of the Adsorbates at a Smooth Rhodium Electrode in Acid Medium□: An EMIRS Investiga. *J. Electron Spectros. Relat. Phenomena* **1987**, *45*, 153–160.

(36) Fukuzumi, S.; Kobayashi, T.; Suenobu, T. Efficient Catalytic Decomposition of Formic Acid for the Selective Generation of H2 and H/D Exchange with a Water-Soluble Rhodium Complex in Aqueous Solution. *ChemSusChem* **2008**, *1*, 827–834.

(37) Wang, Z.-L.; Ping, Y.; Yan, J.-M.; Wang, H.-L.; Jiang, Q. Hydrogen Generation from Formic Acid Decomposition at Room Temperature Using a NiAuPd Alloy Nanocatalyst. *Int. J. Hydrogen Energy* **2014**, *39*, 4850–4856.

(38) Assaud, L.; Monyoncho, E.; Pitzschel, K.; Allagui, A.; Petit, M.; Hanbücken, M.; Baranova, E. A.; Santinacci, L. 3D-Nanoarchitectured Pd/Ni Catalysts Prepared by Atomic Layer Deposition for the Electrooxidation of Formic Acid. *Beilstein J. Nanotechnol.* **2014**, *5*, 162–172.

(39) Chang, J.; Feng, L.; Liu, C.; Xing, W.; Hu, X. An Effective Pd-Ni(2)P/C Anode Catalyst for Direct Formic Acid Fuel Cells. *Angew. Chem. Int. Ed. Engl.* **2014**, *53*, 122–126.

(40) Benziqer, J. B.; Schoofs, G. R. Influence of Adsorbate Interactions on Heterogeneous Reaction Kinetics. Formic Acid Decomposition on Nickel. *J. Phys. Chem.* **1984**, *88*, 4439–4444.

(41) Joyner, R. W.; Roberts, M. W. Photoelectron Spectroscopic Investigation of the Adsorption and Catalytic Decomposition of Formic Acid by Copper, Nickel and Gold. *Proc. R. Soc. A Math. Phys. Eng. Sci.* **1976**, *350*, 107–126.

(42) Hirota, K.; Kuwata, K.; Nakai, Y. Infrared Studies of Formic Acid, Chemisorbed on Copper, Nickel and Zinc. *Bull. Chem. Soc. Jpn.* **1958**, *31*, 861–864.

(43) IGLESIA, E. Decomposition of Formic Acid on Copper, Nickel, and Copper-Nickel Alloys I. Preparation and Characterization of Catalysts. *J. Catal.* **1983**, *81*, 204–213.

(44) Haq, S.; Love, J. G.; Sanders, H. E.; King, D. A. Adsorption and Decomposition of Formic Acid on Ni{110}. *Surf. Sci.* **1995**, *325*, 230–242.

(45) IGLESIA, E. Decomposition of Formic Acid on Copper, Nickel, and Copper-Nickel Alloys II. Catalytic and Temperature-Programmed Decomposition of Formic Acid on Cu/SiO2, Cu/Al2O3, and Cu Powder. *J. Catal.* **1983**, *81*, 214–223.

(46) Sabatier, P.; Mailhe, A. The Catalytic Formation of Ether Salts of Formin Acid from Formic Ether. *COMPTES RENDUS Hebd. DES SEANCES L Acad. DES Sci. 154*, 175–177.

(47) Yoo, J. S.; Abild-Pedersen, F.; Nørskov, J. K.; Studt, F. Theoretical Analysis of Transition-Metal Catalysts for Formic Acid Decomposition. *ACS Catal.* **2014**, *4*, 1226–1233.

(48) Huang, J. Y.; Huang, H. G.; Lin, K. Y.; Liu, Q. P.; Sun, Y. M.; Xu, G. Q. The Structures

of Physisorbed and Chemisorbed Formic Acid on Si(111)-7×7. *Surf. Sci.* **2004**, *549*, 255–264.

(49) Bowker, M.; Madix, R. J. XPS, UPS and Thermal Desorption Studies of the Reactions of Formaldehyde and Formic Acid with the Cu(110) Surface. *Surf. Sci.* **1981**, *102*, 542–565.

(50) Chen, Y.-X.; Heinen, M.; Jusys, Z.; Behm, R. J. Bridge-Bonded Formate: Active Intermediate or Spectator Species in Formic Acid Oxidation on a Pt Film Electrode? *Langmuir* **2006**, *22*, 10399–10408.

(51) Rice, C. Catalysts for Direct Formic Acid Fuel Cells. *J. Power Sources* **2003**, *115*, 229–235.

(52) Yin, M.; Li, Q.; Jensen, J. O.; Huang, Y.; Cleemann, L. N.; Bjerrum, N. J.; Xing, W. Tungsten Carbide Promoted Pd and Pd–Co Electrocatalysts for Formic Acid Electrooxidation. *J. Power Sources* **2012**, *219*, 106–111.

(53) Chtaïb, M.; Delrue, J. P.; Caudano, R. Decomposition of HCOOH on Gold Studied by XPS and TDS Spectroscopies and Its Behaviour Under Very Low Energy Electron Excitation. *Phys. Scr.* **1983**, *T4*, 133–137.

(54) Hung, W.-H.; Bernasek, S. L. The Adsorption and Decomposition of Formaldehyde and Formic Acid on the Clean and Modified Fe (100) Surface. *Surf. Sci.* **1996**, *346*, 165–188.

(55) Inglis, H. S.; Taylor, D. Decomposition of Formic Acid on Titanium, Vanadium, Chromium, Manganese, Iron, Cobalt, Nickel, and Copper. *J. Chem. Soc. A Inorganic, Phys. Theor.* **1969**, 2985.

(56) Smith R J, B.; Loganathan, M.; Shantha, M. S. A Review of the Water Gas Shift Reaction Kinetics. *Int. J. Chem. React. Eng.* **2010**, *8*.

(57) Mellor, J. R.; Coville, N. J.; Sofianos, A. C.; Copperthwaite, R. G. Raney Copper Catalysts for the Water-Gas Shift Reaction II. Initial Catalyst Optimisation. *Appl. Catal. A Gen.* **1997**, *164*, 185–195.

(58) JACOBS, G.; PATTERSON, P.; GRAHAM, U.; CRAWFORD, A.; DAVIS, B. Low Temperature Water Gas Shift: The Link between the Catalysis of WGS and Formic Acid Decomposition over Pt/ceria. *Int. J. Hydrogen Energy* **2005**, *30*, 1265–1276.

(59) Senanayake, S. D.; Mullins, D. R. Redox Pathways for HCOOH Decomposition over CeO 2 Surfaces. *J. Phys. Chem. C* **2008**, *112*, 9744–9752.

(60) Peng, X. D.; Barteau, M. A. Acid-Base Reactions on Model MgO Surfaces. *Catal. Letters* **1992**, *12*, 245–253.

Chapter 2:

Experimental

2.0 Experimental

This chapter details the theoretical and practical aspects of the equipment and techniques used in this thesis. The topics that will be broached are the ultra-high vacuum (UHV) vessel, sample preparation, X-ray photoelectron spectroscopy (XPS), scanning tunnelling microscopy (STM), low-energy electron diffraction (LEED), quadrupole mass spectrometry (QMS), and temperature programmed desorption/temperature programmed reaction (TPD/TPR). Details of the experiments conducted will be stated in the chapters concerning results.

2.1 Ultra-High Vacuum Vessel

The UHV vessel is where all the experiments and techniques used in this thesis are conducted. The vessel is specially designed to be able to achieve and remain at UHV pressures, defined as 10^{-9} mbar and lower, with the aid of a series of special pumps. The chamber was custom built by Specs GmbH and RHK. The vessel comprises 3 chambers: the load-lock, analysis, and STM chambers all separated by gate valves. The load-lock is where samples can be loaded in or out of the chamber. The analysis chamber houses the XPS/UPS and LEED instruments, two quadrupole mass spectrometers (also known as residual gas analysers or RGA), an ion sputter gun, and a metal evaporation source. The appropriately named STM chamber contains the atomic force/scanning tunnelling microscope (STM) and a sample storage elevator. Figure 2.1 shows a diagram of the UHV vessel. The vessel is served by two Ion pumps, two turbo pumps, and two accompanying roughing pumps.

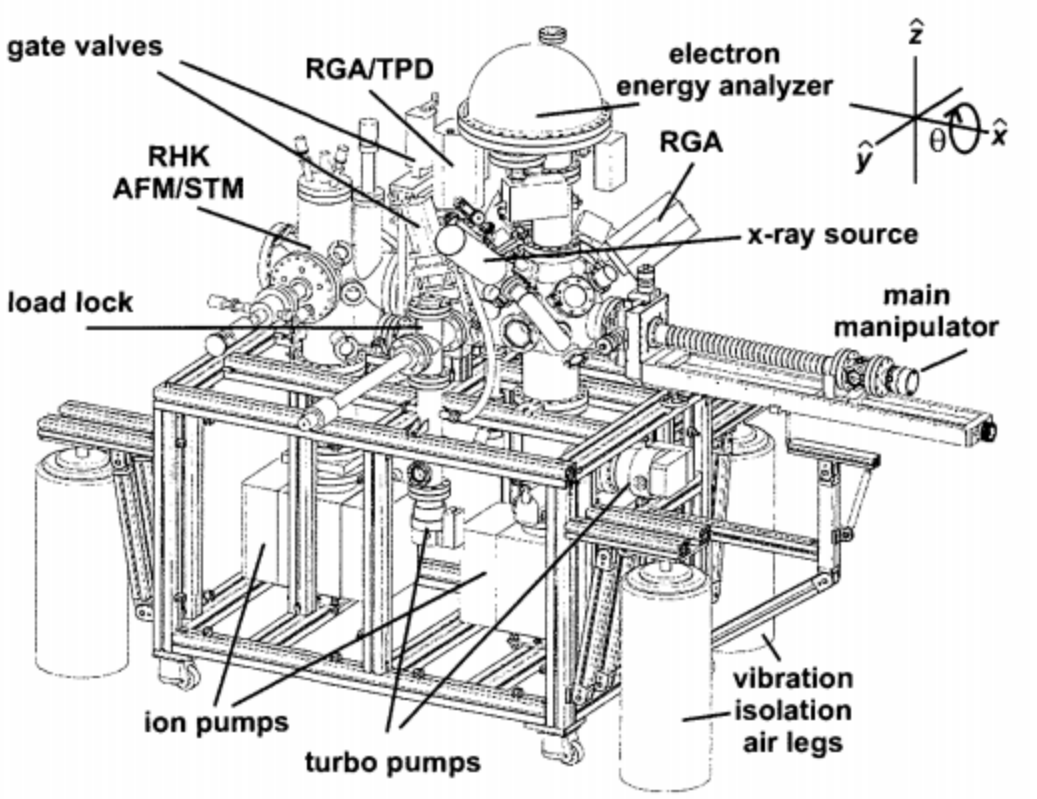

Figure 2.1: Diagram of the UHV vessel with labeled points of interest. Picture provided by Specs GmbH.

The vessel has 3 manipulating arms: the load-lock arm, used to move samples to and from the analysis chamber; the main arm, that is used for the majority of manipulations in the vessel and is used to move the sample between the analysis and STM chamber; and the last arm is a wobble stick (not on a track), used to place samples onto the STM, main arm, or storage elevator. While moving anything in the vessel, special care must be taken to not hit or damage anything within the vessel because most things in the chamber are delicate and not easily replaced. Replacing anything would mean having to open the vessel, which would mean losing UHV and having to re-achieve UHV by "baking out" the whole chamber.

"Baking out" the UHV vessel requires removing almost all electronics and covering the

vessel in special insulating blankets with heating fans. The heating fans heat the vessel up to 113 ^{o}C, while the vacuum pumps run. Heating the vessel degasses the walls of the chambers and allows the pressure in the vessel to decrease. When the vessel has degassed for a sufficient amount of time, usually 24-90 hours, the vessel must be allowed to cool before removing the insulation or else the walls or view ports could crack due to thermal stress. While the vessel is cooling down, all the filaments on the varying instruments should be degassed, which will prevent a pressure spike when the instruments are used.

2.2 Sample Preparation

Sample preparation encompasses a number of elements, including mounting, thermocouples, annealing, and sputtering. This section will illustrate the general steps needed to complete each of these elements.

2.2.1 Mounting

The sample is mounted on a RHK puck that is designed specifically for the manipulators in the vessel to easily handle. The manipulators have either a fork to pick up the puck or a horseshoe shaped sample stage to hold the puck for experimentation. The puck, shown in Figure 2.2, is made of copper and has two groves machined into it so the manipulating forks can hold it and has a horse shoe base so the puck can only be placed in a sample stage in one orientation. There is a hole on the side for thermocouples and a hole at the back for either a grounding base plate to insure no current is passing through the thermocouples or for inducing a charge or bias on the sample depending on the experiment. The thermocouple and grounding base plate holes have two ceramic plates that squeeze the protruding wires to hold them in place as well as to isolate them from the puck. The RHK puck is designed for the STM probe to approach from the

top and as such has three ramps on it that the three-legged STM probe can ‘walk’ down to meet the sample.

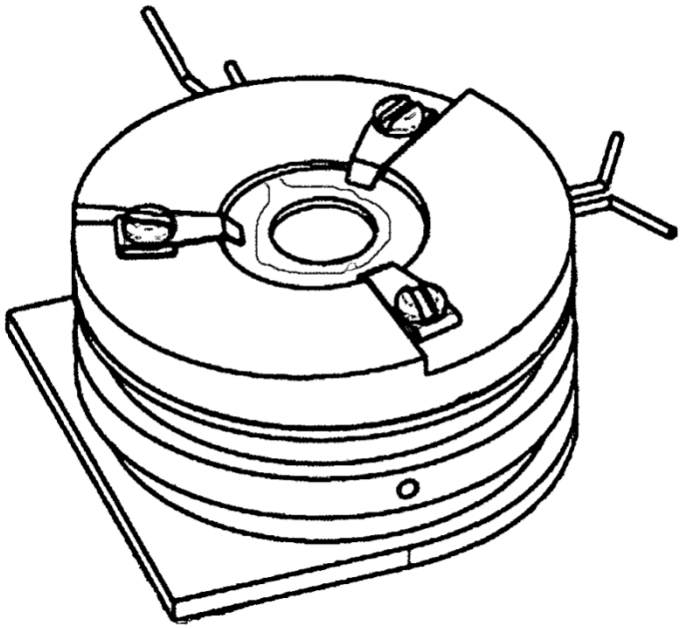

Figure 2.2: RHK sample puck with thermocouple and grounding plate. Picture provided by RHK.

The sample is mounted in the puck using a number of sapphire and molybdenum or tantalum rings to raise the sample up to the required height and to secure the thermocouple to the sample. The choice of supporting rings can result in the sample either being grounded through the thermocouple and electrically isolated from the puck, grounded through the puck, or isolated from everything. The mounting of the sample has a large impact on the experiments conducted: LEED cannot be done on any sample with a sapphire ring on top nor can it be conducted on samples that have poor grounding. If the sample has poor or no grounding, XPS will show unpredictable sample charging giving shifted peaks and STM will not work. If the sample is grounded through the thermocouple without a grounding base plate during the temperature ramp of a TPD experiment the reported temperature will become unreliable due to the current emitted from the heating filament. If the sample is grounded through the puck the electron beam emitted

from the heating filament will heat the sample and puck together resulting in a stronger background and requiring higher filament current.

2.2.2 Thermocouples

The highest temperature the sample can achieve is dependent on a number of factors including the cooling efficiency of the arm, how the sample is mounted and the number of coils the heating filament has. Thermocouples are used to measure the temperature of the samples placed in the system. These thermocouples are K-type, which have a range of -200 to 1350 ^{o}C.[1] K-type thermocouples are made of two types of metal: chromel and alumel.[1] The principle behind the thermocouple is measuring the voltage drop at the junction of the two metals.[1] The voltage change depends on the temperature at the junction, and hence the temperature can be assessed. This means that the junction must be on the sample in order to actually measure the temperature of the sample. The thermocouples are handmade in the lab.

2.2.3 Annealing

The principle behind annealing is to provide enough energy to allow enough mobility to the atoms at the sample surface to allow it to reach an optimal surface orientation.[2] Heating to high temperatures also desorbs any unwanted adsorbed species.[2] In order to achieve high temperatures (above 200 ^{o}C) the main arm needs to be cooled with liquid nitrogen, as the main arm has an iridium film, to improve thermal contact between the sample stage and the liquid nitrogen reservoir, that cannot go above 130 ^{o}C.

The following steps are to set up the chamber for heating:

1. Connect the dry air line to the main arm and turn the dry air line control to about 5

psia. This removes moisture from the thin tubing and prevents the formation of ice inside of the cooling lines when the liquid nitrogen is connected.

2. After the air has been running for about 30 min, disconnect the air line, connect and turn on the liquid nitrogen. Let the liquid nitrogen run for about 1 hour or until the temperature of the arm reaches around -170 ^{o}C.
3. Turn on the SH-100 power supply. Now the system is ready to heat the sample.

Note: it is important to keep the pressure below 10^{-6} mbar, when the analysis and STM chamber are connected.

2.2.4 Sputtering

Sputtering's general concept is simple; it shoots high energy particles at the surface of the sample to remove surface atoms.[3] Since contaminants occupy the top layer, the surface is cleaned in the process. The higher the temperature at which the sputtering takes place the more of the surface is removed. The sputter gun used has a maximum 3 KeV and uses argon as a gas source. The control system, IQE 11-A, for the Ion gun is extremely simple as it only has two knobs, one for the energy level (the kinetic energy given to the Ar particles) and the other for "stand by", "degas", and "operate".

2.3 X-ray photoelectron spectroscopy (XPS)

XPS is a quantitative method to measure the chemical state, elemental composition,

empirical formula and electronic state of the elements at the surface of a material.[4–6] The spectrum is acquired by irradiating the material with a beam of X-rays, generated by an X-ray source, while measuring the kinetic energy and quantity of electrons that escape from the top 1-10 nm of the material. Due to the fact XPS measures freed electrons it requires UHV.

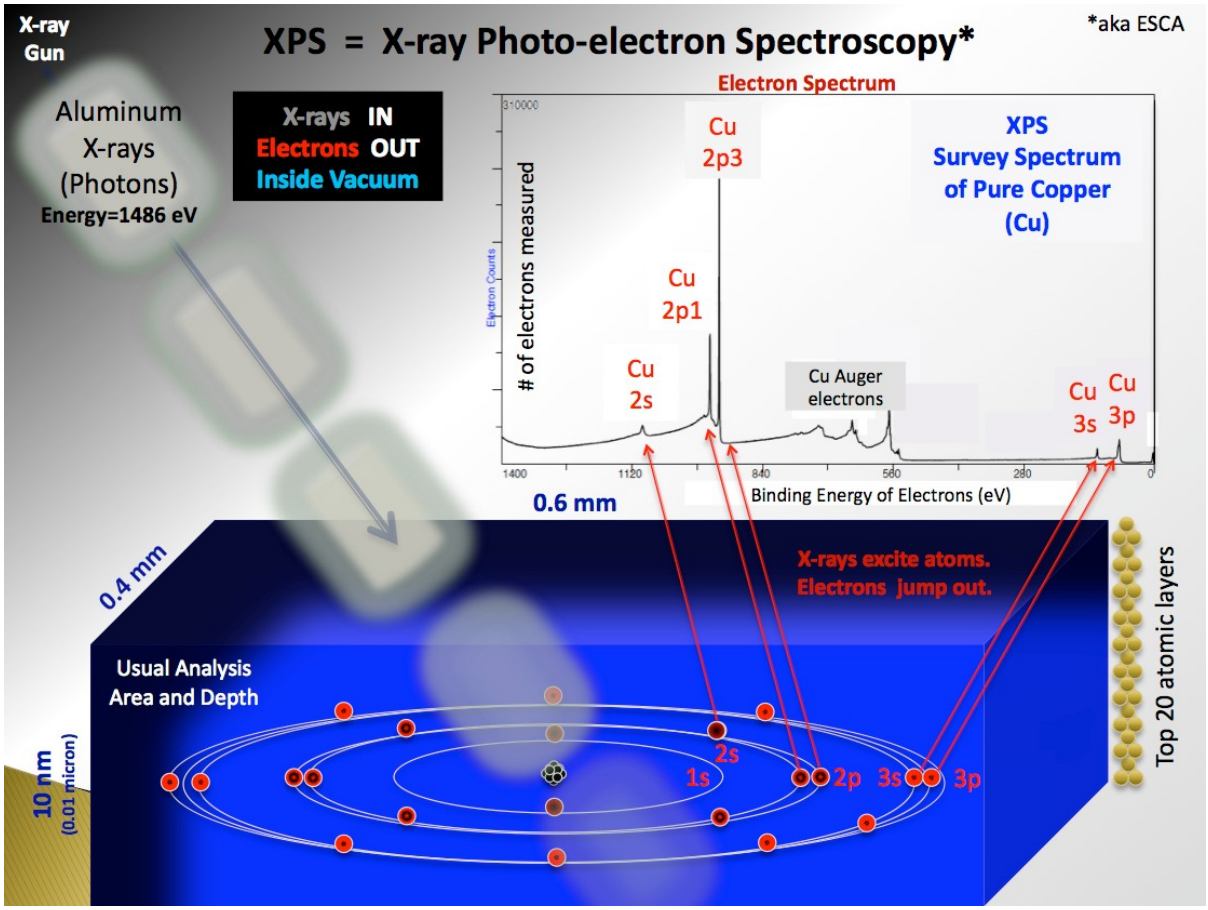

Figure 2.3: Illustration of a XPS performed on Cu, and the respective spectrum.[7]

2.3.1 Theoretical

XPS can measure the binding energy of the electrons, based on the equation[4–6]:

$$E_{binding} = E_{X-ray} - E_{kinetic} - \varphi \quad (2.1)$$

Since the energy of the X-ray ($E_{X\text{-}ray}$) is known and the kinetic energy can be measured ($E_{kinetic}$) and the work function of the instrument (φ) is a constant inherent to the system and as such can be found, the binding energy ($E_{binding}$) can be calculated. The released electrons form a unique spectrum for each element. The binding energy changes due to the interactions with surrounding elements and thus XPS can also show a chemical shift, such as an XPS spectrum of CO_2 vs. elemental C will reveal a slight shift in the carbon peak.

As mentioned above, XPS can only measure freed electrons from the top 1-10 nm of a given material and therefore is used to analyze the surface of a material. XPS can detect all elements except hydrogen and helium, for these elements the "catch probability" (the likelihood of an electron to absorb the energy of an X-ray) is basically zero.[4–6] The lower detection limit for most elements is parts per thousand, but can be decreased to parts per million by either concentrating on the top surface of the material (i.e., tilting the sample, increasing the surface sensitivity) or having a very long collection time.

The main components of the XPS system are:

- A source of X-rays
- An electron energy analyzer
- An electron collection lens
- An ultra-high vacuum (UHV) stainless steel chamber with UHV pumps
- Mu-metal magnetic field shielding

X-rays are generated by bombarding an anode material (Al or Mg) with high-energy electrons. The electrons are emitted from a thermal source, an electrically heated tungsten filament. The photon flux from the X-ray anode is proportional to the electron current contacting the anode.[4–6] The maximum anode current is dependent on the efficiency of heat removal from the anode; for this reason, the X-ray anodes are water-cooled.

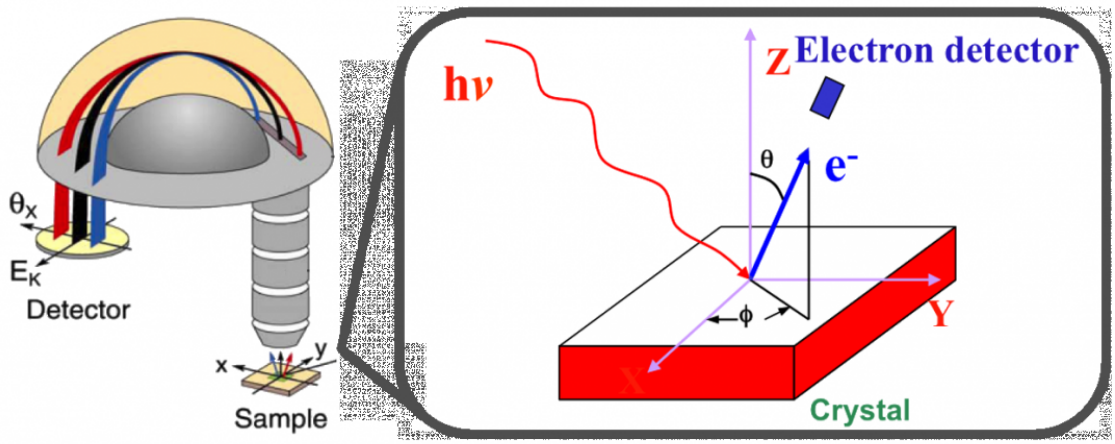

Figure 2.4: Freed electrons traveling through a hemispherical analyzer [8]

There are a number of different types of analysers, but for the sake of simplicity only the type that was used will be explored, which is called a hemispherical electron energy analyser. This type of analyser is used for applications where higher resolution is needed.[4–6] The analyser is composed of two concentric hemispherical electrodes, inner and outer hemispheres as shown in Figure 2.4, each of which is held at a certain voltage. In the analyser, the electrons that pass through are linearly dispersed along the direction connecting the entrance and the exit slits, depending on their kinetic energy. When the two hemispheres are given electric potential, the electric potential and field in the space between the hemispheres can be calculated. The electric field created between the hemispheres is in effect a filter, as it only allows electrons with a certain energy to pass through the entrance slit and into the exit slit where the detector is located; this required energy is called the pass energy.[4–6] The pass energy can be calculated from the electric field created and the geometry of the hemispheres and as such, the pass energy is an important variable in XPS software. Decreasing the pass energy decreases the acceptable energy deviation of the electrons from the desired measured energy, thereby decreasing the number of electrons that are detected, but increases the resolution.

Specifics of the XPS and detailed notes operation of the XPS are given in Appendix I.

2.4 Scanning Tunnelling Microscope

A scanning tunnelling microscope (STM) is an instrument used to image surfaces of materials at the atomic level. Good resolution is considered to be 0.1nm or 1Å lateral and depth resolution.[9] With this resolution, individual atoms can be imaged and manipulated. STM can be used in UHV, air, water, and other fluids, and at temperatures ranging from almost 0 K to a several hundred degrees Celsius.

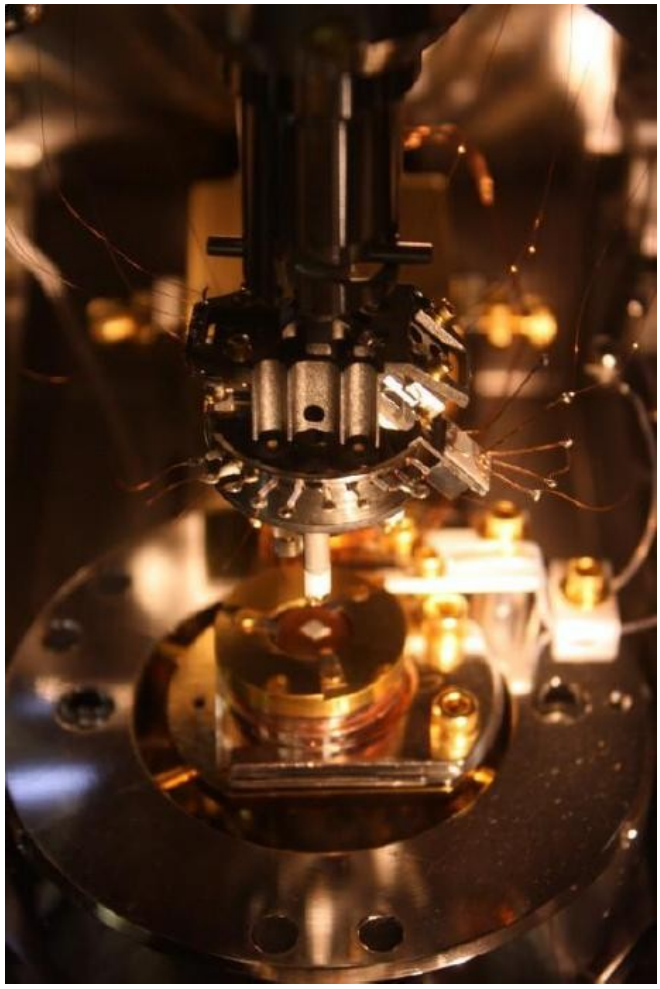

Figure 2.5: a STM tip being lowered to a sample.[10]

STM is founded on the concept of quantum tunnelling. When a conducting tip is brought very near to the surface to be examined and a voltage difference, called a bias, is applied to the surface, with reference to the tip; this allows electrons to tunnel through the vacuum or medium between them. The amount of electrons tunnelling through the tip, called tunnelling current is dependent on the position of the tip, the applied voltage or bias, and the local density of states of the sample.[9] The information is acquired by monitoring the current as the tip scans across the surface; this is displayed as an image. STM requires extremely clean and stable surfaces, sharp tips, vibration control, and refined electronics. The actual steps a STM takes as it takes an image is explained in detail in the next paragraphs.

First, a voltage bias is applied to the sample and the tip is brought close to the surface with the use of a coarse tip control unit, which is subsequently turned off when the tip and sample reach the desired tunnelling current. Once the tip is close the fine tip control mechanism takes over, which allows for complete 3-dimensional movement. The tip is usually about 4-7 Å away from the surface, this is the equilibrium position between attractive and repulsive interactions. Once in the equilibrium position, the bias and the resultant tip's position can be varied in order to obtain the desired resolution, which depends on the experiment. While scanning the tip across the surface the changes in tunneling current are mapped and result in topographic (distance tip travels in the z direction) and current map of the surface.

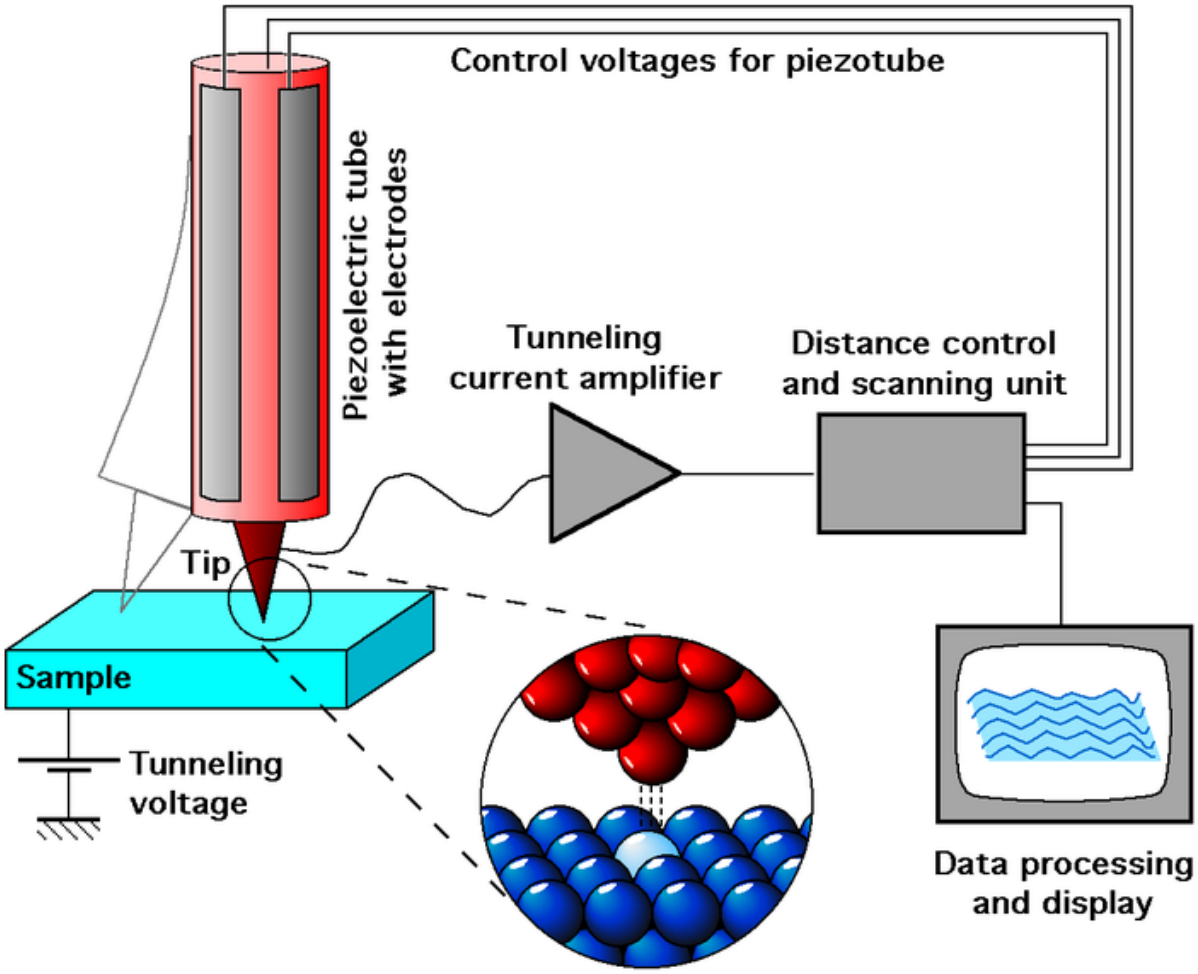

Figure 2.6: STM system diagram.[11]

In addition to scanning across the surface of a sample, data on the electronic structure of a location on a surface can be found by sweeping the voltage and measuring the current at a specific site. This measurement is called scanning tunnelling spectroscopy and results in a plot of local density of states as a function of energy. It is also important to note that all images recorded by STM are greyscale, which means it varies the colour of the image depending on the relative intensity of the data points. For example, it will colour a point red if it has a high current or black if it has a low current. The colours can be changed to give an aesthetically pleasing contrast to emphasize important features.

Detailed notes on the operation of the STM are given in Appendix II.

2.5 Low Energy Electron Diffraction

Low energy electron diffraction (LEED) is a method for determining the surface structure of crystalline materials by bombarding the sample surface with a beam of low energy electrons and observing the diffracted electrons as spots on a fluorescent screen.[12,13] In order to see patterns from a LEED experiment the sample surface must be clean, free from unwanted compounds and atomically smooth; as such the experiments are performed in UHV.

The LEED is used to analyse the spot positions of the diffraction pattern to give information on the symmetry of the surface structure. If in the presence of an adsorbate, the analysis can reveal information about the size and rotational alignment of the adsorbate with respect to the substrate.

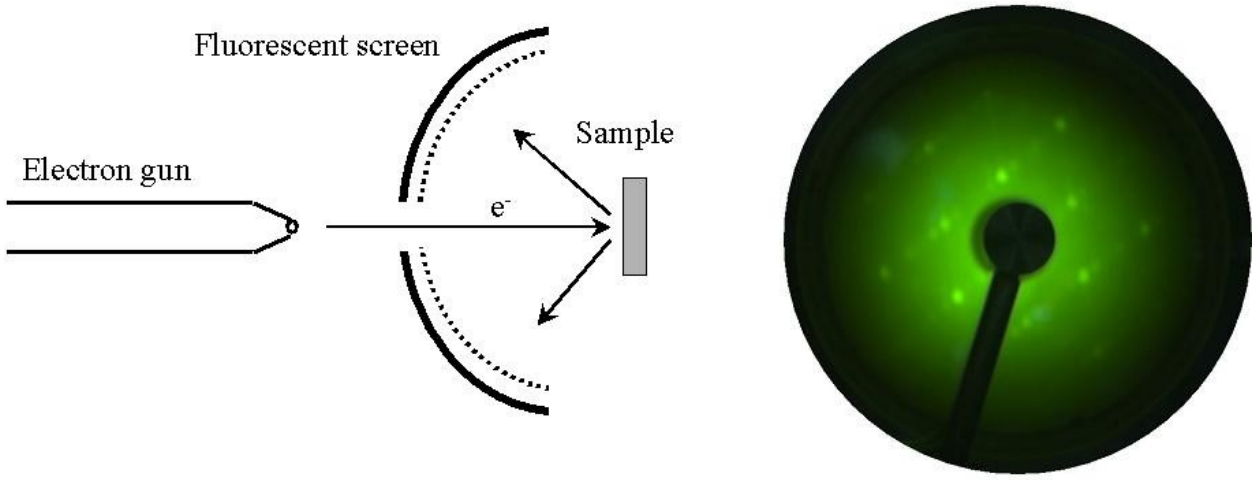

Figure 2.7: LEED experimental setup and LEED pattern of Si(111)[14]

Low-energy electrons (20 -200 eV) have a wavelength around 1-2 Å[12,13], which is less

than the interatomic distance of solids allowing for the observation of diffraction patterns with structural information to be obtained. Upon penetrating the surface, primary electrons (electrons emitted from the electron gun) will lose kinetic energy due to inelastic scattering processes such as plasmon-and phonon excitations and electron-electron interactions. When the nature of the inelastic processes is not important they are treated by assuming an exponential decay of the electron beam intensity. For low energy electrons the penetration is only a couple atomic layers and the deeper the electrons penetrate the less they contribute to the diffraction pattern, which is gives LEED a very high surface sensitivity;[12,13] Making LEED an ideal technique to confirm if a sample surface is clean.

The diffraction pattern is caused by what is known as kinematic diffraction. Kinematic diffraction is when electrons impacted on an ordered crystal surface and are elastically scattered only once. The actual pattern is caused by constructive interference of the electrons to form bright spots on the fluorescent screen.[12,13]

Using LEED, it becomes possible to identify what is known as a superstructure. A superstructure is an adsorbed species that forms a well ordered lattice on top of a samples surface. The superstructure can only be a couple of atomic layers deep or the LEED will only detect the top layer. Knowing the underlying surface's LEED pattern it becomes possible to identify the pattern due to the superstructure. The symmetry and rotational alignment of the superstructure can be found with respect to the surface.[12,13]

2.6 Quadrupole Mass Spectrometers

Quadrupole mass spectrometer (QMS), also known as a residual gas analyser, is a technique that allows for the identification of gaseous chemical species by filtering ions based on their mass to charge ratio (m/z).[15–17] In UHV QMS is mainly used for two reasons; identifying leaks in the chamber and Temperature Programmed Desorption which will be explained later. QMSs are composed of four main parts:

- Ion source or ionizer: ionizes the gas producing positive ions
- Quadrupole mass filter: filters ions
- Ion detector or current collector: collects the ions that pass through the filter producing a current
- Electronics that control the parameters of the filter

The ion source creates ions through electron bombardment, usually using a tungsten filament.[15–19] A fraction of the gas gets ionized by the electrons and makes a fragmentation pattern, which is when the parent molecule fragments into smaller pieces. This fragmentation pattern depends on the chemical species and the ionizing energy[19], this allows for identification of disparate chemical species. For example, carbon monoxide and nitrogen gas both have a molecular weight of around 28 amu, meaning the parent molecule will have a m/z of 28. Without fragmentation it would be impossible to distinguish the two but carbon monoxide will have carbon, 12 m/z, and oxygen, 16 m/z, in its fragmentation pattern where as nitrogen gas will only have nitrogen, 14 m/z.[20] Not only with the each chemical species fragment differently, they will also ionize in different amounts depending on their ionization cross section.[19]

The quadrupole mass filter is composed of 4 parallel metal rods in a square configuration, as shown in Figure 2.8. The rods are put under a combination of DC and AC voltages. The rods that are opposite each other are connected and thus share the same voltages. The two sets of rods are put under opposite DC voltages giving one set a positive over all voltage and the other negative. These 4 poles induce an electric field that ultimately filters ions based on their m/z.

The positive rods act as a high pass filter, meaning they filter out low mass to charge ions and allow high m/z ions pass through. The DC voltage applied naturally repulses the ions as both have like-charges, but as the AC voltage changes from positive to negative and overcomes the DC voltage the rods overall charge changes to negative for a short period of time. This change of charge undergone by the rod causes the ions to change their trajectory to move toward the rod. The rods are constantly changing overall charge and results in the ions moving in a wave like motion. If the ions that have low mass to charge ratio have greater mobility and respond faster to changes in polarity.[15–18] Thus, ions under the specific m/z that desired will have an unstable pathway and collide with the rods, neutralizing the ions. The negative rods are a low pass filter, meaning they filter out high mass to charge ions. The principle of operation is the same as that of the positive high pass filter; relying on the mobility of the lower m/z ions. The difference being the natural trajectory of the ions is towards the rods, due to the negative DC voltage, and not through the filter.[15–18] Thus, the larger mass to charge ions respond weakly to the voltage change and their momentum gives them an unstable path through the filter. With both the positive and negative sets of rods, high and low pass filters working in tandem it becomes possible to make a "window" that allows only a single mass over charge ratio through the filter. The resolution of the QMS used in this thesis is ~0.8 m/z.

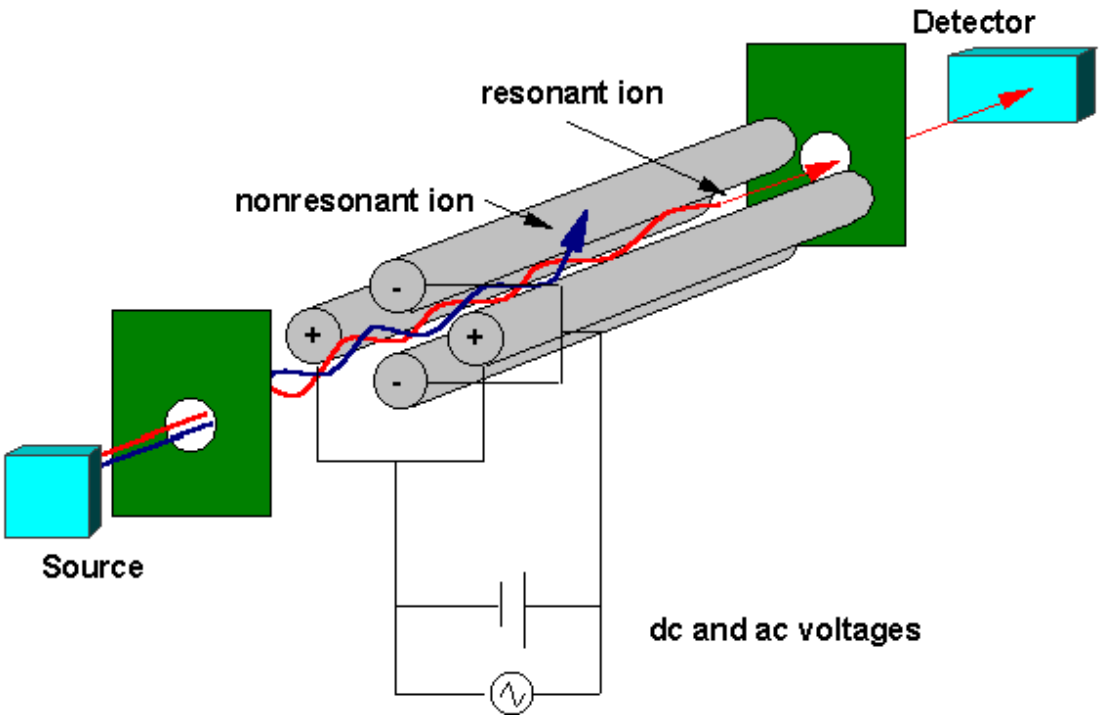

Figure 2.8: Schematic of a quadrupole mass filter[21]

There are a number of different detectors for QMS, but for the sake of brevity only the one used in this thesis will be explained, which is a microchannel plate detector (MCP). MCP detector is a 2mm thick plate with an array of channels, approximately 10 microns in diameter and spaced 15 microns apart that is put under negative voltage to attract the positive ions. The channels are parallel to each other and are enter ~8^{o} from normal. The channels are continuous dynode electron multipliers, which when an ion impacts the side of one of the channels induces a cascade affect, which propagate through the channels, multiplying the signal by several orders of magnitude. The propagated electrons are then collected by a positively charged anode plate creating a current. This current is proportional to the amount of ions that are neutralized.[19] Knowing that the fragmentation pattern and amount of gas ionised depends on the chemical species and that the current is proportional to the amount of ions neutralised it becomes possible to identify, separate, and quantify the chemical species observed in a QMS.

2.6.1 Practical Considerations

The QMS is a Pfeiffer Vacuum Prisma 200. It has a measureable range of 1 to 200 m/z, tuneable ionization parameters, and an operating pressure range of $1 \times 10^{-4} - 1 \times 10^{-14}$ Torr. The accompanying software package is called "QuadStar" or QS. In order to actually take a spectrum the executable file "Measure" must be opened. Once opened the software will automatically find and connect to the QMS, if the QMS is connected to the computer. The software has a number of different operational modes; Scan which scans a range of masses specified by the user; Multiple Ion Detection or MID which measures individual m/z ratios specified by the user; and Multiple Concentration Detection or MCD which attempts to automatically identify, separate, and quantify the components in the gas observed. The scan function is mainly used when trying to identify major m/z ratios for compounds and as an indicator of the UHV vessels background composition. The MID mode is used when the major m/z ratios are known for a set of gasses and are to be observed. MCD requires an incredible amount of non-trivial calibration and was never used in this work.

In order to quantify the data the fragmentation pattern of each molecular species must be taken using the same QMS that the data is taken from because each QMS will produce a slightly different fragmentation pattern that will have a large impact on the quantification process. Once the fragmentation patterns are known the separating and identification of molecular species that share m/z ratios becomes possible but the process can long and difficult if there are multiple species that share m/z ratios. The process may not be possible for some molecular species, if the sensitivity factor (factor to account for differing ionization cross-sections) cannot be found and one does not have the special set-up to test for the sensitivity factor.

2.7 Temperature Programmed Desorption

There are a number of different techniques for studying surface reactions that use "temperature programmed" to delineate processes with disparate activation parameters. These techniques are applied to a system under UHV conditions in which a chemical species is adsorbed to a surface and a heating temperature programmed, usually a linear ramp, induces either desorption or a reaction; known as Temperature Programmed Desorption (TPD) or Temperature Programmed Reaction (TPR), respectively. Although TPD and TPR have different names and observe different phenomenon there is no practical difference between the two.

The experiment is quite simple, one or more chemical species are adsorbed onto a sample surface at a relatively low temperature. Then the sample is heated to give a linear temperature ramp, usually between 2-10 K/s[22–25], while monitoring the species that are evolving from the surface. Our choice of detector for monitoring the chemical species is a QMS. The detector is usually differentially pumped, or in our case it is encased in a bulb made of either glass with a small hole on the bottom that is 1 mm in diameter, as shown in Figure 2.9. The sample surface is placed as close as possible to the hole in the bulb, so as to ensure that the majority of what is evolved from the surface is measure by the QMS. The QMS usually measures multiple m/z but for the simplest experiments may measure only one.

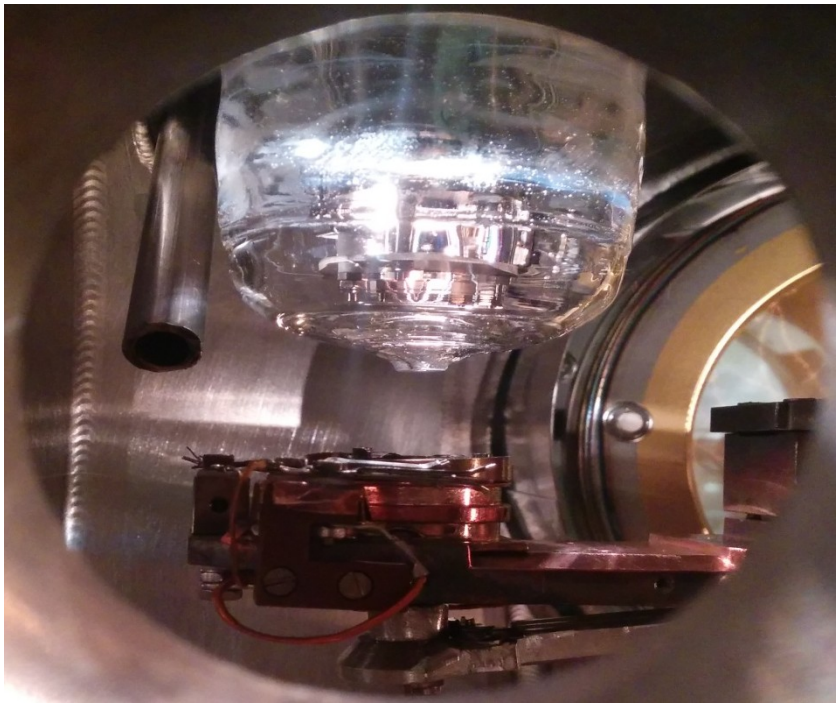

Figure 2.9: Operating QMS encased in a glass bulb, with a Pt(111) sample mounted in a sample puck on the sample stage of the main manipulating arm.

The resulting QMS spectrum will be a current vs. temperature plot. As aforementioned the current of the QMS is proportional to the pressure and therefore proportional to the rate of desorption. The temperature of the desorption peak is related to how strongly the species is bound to the surface.[22–25] From these it is possible to calculate the pre-exponential factor and activation/desorption energy of the observed reaction/desorption.

The general form of the rate of desorption of a surface species is given by:[22–25]

$$R_{des} = v\,\theta^{x}\,\mathrm{e}^{\frac{-\mathrm{E_a^{des}}}{\mathrm{RT}}} \qquad (2.2)$$

Where R_{des} is the desorption rate, v is the vibrational frequency factor, θ is the surface coverage of the desorbing species, x is the order of desorption, $\mathrm{E_a^{des}}$ is the energy of desorption, and T is temperature.

With the introduction of a linear temperature ramp in a TPD experiment additional

parameters can be added:[22–25]

$$T = T_o + \beta t \qquad (2.3) \qquad dT = \beta t \qquad (2.4)$$

Where T_o is the initial temperature, β is the temperature increase per second, and t is time in seconds.

After quantification of the current measured by the QMS, P(T), it is equal to the rate of decrease of surface coverage of the adsorbed species giving:

$$P(T) = -\frac{d\theta}{dT} = \frac{v\,\theta^x}{\beta}\, e^{\frac{-E_a^{des}}{RT}} \qquad (2.5)$$

From this it is possible to find the Energy of desorption and vibrational frequency factor for an adsorbed species.

For TPR a mechanism and rate determining step must be found or determined in order to calculate the pre-exponential factor and activation energy.[22–25] Once a rate determining step is found the rate constants can be calculated for every measured temperature. Using multiple surface coverages of the chemical species, the rate constants dependence on temperature, $k = A\, e^{\frac{-E_a}{RT}}$, and possible dependence on surface coverage[22–25] it is possible to find the activation energy and pre-exponential factor. By plotting ln (k) at the same surface coverage for a number of different exposures of the molecular species, vs. the temperatures at which the surface coverages occur, the slope of the line will be $\frac{-E_a}{RT}$ and the intercept will be ln A.[22–25]

2.7.1 Practical Considerations

Despite the simplicity of this experiment it is extremely hard to get reliable, clear, and uncontaminated results. This experiment is a very long day of collecting data. First the sample must be cleaned and cooled down to the temperature needed to dose the chemical species, usually as low as possible (i.e., 120 -130 K). Then the gas manifold used to dose the chemical

must be able to hold a constant pressure for at least 30 minutes to insure there is no external contaminates. These contaminates can modify or completely change the interpretation of a TPD/TPR. Then the lowest dosage of chemical is introduced to the chamber. The position of the sample during this period of time is crucial for reproducibility, as the position of the sample will have immense effect on surface coverage, so the sample must always be in the same place when dosing. The sample is then moved into position below the QMS, the QMS is turned on and recording the m/z of interest. The linear temperature ramp program is then started, in which the ramp rate and the process control parameters can be modified and records the temperature vs. time. The temperature ramp program was originally programmed in LabView by Javier B. Giorgi then modified by Richard G. Green, and then I reprogrammed and optimised for a lower initial temperature and higher ramp rate. Once the temperature has reached the maximum temperature in the program the sample must be cleaned again, usually flashing to a high temperature. The surface is checked by XPS or LEED to ensure it is clean and then the sample must cool again to the temperature it was previously dosed at and the next lowest dosage is introduced. This process continues until all desired dosages are done. One cool-dose-run-clean cycle takes about 1 1/2 hours and the number of differing exposures is usually 8 to 10. If there is a problem with the temperature ramp, such as the ramp is not linear, or the sample is not grounded properly the run must be repeated.

Once the actual experiment has been conducted, the QMS file and temperature file must be correlated. This is done by a VBA macro originally programmed by Richard G. Green and then I reprogrammed it to work with a newer version of excel and to incorporate multiple m/z ratios. This macro takes both files and plots the QMS current vs. a calculated temperature taken from the temperature ramp. Then the process of quantifying the QMS data can start. Once all of

the QMS data has been quantified the analysis of the reaction/desorption rates can occur.

2.8 References

(1) Park, R. M.; Hoersch, H. M. *Manual on the Use of Thermocouples in Temperature Measurement*; ASTM International, 1981.

(2) Callister, W. D.; Rethwisch, D. G. *Fundamentals of Materials Science and Engineering: An Integrated Approach*; John Wiley & Sons, 2012.

(3) Sigmund, P. Mechanisms and Theory of Physical Sputtering by Particle Impact. *Nucl. Instruments Methods Phys. Res. Sect. B Beam Interact. with Mater. Atoms* **1987**, *27*, 1–20.

(4) McIntyre, N. S.; Cook, M. G. *Surface Analysis Techniques for Metallurgical Applications*; ASTM International, 1976.

(5) Barr, T. L. *Modern ESCAThe Principles and Practice of X-Ray Photoelectron Spectroscopy*; CRC Press, 1994.

(6) Azoulay, J. Photoelectron Spectroscopy—principles and Applications. *Vacuum* **1983**, *33*, 211–213.

(7) Crist, B. V. File:XPS PHYSICS.png http://en.wikipedia.org/wiki/File:XPS_PHYSICS.png (accessed Apr 9, 2015).

(8) Angle-Resolved Photoemission Spectroscopy | Shen Laboratory https://arpes.stanford.edu/research/tool-development/angle-resolved-photoemission-spectroscopy (accessed Apr 9, 2015).

(9) Chen, C. J. *Introduction to Scanning Tunneling Microscopy*; OUP Oxford, 2008.

(10) Bazylewski, P. Facilities http://physics.usask.ca/~chang/homepage/lab/lab.html (accessed Apr 9, 2015).

(11) Schmid, M. File:ScanningTunnelingMicroscope schematic.png http://en.wikipedia.org/wiki/File:ScanningTunnelingMicroscope_schematic.png (accessed Apr 9, 2015).

(12) Van Hove, M. A.; 1947-; Tong, D. S. Y.; 1942-. Surface Crystallography by LEED. **1979**.

(13) Prigogine, I.; Rice, S. A. *Advances in Chemical Physics, Volume 20*; John Wiley & Sons, 2009.

(14) Surface Analysis Chamber – Nuclear and Radiation Physics http://fys.kuleuven.be/iks/nvsf/experimental-facilities/surface-analysis-chamber (accessed Apr 12, 2015).

(15) Dawson, P. H. *Quadrupole Mass Spectrometry and Its Applications*; Elsevier Science, 2013.

(16) Chernushevich, I. V; Loboda, A. V; Thomson, B. A. An Introduction to Quadrupole-Time-of-Flight Mass Spectrometry. *J. Mass Spectrom.* **2001**, *36*, 849–865.

(17) Miseki, K. Quadrupole Mass Spectrometer. US5227629 A, July 13, 1993.

(18) Miller, P. E.; Denton, M. B. The Quadrupole Mass Filter: Basic Operating Concepts. *J. Chem. Educ.* **1986**, *63*, 617.

(19) Nakao, F. Determination of the Ionization Gauge Sensitivity Using the Relative Ionization Cross-Section. *Vacuum* **1975**, *25*, 431–435.

(20) US Department of Commerce, N. NIST Standard Reference Database 1A v14.

(21) Definition of quadrupole_mass_spectrometry - Chemistry Dictionary http://www.chemicool.com/definition/quadrupole_mass_spectrometry.html (accessed Apr 13, 2015).

(22) Kolasinski, K. K.; Kolasinski, K. W. *Surface Science: Foundations of Catalysis and Nanoscience*; John Wiley & Sons, 2012.

(23) Woodruff, D. P.; Delchar, T. A. *Modern Techniques of Surface Science*; Cambridge University Press, 1994.

(24) Falconer, J. L.; Schwarz, J. A. Temperature-Programmed Desorption and Reaction: Applications to Supported Catalysts. *Catal. Rev.* **2007**, *25*, 141–227.

(25) Miller, J. B.; Siddiqui, H. R.; Gates, S. M.; Russell, J. N.; Yates, J. T.; Tully, J. C.; Cardillo, M. J. Extraction of Kinetic Parameters in Temperature Programmed Desorption: A Comparison of Methods. *J. Chem. Phys.* **1987**, *87*, 6725.

Chapter 3:

Adsorption and Decomposition of Formic Acid on Co(0001)

3.0 Decomposition of Formic acid on Cobalt (0001)

Jeffrey J. Sims[a,b], Cherif Aghiles Ould Hamou[a,c], Javier B. Giorgi[a,d]

[a]Centre for Catalysis Research and Innovation, [b]Department of Chemical and Biological Engineering, [c]Department of Physics, [d]Department of Chemistry,
University of Ottawa, 10 Marie Curie Pvt., Ottawa, Ontario, Canada. K1N 6N5.

3.1 Abstract

Formic acid can decompose to CO and H_2O or H_2 and CO_2, through the dehydration or dehydrogenation pathways, respectively. The mechanisms and selectivities of these reactions depend on the nature of the catalysts used. This work provides mechanistic insight into the decomposition of formic acid on Co(0001). The adsorption and decomposition of formic acid on a Co(0001) single crystal of cobalt was studied in ultra-high vacuum by XPS and temperature programmed desorption.

Formic acid adsorbs molecularly on the surface below 160 K. Partial decomposition through the dehydration pathway occurs at 140 K. At 160 K decomposition of formic acid into formate is dominant. The dehydration reaction occurs again at 236 K when part of the dissociated formic acid associatively desorbs and reacts to form CO and H_2O. At 415-450 K CO, CO_2, and H_2 are observed desorbing from the surface in a 1:1:1 ratio. All H_2O observed is equal to the quantity of CO produced. The fact that the amount of H_2O and CO is equivalent and the presence of the 1:1:1 desorption ratio at 415-450 suggests that part of the formic acid adsorbed undergoes a bimolecular reaction and the rest follows the dehydration reaction. A full mechanism for the bimolecular reaction is proposed for which the measured parameters are: activation energy = 44.3 ± 0.6 kJ/mol, pre-exponential factor = 0.70 ± 0.05 mbar/s, an order of -1 with respect to the surface coverages of formate and carbon, and a 0^{th} order with respect to the hydroxyl.

3.2 Introduction

The adsorption and decomposition of formic acid on transition metal surfaces has been the subject of many studies. Formic acid has garnered this interest for a number of reasons. Formic acid decomposition possesses similar intermediates as the water-gas shift reaction, methanol oxidation, and they are likely present in oxidations of large organic molecules and steam reforming reactions. Formic acid also has been purposed as a hydrogen vector for mobile application. Formic acid has been used as a model molecule for characterizing catalyst surfaces because it is a simple molecule that has two known decomposition pathways producing either CO_2 and H_2 or CO and H_2O, known as the (3.1) dehydrogenation and (3.2) dehydration, respectively.

$$HCOOH \rightarrow CO_2 + H_2 \quad (3.1)$$

$$HCOOH \rightarrow CO + H_2O \quad (3.2)$$

Single crystal investigations of formic acid on transition metal surfaces have shown orientation-dependent reaction behaviour, for example on Pt(111) formic acid decomposes purely through the dehydrogenation reaction[1,2] and on Pt(100), formic acid does not react.[3] Formic acid has also been suggested to undergo a bimolecular decomposition pathway on Cu[4–6], Ru[4], Ni[4,6–8] surfaces in addition to, or instead of, the dehydrogenation and dehydration reactions.

Despite cobalt's prevalence as a water-gas shift[9] and methanol oxidation[10] catalyst, as well as an additive to increase performance and stability[11–19] of direct formic acid/methanol fuel cell catalysts very little investigation has been done into formic acid decomposition on cobalt surfaces.

Toomes and King[20] explored monolayer and multilayer potassium-promoted synthesis of surface formate and the decomposition of formic acid on Co(1010) by infrared reflective

adsorption spectroscopy (IRRAS) and temperature programmed desorption (TPD) in the temperature range 160-640 K.[20] Toomes and King[20] found the surface formate was synthesised from CO, O_2, and H_2 at 300 K. Formic acid chemisorbed onto the potassium layer forming formate and hydrogen at 160 K. The formate decomposed to CO, H_2, and atomic O above 250 K.

Inglis and Taylor[6] studied the decomposition of formic acid on 1st row transition metal thin films under 30 Torr of formic acid and temperatures between 100-300 ^{o}C. They reported a CO_2:CO ratio for Co of approximately 1 : 1. They also found that this ratio was independent of temperature for the temperature range used in their experiments and postulated that formic acid may decompose through a bimolecular pathway.

This study will explore, fundamentally, the decomposition and adsorption of formic acid on Co(0001) single crystal under ultrahigh vacuum (UHV) conditions characterized by low energy electron diffraction (LEED), using X-ray photoelectron spectroscopy (XPS) and TPD. Experimentally determined surface species are used to corroborate the proposed formic acid decomposition pathway presented herein. Surface coverage calculations based on the TPD and XPS data for the major decomposition products are also reported, as well as desorption energies.

3.3 Experimental

Experiments were carried out in a UHV chamber with a base pressure of 3 x 10^{-10} mbar. The chamber contains an XPS, LEED, STM/AFM, mass spectrometer for TPD measurements, and has been described in detail previously in the experimental chapter.

The 8 mm diameter and 0.5 mm thick cobalt (0001) single crystal sample (hcp phase) with purity of 99.999% was purchased from Princeton Scientific. The Co(0001) crystal surface was cleaned by repetitive cycles of 10 min of sputtering (3 keV, 1 x 10^{-5} mbar Ar^{+}), followed by annealing to 600 K for 5 min. The sample was confirmed clean by LEED from the hexagonal

diffraction pattern, shown in Figure 3.1. Temperatures above 630 K were avoided due to the Co phase transition from hcp to fcc at 670 K[21,22]. The sample was heated by electron bombardment and the temperature was measured by a chromel-alumel (K-type) thermocouple.

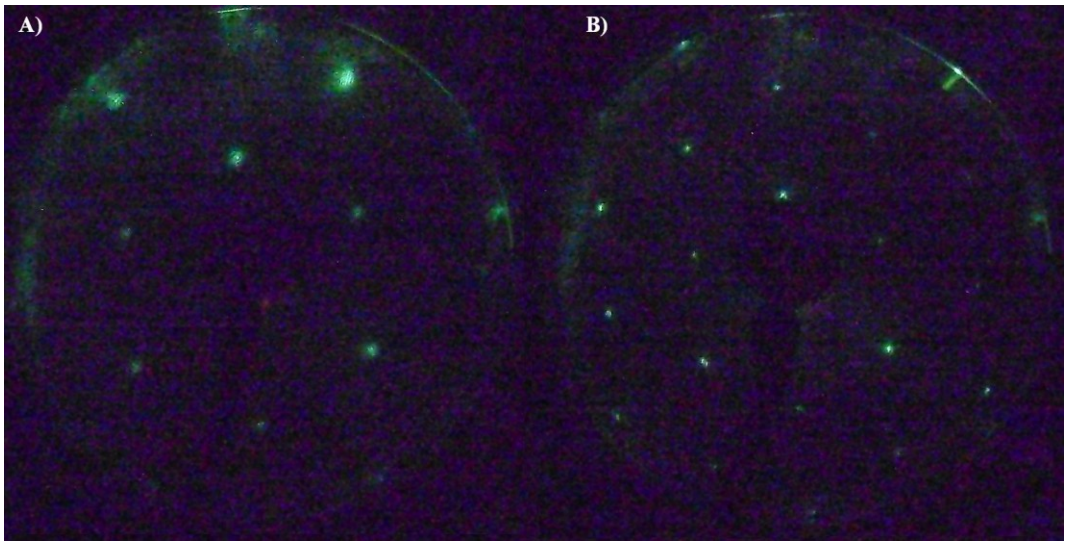

Figure 3.1: LEED patterns of clean Co(0001) obtained with A) 30 eV and B) 102 eV.

HPLC-grade formic acid (99% purity) was purchased from Sigma Aldrich. The formic acid was introduced to the UHV chamber through a leak valve that was connected to a gas manifold with a formic acid reservoir. The reservoir underwent a series of freeze-pump-thaw cycles to ensure the pressure of the gas manifold was that of the vapour pressure of formic acid. Formic acid was dosed by backfilling the chamber. All exposures are reported in Langmuir (1 L = 1.0×10^{-6} Torr s) without corrections for the gauge sensitivity.

3.3.1 XPS

XPS spectra were recorded using a standard Al Kα source (1486.7 eV) operated at 289.7 W (14.2 kV, 20.4 mA). Selected peaks were obtained in high resolution spectra using 0.1 eV step size, 1 second dwell time, and pass energy of 20 eV. When necessary, each region was scanned 3 times to increase the signal to noise ratio. The spectra were then fit using CasaXPS analysis software using a mixed Gaussian Lorentzian function and Shirley background subtractions. The

binding energy scale was calibrated using cobalt (Co 2p 3/2 = 777.8 eV).

X-ray exposure was kept to the minimum required to reduce formic acid decomposition due to the X-ray beam. The clean sample was dosed with formic acid at 130 K and then heated up to the desired temperature of observation then the spectrum was taken. Once the spectrum was finished, the sample was flashed to 630 K to clean the sample surface and verified clean by LEED. This process was repeated for each temperature of interest.

3.3.2 TPD

The sample was dosed with varying exposures of formic acid at 130 K and placed approximately 1 mm below a 1 mm diameter hole leading to the differentially pumped mass spectrometer. The temperature controlled heating ramp was programmed in LabView and designed to provide and record a linear temperature ramp using a PID controller feedback loop. All experimental ramps started at 130 K and ended at 550 K, with a ramp rate of 4.6 ± 0.15 K/s. The sample was annealed at 630 K for 5 min after each exposure to clean the sample. A total of 13 channels corresponding to m/z values of 46, 45, 44, 40, 32, 29, 28, 18, 17, 16, 14, 4, and 2, were monitored for the formic acid TPD experiments. These m/z values correspond to the expected species and their respective fragmentation patterns.

3.4 Results

The XP spectra in Figure 3.2 show that formic acid molecularly adsorbs on Co(0001) below 160 K, which corresponds to the molecular adsorption temperature on potassium doped Co(1010)[20] and is similar to other transition metals[4]. The binding energies of formic acid for the corresponding elements are carbon at 289.7 eV, and oxygen at 534.15 eV and 533 eV. At 140 K another carbon peak evolves and the oxygen envelope becomes asymmetric. This can be

attributed to formic acid going through the (3.2) dehydration pathway producing carbon monoxide and water. The binding energy of carbon monoxide in the carbon region is 286.2 eV[23–25]. The oxygen peak at 533 eV is a combination of the oxygen from carbon monoxide, 532.2 eV[23–25], water, 532.7 eV[26], and formic acid. Due to the higher binding energy formic acid oxygen and the known stoichiometry of formic acid, it becomes possible to isolate the formic acid oxygen peak at 533 eV. The binding energies of water and carbon monoxide are too similar to separate and thus are represented as a single peak.

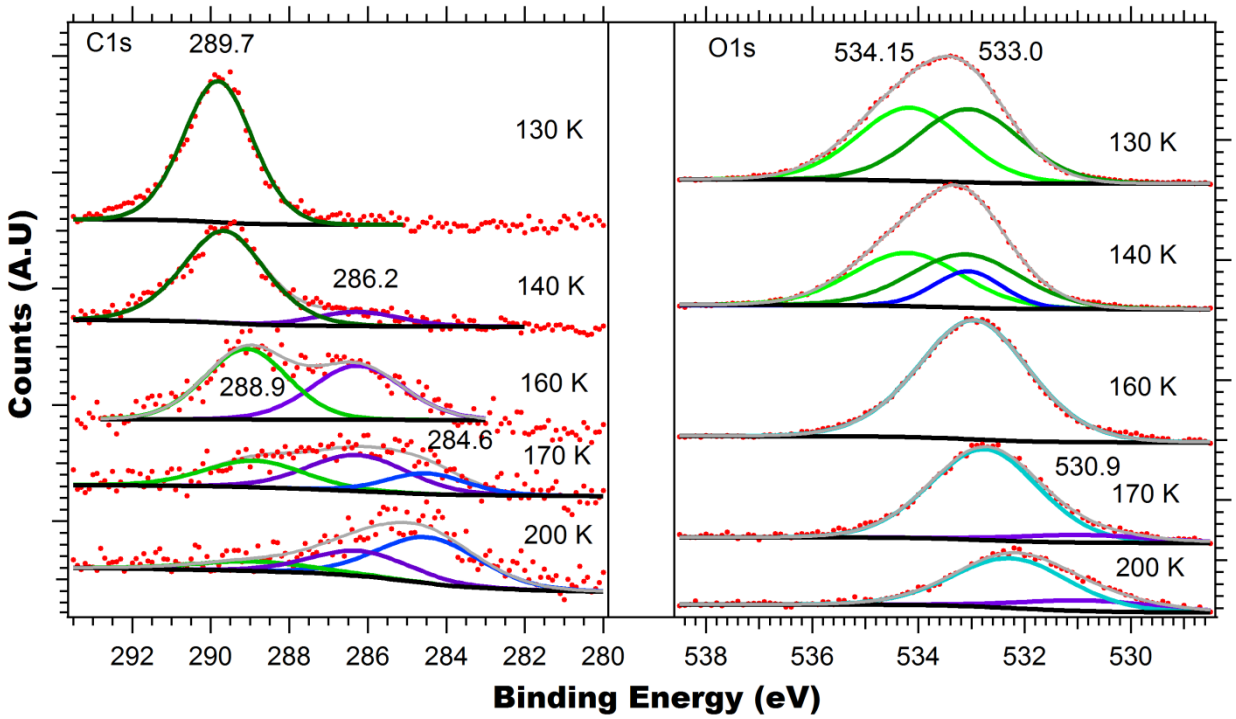

Figure 3.2: XPS of 1 L formic acid adsorption at 130 K and subsequent decomposition on Co(0001). C 1s and O 1s regions shown at varying temperatures of interest.

Upon heating to 160 K, there is a shift of 0.8 eV in the carbon peak, to 288.9 eV, and the disappearance of the higher energy, 534.15 eV oxygen peak associated with formic acid. The shift in the carbon peak is in agreement with formic acid dissociating to formate and hydrogen[27–31] and the disappearance of the higher energy oxygen peak also indicates the formation of formate binding in either the bidentate or bridged orientation. Due to the disappearance of the

higher energy formic acid oxygen peak, the deconvolution of the oxygen peak at 533 eV is no longer possible and therefore is the combined signal of formate, carbon monoxide, and water.

By 170 K, a third peak in the carbon region at 284.6 eV and a small peak in the oxygen region at 530.9 eV can be distinguished. At this temperature, carbon monoxide dissociates to carbon and oxygen on Co(0001), with binding energies reported at 284.3 eV and 531.0 eV[23–25], respectively. The error in binding energies is within the resolution of the XPS, thus it is reasonable to assume the dissociation of carbon monoxide is responsible for the additional XPS peaks. Increasing the temperature up to 200 K, there is a decrease in the formate peak and a shift in the oxygen peak to 532.5 eV. The apparent shift in the oxygen peak can be explained by the fact that the adsorbed carbon monoxide to formate ratio is increasing and thus the convoluted oxygen peak is shifting towards the carbon monoxide binding energies. Above 200 K desorption of several species becomes significant in the timeframe of XPS measurements. Thus, another technique was needed to further the investigation, here temperature programmed desorption (TPD) was used.

The TPD spectrum of m/z 46 in Figure 3.3 shows that molecular formic acid starts to desorb from the surface of Co(0001) at 160 - 220 K, with a main peak at 178 K. All peaks below 200 K are exclusively due to the fragmentation pattern of formic acid with the exception of m/z 18, which is due to water, and m/z 2 which is combination of formic acid and water. Water also desorbs from the surface of Co(0001) at 160 - 200 K which is in good agreement with Xu et al.[26] for water on Co(0001).

A peak starts to develop at 236 K in m/z 18, 2, 28, 44, and vary slightly in 46 for the 1 L and above exposures. These peaks are due in part to formic acid desorption and also carbon monoxide and water evolution from the surface. This suggests the dehydration reaction is

occurring, as all adsorbed water desorbs between 160-200 K. Knowing from the XPS data that formic acid dissociatively adsorbs on the surface above 160 K, the TPD spectrum suggests that formate and hydrogen recombine at 236 K desorbing as formic acid and the desorbing formic acid reacts through the (3.2) dehydration pathway. From 250 - 400 K, carbon monoxide desorbs from the surface[23–25]. From the XPS data, it is known that formate, carbon monoxide, carbon, oxygen, and water adsorb on the surface and with the implied dissociation of formic acid to formate and hydrogen, hydrogen is also a surface species. Hydrogen desorbs from Co(0001) at 370 K[32] in a broad second order desorption peak.

Looking at the TPD spectrum of m/z 2, with the exception of the 0 to 0.5 L exposures, which is attributed to ambient hydrogen that dissipates as the experiment progresses, hydrogen does not desorb from the surface at 370 K. Pure hydrogen desorbs at 370 K from Co(0001).[26] As hydrogen does not desorb at this temperature it must react with another surface species in order for conservation of mass to be preserved. It is unlikely that hydrogen would react with either formate or carbon, as the former should either produce formic acid or undergo the (3.1) dehydrogenation reaction. The latter would imply possible methane production; neither coincides with the observed TPD spectra. Hydrogen does not react with water on Co(0001)[26] and is unlikely to react with carbon monoxide as it would produce formyl and there is no XPS evidence of the presence formyl. This leaves only oxygen as a possible reactive species for hydrogen, which most likely produces hydroxyls. With hydroxyls on the surface this would mean that carbon, which would have normally associatively desorbed with the oxygen as carbon monoxide, must have also remained on the surface. Table 3.1 reports all relevant desorption energies calculated by Redhead analysis and the corrected pre-exponential factors used, calculated by the Charles T. Campbell et al relation.[33]

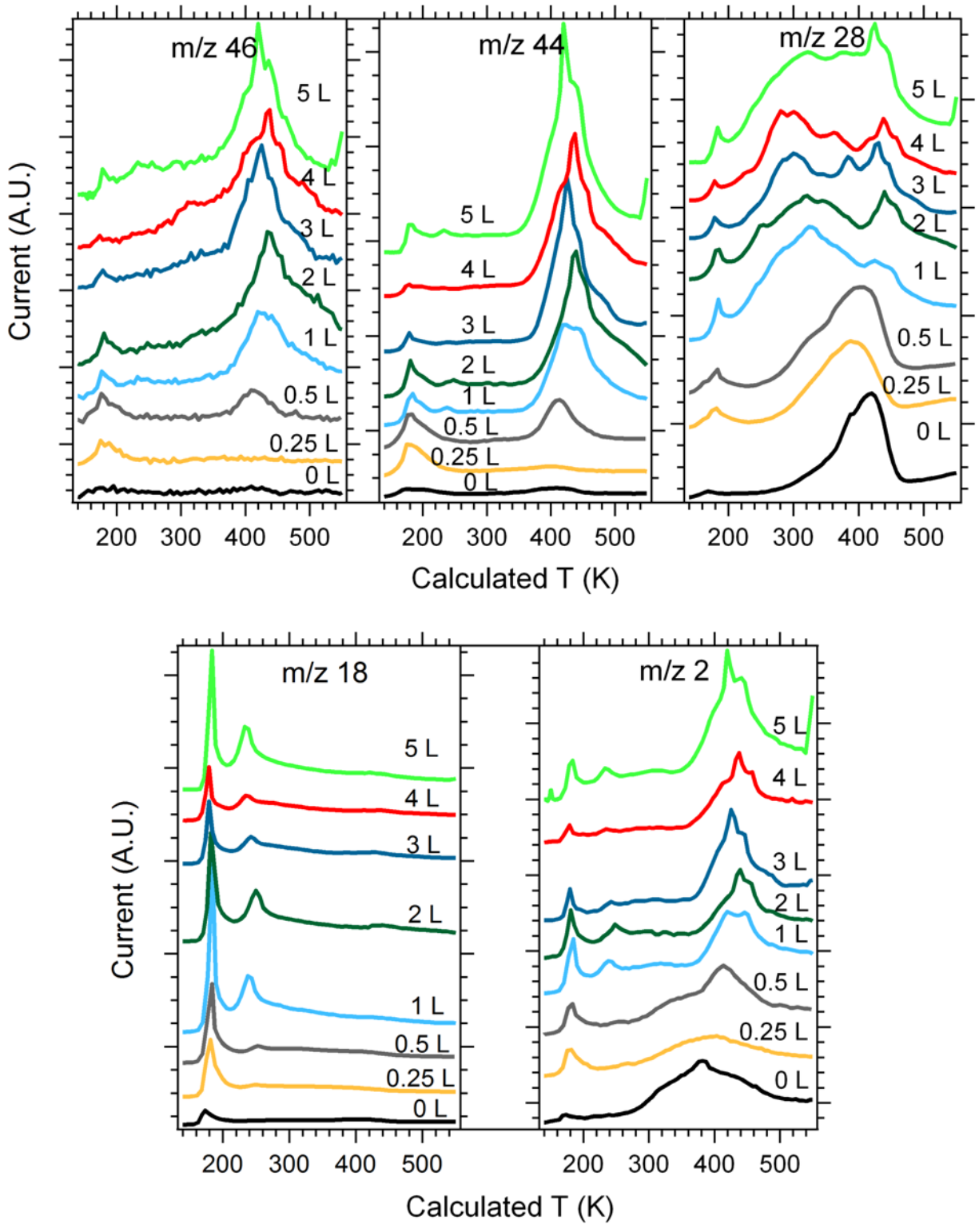

Figure 3.3: TPD spectra of mass/charge 46, 44, 28, 18, and 2 of 0 – 5 L exposures of formic acid, dosed at 130 K, on Co(0001) under a linear temperature ramp of 4.6 K up to 550 K

Table 3.1: Desorption energies of observed species, calculated by Redhead analysis.

Species	Temperature K	ν_{des} [a] mbar/s	Edes kJ/mol
Formic acid	174	1.1×10^{15}	50.2
	236[b]	1.7×10^{15}	69.5
Water	175	2.6×10^{14}	48.8
Carbon monoxide[c]	275	4.8×10^{14}	79.1
	300	5.2×10^{14}	86.7
	320	5.5×10^{14}	92.8
	380	6.5×10^{14}	111.3
	400[d]	6.9×10^{14}	117.5

[a]Preexponential factor derived by the method of Campbell et al.[33]
[b]Associative desorption.
[c]Molecular carbon monoxide desorption shows multiple peaks in this temperature range.[25,34]
[d]Reported associative desorption.[24]

Starting at 0.5 L a peak appears in m/z of 46, 44, 28, and two at 415 K. As the exposure of formic acid increases from 1 to 5 L, the peak starts to develop a triplet peak characteristic, with main peaks at 415, 438, and 455 K. After quantifying the TPD spectra explained below, it was found that these peaks were due to carbon dioxide, carbon monoxide, and hydrogen evolving from the surface in a 1:1:1 stoichiometric ratio. This implies that a reaction is occurring on the surface, as all species have desorption energies below the peak temperature. The stoichiometric ratio suggests that the observed reaction is not the dehydration (3.2) or the dehydrogenation (3.1) pathway. As previously mentioned, carbon monoxide and water both desorb at lower temperatures, thus cannot take part of this reaction, leaving formate, carbon, and hydroxyls. With known products and the likely reactants, it suggests the following pathway:

$$HCOO_{(ads)} + C_{(ads)} + OH_{(ads)} \rightarrow CO_{2(g)} + CO_{(g)} + H_{2(g)} \quad (3.3)$$

In order to quantify the TPD, the data has been separated by molecular species (i.e., water, carbon monoxide, carbon dioxide, and hydrogen) and been converted to equivalent N_2 current allowing for direct comparison and converted to pressure. Deconvolution of the currents for each species was achieved by independently measuring the fragmentation patterns of each molecule in the MS and adding the fragmentation patterns of the molecules together until the

observed currents were matched. This deconvolution is necessary because many of the m/z are shared by the molecules present such as m/z 46, 45, and 44 values being shared by both formic acid and carbon dioxide, as well as m/z 28, 29, 16, and 14 values being shared by carbon dioxide, carbon monoxide, and formic acid.[35] The conversion of the currents to equivalent N_2 was achieved by using the deconvoluted currents of each molecule, summing the relevant currents of fragmentation pattern and dividing by the relative sensitivity factor of ionization for the relevant molecule.[36] The conversion to equivalent N_2 current is required for the quantification of the TPD data because of the differing ionization cross sections of each species. The difference in ionization cross section results in differing current produced for equal amounts of molecules for each species passing through the MS. Once the current has been converted to equivalent N_2 the conversion to pressure is possible knowing the ionization energy of the MS.[36] From this data the stoichiometry of each event can be gleaned.

With the aforementioned 1:1:1 ratio of reaction (3.3), it is also important to note that the total amount of carbon monoxide produced is equivalent to the total amount of water produced. Thus the dehydration reaction (3.2) is also occurring on the surface both at 236 K and below the desorption temperature of water, 160 K.

Looking at the decomposition of formic acid on Co(0001) as a whole, the above data suggests the following reactions occur at the relevant temperatures:

$$HCOOH_{(g)} + 2S^* \overset{k_1}{\Leftrightarrow} HCOOH_{(ads)} \qquad <160\text{ K} \qquad (3.4)$$

$$HCOOH_{(ads)} + S^* \overset{k_2}{\Leftrightarrow} CO_{(ads)} + H_2O_{(ads)} \qquad 140\text{ K} \qquad (3.5)$$

$$HCOOH_{(ads)} + S^* \overset{k_3}{\Leftrightarrow} HCOO_{(ads)} + H_{(ads)} \qquad 160\text{ K} \qquad (3.6)$$

$$HCOOH_{(ads)} \overset{k_4}{\Leftrightarrow} HCOOH_{(g)} + 2S^* \qquad >160\text{ K} \qquad (3.7)$$

$$H_2O_{(ads)} \overset{k_4}{\Leftrightarrow} H_2O_{(g)} + 2S^* \quad >160\text{ K} \quad (3.8)$$

$$CO_{(ads)} + S^* \overset{k_5}{\Leftrightarrow} C_{(ads)} + O_{(ads)} \quad >170\text{ K} \quad (3.9)$$

$$HCOO_{(ads)} + H_{(ads)} \overset{k_6}{\Leftrightarrow} CO_{(g)} + H_2O_{(g)} + 3S^* \quad 236\text{ K} \quad (3.10)$$

$$CO_{(ads)} \overset{k_6}{\Leftrightarrow} CO_{(g)} + S^* \quad 300 - 400\text{ K} \quad (3.11)$$

$$O_{(ads)} + H_{(ads)} \overset{k_5}{\Leftrightarrow} OH_{(ads)} + S^* \quad <370\text{ K} \quad (3.12)$$

$$HCOO_{(ads)} + OH_{(ads)} + C_{(ads)} \overset{k_6}{\Leftrightarrow} H_{2_{(g)}} + CO_{(g)} + CO_{2_{(g)}} + 4S^* \quad 400 - 470\text{ K} \quad (3.13)$$

Where S^* is an available surface site on Co(0001).

From the above pathways two main reactions can be established; the dehydration reaction through pathways (3.4), (3.5), (3.6), and (3.10) and the reaction involving pathway (3.13). By looking at the latter as a concerted process by combining reactions (3.4), (3.5), (3.6), (3.8), (3.9), (3.12), and (3.13) the overall reaction becomes:

$$2\,HCOOH \rightarrow H_2O + CO + H_2 + CO_2 \quad (3.14)$$

Equation (3.13) is the rate determining step, as it requires the highest temperature and it has been previously predicted that the decomposition of formate would be the rate determining step[4,37]. The Langmuir-Hinshelwood type kinetic rate constants can then be derived (3.15). Due to UHV conditions the reverse reaction is negligible and thus can be simplified to (3.16).

$$rate_{tot} = k_6\theta_{HCOO}\theta_{OH}\theta_C - k_{-6}P_{H_2}P_{CO}P_{CO_2}{\theta_{S^*}}^4 \quad (3.15)$$

$$rate_{tot} = k_6\theta_{HCOO}\theta_{OH}\theta_C \quad (3.16)$$

Where θ_{S^*} is the concentration of available surface sites and is defined as the following:

$$\theta_{S^*} = 1 - \left(\theta_{HCOO} + \theta_{OH} + \theta_c + \theta_{CO} + \theta_{H_2O}\right) \quad (3.17)$$

With the quantified TPD data of the major products, leading edge analysis[38,39] was conducted, which allows for the calculation of reaction energies and pre-exponential factors. Using the integration of the major products for each exposure, assigning the appropriate pathway to the relevant peaks, and assuming the number of sites each species occupies on the surface the total number of surface sites occupied can be found. The total number of surface sites occupied became more or less constant at 3 – 5 L exposures; the average of those exposures was used as the total number of surface sites. The rates of reaction were found from the pressure of carbon dioxide evolving from the surface at a given temperature multiplied by the linear temperature ramp to report values of pressure/second. The forward rate constant was calculated for multiple coverages of formate using equation (3.16). Then using an Arrhenius plot at specific coverages, the activation energies and pre-exponential factors were found, as shown in Figure 3.4.

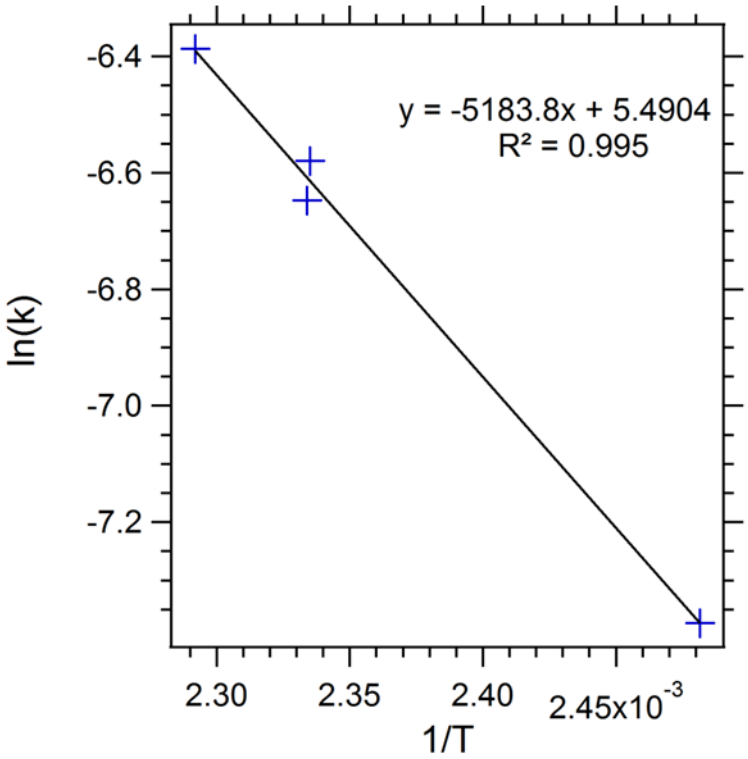

Figure 3.4: Plot of ln k vs 1/T for θ_{HCOO} = 0.9, with the equation of the fitted line and R^2.

From the analysis, an activation energy of 44.3 ± 0.6 kJ/mol and pre-exponential factor of 0.70 ± 0.05 mbar/s were obtained for the rate determining step pathway (3.13). The pre-exponential factor was found to be dependent on the inverse product of surface coverage for formate and carbon, giving an order of reaction of -1 on both C and HCOO and 0 on OH. This order of reaction is only valid for the experimental surface coverages of θ_{HCOO} = 0.06-0.15.

The absence of hydroxyls in the surface coverage dependence may be explained by the hydroxyls stabilizing adsorbed surface formates, as seen with water and formic acid in previous studies.[27,40–42] This essentially makes the likelihood of the reaction occurring (i.e., the pre-exponential factor) rely only on carbon and formate-hydroxyl complex collisions.

Bimolecular assisted formate decomposition proceeds through transition states with large negative values of standard activation entropy, which in turn leads to small pre-exponential factors.[5,43] Bimolecular interactions also lower the energy required for the formation of the activated complex.[5,43] Activation energies of 34.4 kJ/mol been reported for Mo(110) and suggested to be bimolecular decomposition.[44] NiO on Ni(111) has reported activation energies of 16-58.3 kJ/mol and an order of reaction of 0.5 [45,46], which is another surface where a bimolecular reaction has been suggested.[4] The activation energy and order of reaction calculated herein is consistent with literature values for other bimolecular formic acid decompositions. Experimentally obtained pre-exponential factors could not be found for any surface with a proposed or suspected bimolecular decomposition pathway and thus we have no reference for the one report here.

3.5 Conclusion

Formic acid adsorption and decomposition on Co(0001) was investigated in UHV by XPS and TPD. Binding energies of 289.7, 534.15, and 533 eV were found for formic acid and

288.9 and 533 eV for formate. Formic acid dissociated to formate at 160 K, molecularly desorbed from the surface above 160 K, and associatively desorbed at 236 K. Carbon monoxide desorbed from the surface at 400 K for small coverages and down to 300 K for large coverages. Water desorbed from the surface at 200 K. The dehydration reaction occurred at 140 and 236 K. A bimolecular reaction occurred on the surface at 415-450 K, with an overall reaction of:

$$2\,HCOOH \rightarrow H_2O + C + OH + HCOO \rightarrow H_2O + CO + H_2 + CO_2$$

The reaction has an activation energy of 44.3 ± 0.6 kJ/mol, pre-exponential factor of 0.7 ± 0.05 mbar/s and an order of -1 with respect to the surface coverages of formate and carbon and a 0^{th} order with respect to the hydroxyl.

3.6 References

(1) Columbia, M.; Thiel, P. The Reaction of Formic Acid with Clean and Water-Covered Pt(111). *Surf. Sci.* **1990**, *235*, 53–59.

(2) Avery, N. R. Adsorption of Formic Acid on Clean and Oxygen Covered Pt(111). *Appl. Surf. Sci.* **1982**, *11-12*, 774–783.

(3) Kizhakevariam, N. Coadsorption of Bismuth with Electrocatalytic Molecules: A Study of Formic Acid Oxidation on Pt(100). *J. Vac. Sci. Technol. A Vacuum, Surfaces, Film.* **1990**, *8*, 2557.

(4) Columbia, M. R.; Thiel, P. A. The Interaction of Formic Acid with Transition Metal Surfaces, Studied in Ultrahigh Vacuum. *J. Electroanal. Chem.* **1994**, *369*, 1–14.

(5) Iglesia, E. Unimolecular and Bimolecular Formic Acid Decomposition on Copper. *J. Phys. Chem.* **1986**, *90*, 5272–5274.

(6) Inglis, H. S.; Taylor, D. Decomposition of Formic Acid on Titanium, Vanadium, Chromium, Manganese, Iron, Cobalt, Nickel, and Copper. *J. Chem. Soc. A Inorganic, Phys. Theor.* **1969**, 2985.

(7) Haq, S.; Love, J. G.; Sanders, H. E.; King, D. A. Adsorption and Decomposition of Formic Acid on Ni{110}. *Surf. Sci.* **1995**, *325*, 230–242.

(8) Luo, Q.; Feng, G.; Beller, M.; Jiao, H. Formic Acid Dehydrogenation on Ni(111) and Comparison with Pd(111) and Pt(111). *J. Phys. Chem. C* **2012**, *116*, 4149–4156.

(9) Smith R J, B.; Loganathan, M.; Shantha, M. S. A Review of the Water Gas Shift Reaction Kinetics. *Int. J. Chem. React. Eng.* **2010**, *8*.

(10) Zafeiratos, S.; Dintzer, T.; Teschner, D.; Blume, R.; Hävecker, M.; Knop-Gericke, A.; Schlögl, R. Methanol Oxidation over Model Cobalt Catalysts: Influence of the Cobalt Oxidation State on the Reactivity. *J. Catal.* **2010**, *269*, 309–317.

(11) Mohanty, P.; Pant, K. K.; Naik, S. N.; Parikh, J.; Hornung, A.; Sahu, J. N. Synthesis of Green Fuels from Biogenic Waste through Thermochemical Route – The Role of Heterogeneous Catalyst: A Review. *Renew. Sustain. Energy Rev.* **2014**, *38*, 131–153.

(12) Hosseini, H.; Mahyari, M.; Bagheri, A.; Shaabani, A. Pd and PdCo Alloy Nanoparticles Supported on Polypropylenimine Dendrimer-Grafted Graphene: A Highly Efficient Anodic Catalyst for Direct Formic Acid Fuel Cells. *J. Power Sources* **2014**, *247*, 70–77.

(13) Yin, M.; Li, Q.; Jensen, J. O.; Huang, Y.; Cleemann, L. N.; Bjerrum, N. J.; Xing, W. Tungsten Carbide Promoted Pd and Pd–Co Electrocatalysts for Formic Acid

Electrooxidation. *J. Power Sources* **2012**, *219*, 106–111.

(14) Stevanović, S.; Babić-Samardžija, K.; Sovilj, S. P.; Tripković, A.; Jovanović, V. M. Oxidation of Formic Acid on Platinum Surfaces Decorated with cobalt(III) Macrocyclic Complexes. *Russ. J. Phys. Chem. A* **2009**, *83*, 1442–1446.

(15) Olson, T. S.; Pylypenko, S.; Kattel, S.; Atanassov, P.; Kiefer, B. Selectivity of Cobalt-Based Non-Platinum Oxygen Reduction Catalysts in the Presence of Methanol and Formic Acid. *J. Phys. Chem. C* **2010**, *114*, 15190–15195.

(16) Zhang, L.; Wan, L.; Ma, Y.; Chen, Y.; Zhou, Y.; Tang, Y.; Lu, T. Crystalline Palladium–cobalt Alloy Nanoassemblies with Enhanced Activity and Stability for the Formic Acid Oxidation Reaction. *Appl. Catal. B Environ.* **2013**, *138-139*, 229–235.

(17) Stathi, P.; Deligiannakis, Y.; Louloudi, M. Co-Catalytic Enhancement of H2 Production by SiO2 Nanoparticles. *Catal. Today* **2015**, *242*, 146–152.

(18) Rice, C. Catalysts for Direct Formic Acid Fuel Cells. *J. Power Sources* **2003**, *115*, 229–235.

(19) Zhou, X.; Liu, C.; Liao, J.; Lu, T.; Xing, W. Platinum-Macrocycle Co-Catalysts for Electro-Oxidation of Formic Acid. *J. Power Sources* **2008**, *179*, 481–488.

(20) Toomes, R.; King, D. Potassium-Promoted Synthesis of Surface Formate and Reactions of Formic Acid on Co {1010}. *Surf. Sci.* **1996**, 43–64.

(21) Lewis, W. F. Magnetic Domain Behavior during the Hcp-to-Fcc Phase Transition in Cobalt Using Lorentz Electron Microscopy. *J. Appl. Phys.* **1977**, *48*, 2980.

(22) Bidaux, J. E. Study of the H.c.p.-F.c.c. Phase Transition in Cobalt by Acoustic Measurements. *Acta Metall. 37*, 803–811.

(23) Habermehl-Cwirzen, K. Sulfur Poisoning of the CO Adsorption on Co(0001). *Surf. Sci. 573*, 183–190.

(24) Cabeza, G. . Adsorption of CO on Co(0001) and Pt–Co(0001) Surfaces: An Experimental and Theoretical Study. *Surf. Sci.* **2000**, *465*, 286–300.

(25) Lahtinen, J.; Vaari, J.; Kauraala, K. Adsorption and Structure Dependent Desorption of CO on Co(0001). *Surf. Sci.* **1998**, *418*, 502–510.

(26) Xu, L.; Ma, Y.; Zhang, Y.; Chen, B.; Wu, Z.; Jiang, Z.; Huang, W. Water Adsorption on a Co(0001) Surface †. *J. Phys. Chem. C* **2010**, *114*, 17023–17029.

(27) Search, H.; Journals, C.; Contact, A.; Iopscience, M.; Address, I. P. The Reactive Chemisorption of Formic Acid at Al (111) Surfaces and the Influence of Surface

Oxidation and Coadsorption with Water□: A Combined XPS and HREELS Investigation. **1991**, *237*.

(28) Mazurkiewicz, M.; Malolepszy, A.; Mikolajczuk, A.; Stobinski, L.; Borodzinski, A.; Lesiak, B.; Zemek, J.; Jiricek, P. Pd/MWCNTs Catalytic Activity in the Formic Acid Electrooxidation Dependent on Catalyst Surface Treatment. *Phys. Status Solidi* **2011**, *248*, 2516–2519.

(29) Cano, E.; Torres, C.; Bastidas, J. An XPS Study of Copper Corrosion Originated by Formic Acid Vapour at 40% and 80% Relative Humidity. *Mater. Corros. UND KORROSION* **2001**, *52*, 667–676.

(30) Ayyoob, M.; Hegde, M. S. Electron Spectroscopic Studies of Formic Acid Adsorption and Oxidation on Cu and Ag Dosed with Barium. *J. Chem. Soc. Faraday Trans. 1 Phys. Chem. Condens. Phases* **1986**, *82*, 1651.

(31) Au, C. T. Adsorption and Interaction of Carbon Dioxide, Formic Acid and Hydrogen/carbon Dioxide Mixtures on (100) Zinc Oxide Surfaces Studied by Photoelectron Spectroscopy (XPS and UPS). *Surf. Sci. 199*, 507–517.

(32) Van Helden, P.; van den Berg, J.-A.; Weststrate, C. J. Hydrogen Adsorption on Co Surfaces: A Density Functional Theory and Temperature Programmed Desorption Study. *ACS Catal.* **2012**, *2*, 1097–1107.

(33) Campbell, C. T.; Árnadóttir, L.; Sellers, J. R. V. Kinetic Prefactors of Reactions on Solid Surfaces. *Zeitschrift für Phys. Chemie* **2013**, *227*, 1435–1454.

(34) Wesner, D. A.; Linden, G.; Bonzel, H. P. Alkali Promotion on Cobalt: Surface Analysis of the Effects of Potassium on Carbon Monoxide Adsorption and Fischer-Tropsch Reaction. *Appl. Surf. Sci.* **1986**, *26*, 335–356.

(35) US Department of Commerce, N. NIST Standard Reference Database 1A v14.

(36) Nakao, F. Determination of the Ionization Gauge Sensitivity Using the Relative Ionization Cross-Section. *Vacuum* **1975**, *25*, 431–435.

(37) Xu, J.; Yuan, D.; Yang, F.; Mei, D.; Zhang, Z.; Chen, Y.-X. On the Mechanism of the Direct Pathway for Formic Acid Oxidation at a Pt(111) Electrode. *Phys. Chem. Chem. Phys.* **2013**, *15*, 4367–4376.

(38) Málek, J.; Criado, J. M. Temperature Programmed Desorption (TPD) from Catalyst Surfaces: The Symmetry of the TPD Curve as a Function of the Kinetic Model. *Thermochim. Acta* **1992**, *208*, 275–281.

(39) Kolasinski, K. K.; Kolasinski, K. W. *Surface Science: Foundations of Catalysis and Nanoscience*; John Wiley & Sons, 2012.

(40) Qi, Y.; Zhu, R.; Zhang, D. Adsorption Behaviors of Monomer and Dimer of Formic Acid on Pt (111) in the Absence and Presence of Water. *J. Mol. Model.* **2014**, *20*, 2264.

(41) Silbaugh, T. L.; Karp, E. M.; Campbell, C. T. Energetics of Formic Acid Conversion to Adsorbed Formates on Pt(111) by Transient Calorimetry. *J. Am. Chem. Soc.* **2014**, *136*, 3964–3971.

(42) Akiya, N.; Savage, P. E. Role of Water in Formic Acid Decomposition. *AIChE J.* **1998**, *44*, 405–415.

(43) Ting, S.-W.; Cheng, S.; Tsang, K.-Y.; van der Laak, N.; Chan, K.-Y. Low Activation Energy Dehydrogenation of Aqueous Formic Acid on Platinum-Ruthenium-Bismuth Oxide at near Ambient Temperature and Pressure. *Chem. Commun. (Camb).* **2009**, 7333–7335.

(44) Flaherty, D. W.; Berglund, S. P.; Mullins, C. B. Selective Decomposition of Formic Acid on Molybdenum Carbide: A New Reaction Pathway. *J. Catal.* **2010**, *269*, 33–43.

(45) Bandara, A.; Kubota, J.; Wada, A.; Domen, K.; Hirose, C. Adsorption and Reactions of Formic Acid on (2×2)-NiO(111)/Ni(111) Surface. 2. IRAS Study under Catalytic Steady-State Conditions. *J. Phys. Chem. B* **1997**, *101*, 361–368.

(46) Bandara, A.; Kubota, J.; Wada, A.; Domen, K.; Hirose, C. Adsorption and Decomposition of Formic Acid on the NiO(111)-p(2 × 2) Surface: TPD and Steady State Kinetics Studies. *Surf. Sci.* **1996**, *364*, L580–L586.

Chapter 4:

Adsorption and Decomposition of Formic Acid on Cobalt

4.0 Adsorption and Decomposition of Formic Acid on Highly Stepped Cobalt

Jeffrey J. Sims[a,b], David J. Mandia[d], Javier B. Giorgi[a,c]

[a]*Centre for Catalysis Research and Innovation,* [b]*Department of Chemical and Biological Engineering,* [c]*Department of Chemistry,*

University of Ottawa, 10 Marie Curie Pvt., Ottawa, Ontario, Canada. K1N 6N5.

[d]*Department of Chemistry. Carleton University, 1125 Colonel By Drive, Ottawa, Ontario, Canada, K1S 5B6*

4.1 Abstract

Formic acid decomposes through dehydrogenation and dehydration. Mechanisms and reaction ratios depend on the nature of the catalysts used. This work provides mechanistic insight into the decomposition of formic acid on cobalt. The adsorption and decomposition of formic acid on a highly stepped crystal of cobalt was studied in ultra-high vacuum by XPS and temperature programmed desorption. Formic acid adsorbs molecularly on the surface below 160 although partial decomposition to carbonyl and formyl intermediates takes place even below that temperature. At 160 K decomposition of formic acid into formate is dominant. Water is formed at low temperature (below 200K) and the remaining intermediates produce H_2, CO and CO_2 in equal quantities at ~470 K. A full mechanism is proposed for which the measured parameters are: activation energy = 147.2 ± 2.0 kJ/mol and pre-exponential factor = $10^{11.3 \pm 0.2}$ mbar/s

4.2 Introduction

Formic acid decomposition is an important model reaction in catalysis. Formic acid provides an ideal framework for understanding decomposition of small organic molecules, as it is known that formic acid can decompose through (4.1) dehydrogenation and (4.2) dehydration pathways producing CO_2 and H_2 or CO and H_2O.

$$HCOOH \rightarrow CO_2 + H_2 \quad (4.1)$$

$$HCOOH \rightarrow CO + H_2O \quad (4.2)$$

These reactions have been studied both theoretically and experimentally on a number of different catalyst surfaces mainly focusing on platinum[1–7], palladium[7–12], ruthenium[6,13–22], rhodium[20,23–30], and nickel[31–39]. From these, the mechanism of decomposition is usually described as proceeding through two very general steps:[6,17,40,41] First, HCOOH reacts on the surface to form an intermediate; and then the intermediate decomposes to form CO, CO_2, H_2O, H_2, O, or C. The last two products could remain on the surface as residues and are due to more extensive decomposition. A number of intermediates have been proposed, namely carboxylate (COOH), formyl (HCO), formate (HCOO), and anhydride ($(HCO)_2O$). [40,41]

Cobalt has been used for alloying or doping of other metals to help improve the catalysts sensitivity to CO and other poisons.[12,42–44] This suggests that Co itself should be an interesting catalyst for formic acid decomposition, but there has been very little investigation into the mechanism on cobalt surfaces. Inglis and Taylor[45] studied the decomposition of formic acid on cobalt thin films under 30 Torr of formic acid and temperatures between 100-300 ^oC They report a CO_2:CO ratio of approximately 1 : 1. Inglis and Taylor also found that this ratio was independent of temperature for the temperature range used in their experiments, which led them to propose a bimolecular decomposition reaction pathway.

Multilayer and monolayer potassium-promoted formic acid adsorption on Co(1010) was investigated by RAIRS and TPD in the temperature range of 160-640 K.[46] It was shown that the formate forms at 160 K, binding to the potassium and adsorbs in a bridging formation. On monolayer potassium, Upon heating the adsorbed formate decomposes to carbon monoxide, dihydrogen and adsorbed oxygen on a Co(1010)-supported potassium monolayer. On multilayered potassium, tetradentate oxalate and carbonate is formed in addition to the previously mentioned products due to the interaction with bulk potassium. The oxalate and carbonate decompose to carbon monoxide and oxygen at 660 K.

The alloying of cobalt and palladium nanoparticles has proven to increase the current densities for direct formic acid electro-oxidation in H_2SO_4 aqueous solution, relative to homogeneous palladium at room temperature[11]. The oxidation current density of homogeneous palladium nanoparticles degrades over time due to the accumulation of carbon monoxide-like species. The cobalt-doped palladium nanoparticles stabilized the current attributed to the removal of the carbon monoxide-like surface poison. The products observed by gas chromatography were only dihydrogen and carbon dioxide suggesting only the dehydrogenation reaction occurs.

This paper will fundamentally explore the decomposition and adsorption of formic acid on a cobalt single crystal under ultrahigh vacuum (UHV) conditions using X-ray photoelectron spectroscopy (XPS) and temperature-programmed desorption (TPD). Experimentally determined surface species are used to corroborate the proposed formic acid decomposition pathway presented herein. Surface coverage calculations based on the TPD and XPS data for the major decomposition products are also reported, as well as desorption energies.

4.3 Experimental

All experiments were conducted in a custom-built multi-technique UHV setup

constructed by Specs GmbH. The instrument is divided into two chambers connected by a transfer arm with allows sample heating and cooling in the range of 110 to 1300 K. The analytical chamber has a base pressure of 3 x 10^{-10} mbar and is used for sample cleaning, basic sample characterization and temperature programmed desorption experiments. The Chamber contains a Specs XPS/UPS setup, LEED, a Pfeiffer differentially pumped multichannel mass spectrometer (MS), and ion sputter gun as the basic components. The STM chamber, with a base pressure of 5 x 10^{-11} mbar, has a variable temperature RHK scanning probe microscope with both scanning tunneling microscopy (STM) and atomic force microscopy (AFM) capabilities. For all experiments reported in this study, it is important to note that the sample is cleaned before measurement with any of the techniques and the sample was always in the same chamber location when gases were dosed.

The 8 mm diameter and 0.5 mm thick cobalt (0001) single crystal sample (hcp phase) with purity of 99.999% was purchased from Princeton Scientific. The (0001) crystal surface was roughened mechanically by polishing with a series of diamond suspensions from 30 to 0.1 micron and chemically etched with a silica colloid at the University of Ottawa, to obtain the highly stepped surface. The cleaning procedure following roughening consisted of repetitive cycles of 10 min of sputtering (3 keV, 1 x 10^{-5} mbar Ar^{+}) and followed by annealing to 600 K for 5 min. The sample was confirmed clean by XPS. Temperatures above 630 K were avoided due to the Co phase transition from hcp to fcc at 670 K[47,48]. The sample was heated by electron bombardment by a tungsten filament directly below the sample that is attached to the main manipulator arm of the UHV chamber. The temperature was measured by a chromel-alumel (K-type) thermocouple. Figure 4.1 shows an STM image of the clean cobalt surface before the experiments. STM images were taken periodically to ensure the surface morphology did not

change.

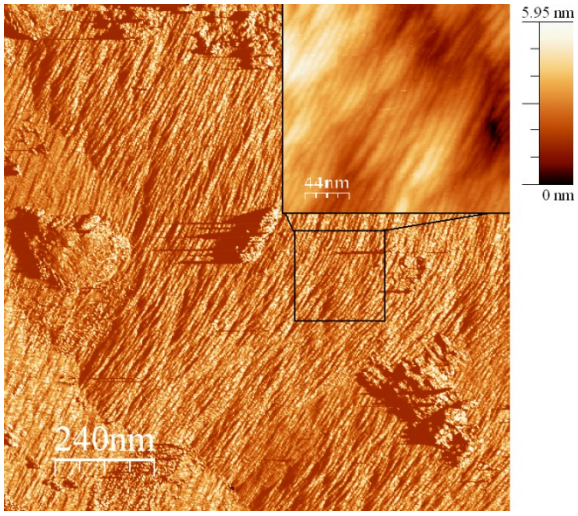

Figure 4.1: 1.2 x 1.2 µm STM topographic image of clean highly stepped cobalt surface flattened and derived. Inset shown is the 220 x 220 nm STM topograph of the enclosed region flattened. Image post-processing done using WSxM.

HPLC-grade formic acid (99% purity) was purchased from Sigma Aldrich. The formic acid was introduced through a leak valve to the UHV chamber by a gas manifold. Before dosing, the formic acid reservoir underwent a series of freeze-pump-thaw cycles. Formic acid was dosed by backfilling the chamber. All exposures are reported in Langmuir (1 L = 1.0×10^{-6} Torr s) without corrections for the gauge sensitivity.

4.3.1 XPS

XPS spectra were recorded using a standard Al Kα source (1486.7 eV) operated at 380 W (14.6 kV 26 mA). Selected peaks were obtained in high resolution spectrums using 0.05 eV step size, 1 second dwell time, and a pass energy of 20 eV. When necessary, each region was scanned 3 times to increase the signal to noise ratio. The spectra were then fit using CasaXPS analysis

software using a mixed Gaussian Lorentzian function and Shirley background subtractions. The binding energy scale was calibrated using cobalt (Co 2p 3/2 = 777.8 eV).

X-ray exposure was kept to the minimum required to reduce formic acid decomposition due to the X-ray beam. The clean sample was dosed with formic acid at 110 K and then heated up to the desired temperature of observation then the spectrum was taken. Once the spectrum was finished, the sample was flashed to 630 K to clean the sample surface and verified clean by XPS. This process was repeated for each temperature of interest.

4.3.2 TPD

The sample was dosed with varying exposures of formic acid at 130 K and placed approximately 1 mm below a 1 mm diameter hole leading to the differentially pumped mass spectrometer. The temperature controlled heating ramp was programmed in LabView and designed to provide and record a linear temperature ramp using a PID controller feedback loop. All experimental ramps started at 130 K and ended at 600 K, with a ramp rate of 3.5 ± 0.2 K/s. The sample was annealed at 630 K for 5 min after each exposure to clean the sample. Multiple m/z channels were monitored, corresponding to the expected species and their respective fragmentation patterns.

4.4 Results

Formic acid adsorbs molecularly on cobalt below 160 K, consistent with observations on other transition metal surfaces[40]. As shown in Figure 4.2, the XPS of adsorbed formic acid shows characteristic spectra for each element, with associated binding energies of 289.7 eV for C1s; and 534.5 eV and 533.2 eV for O1s (110 K). The carbon peak at 292.3 eV is assigned to anhydride (OCHOCHO) based on the range of chemical shift reported between formic acid and

methyl formate[49,50]. The 287.4 eV peak has a chemical shift which is in good agreement with the shift between formic acid and formaldehyde, which would present a similar shift as formyl (HCO)[51–58] and thus there is precedent to assign the peak to formyl. These two intermediates can be produced by formic acid dimer dissociating through pathway (4.3) and (4.4). These two assignments are correlated to oxygen peaks at 536.9 eV for anhydride and 531.7 eV for the formyl group. The second oxygen peak associated with anhydride overlaps in binding energy with the lower binding energy of formic acid and formate and therefore cannot be resolved by XPS in this case. The presence of the 284.7 eV peak is associated C formed via CO dissociative adsorption[59] indicating that the dehydration reaction (4.2) has occurred.

$$2\,HCOOH_{ads} \rightarrow HCOOOCH_{ads} + H_2O_{ads} \qquad (4.3)$$

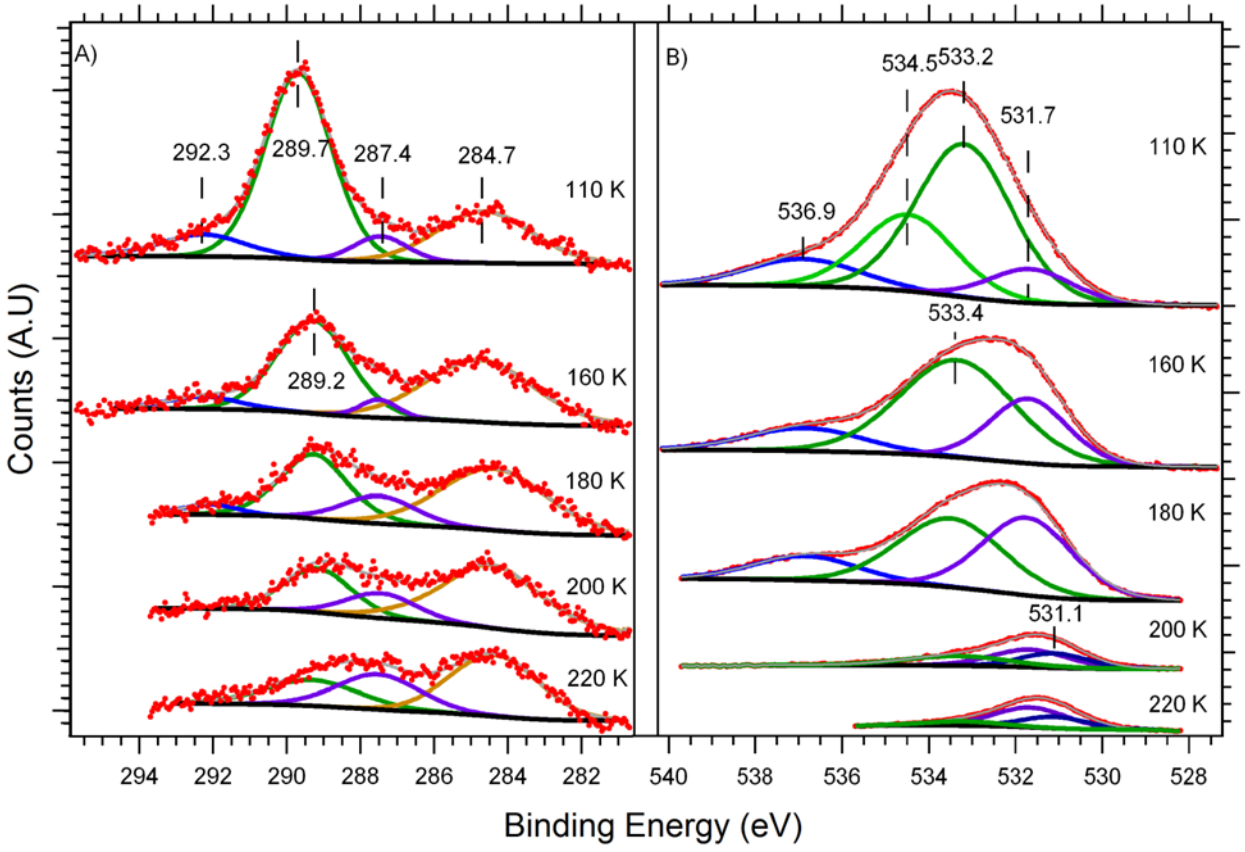

Figure 4.2:XPS of cobalt exposed to 1 L of formic acid at varying temperatures. A) C 1s region and B) O 1s region with the relevant peak positions labelled.

$$HCOOH_{ads} \rightarrow HCO_{ads} + OH_{ads} \quad (4.4)$$

$$HCOOH_{ads} \rightarrow HCOO_{ads} + H_{ads} \quad (4.5)$$

Above 160 K the adsorbed formic acid dissociates to HCOO through pathway (4.5), which results in a 0.5 eV shift[11,40,51,60–63] to 289.2 eV for the formic acid carbon peak and the concurrent disappearance of the higher binding energy oxygen peak at 534.5 eV, resulting in a shift of 0.1 eV to the corresponding to the major oxygen peak (533.4 eV) in the peak envelope. The disappearance of the higher binding energy oxygen peak suggests that the formate binds in the bidentate or bridging formation, which coincides with predicted binding orientations[7,22,38,46,64,65].

Below 200 K, anhydride decomposes to form water and CO, part of which combines with free adsorbed hydrogen to form formyl, following reactions (4.6) and (4.7). This is shown by the disappearance of the carbon peak associated with the anhydride, the increase of the 284.7 eV carbon peak and the 531.7 eV oxygen peak, which are directly associated with CO dissociative adsorption[59] on cobalt and the increase in peak 287.4 eV associated with HCO.

$$HCOOOCH_{ads} \rightarrow H_2O_{ads} + 2CO_{ads} \quad (4.6)$$

$$CO_{ads} + H_{ads} \rightarrow HCO_{ads} \quad (4.7)$$

Above 250 K, the desorption rate is sufficiently high to prevent accurate XPS spectra, however the decomposition can be monitored by TPD. The TPD spectrum of m/z 46 in Figure 4.3 shows that molecular formic acid desorbs from the surface starting at 240 K for low exposures and down to 160 K for higher exposures, with multilayer peaks occurring at 195 K and 175 K

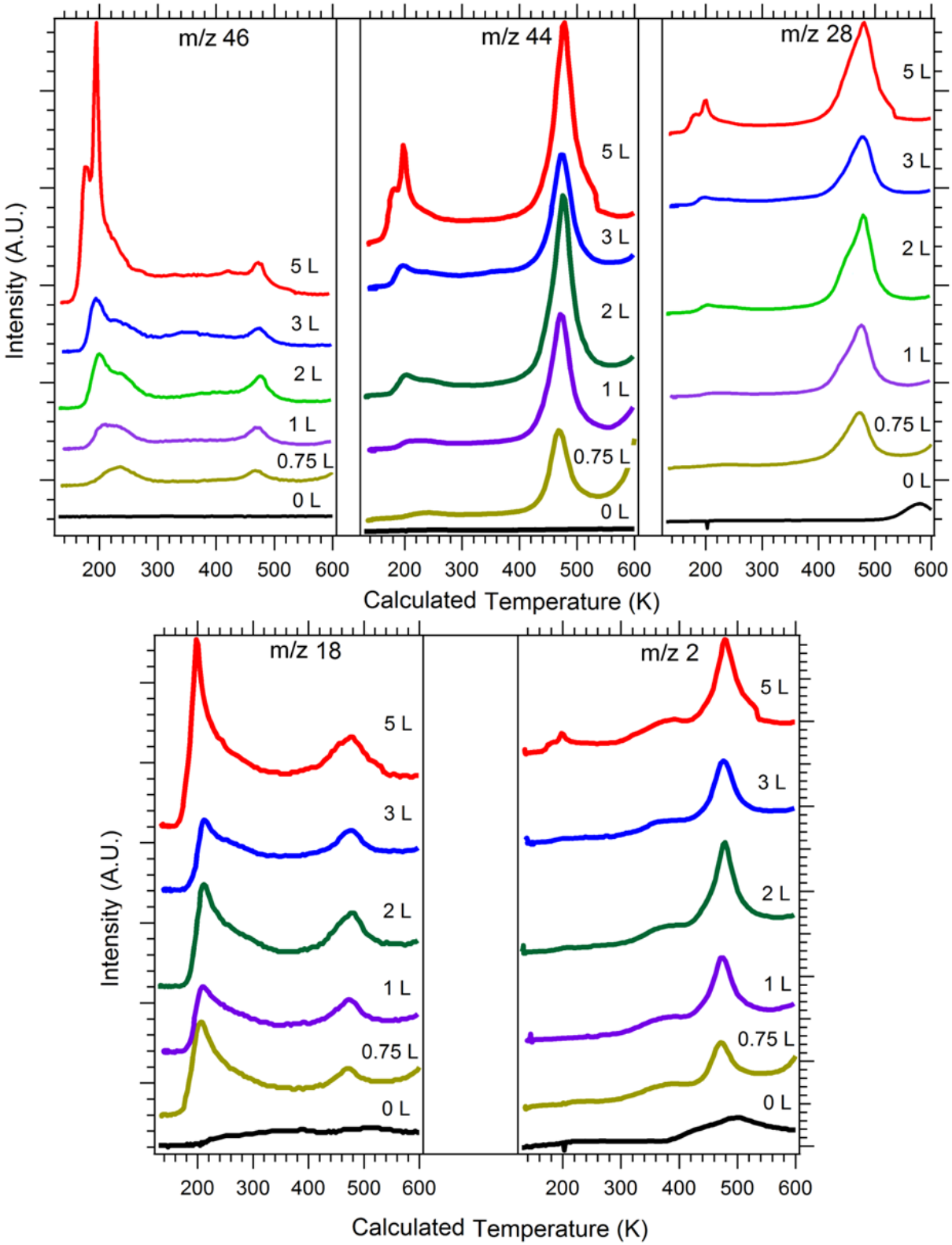

Figure 4.3: TPD spectrum of m/z of 46,44,28,18, and 2 of 0.75 - 5 L exposures of formic acid on cobalt dosed at 130 K with a temperature ramp of 3.5 K/s.

This suggests that part of the adsorbed transient species recombine with hydrogen and desorbs as molecular formic acid. Except for water, no other species desorbs from the surface below 300 K. Peaks seen for other m/z components correspond to the fragmentation of formic acid in the MS.

Independent measurements of TPD for the H_2O/Co and CO/Co systems confirm the desorption temperatures of each species, as shown in Figure 4.4. Water, m/z 18, has monolayer desorption at 200 K and a multilayer peak developing at 195 K. CO, m/z 28, has associative desorption peak at 430-450 K depending on coverage and develops multilayer desorption peaks to 300 K.

Comparison of the independently run CO and water TPDs, shown in Figure 4.4, with the data obtained with formic acid allows the identification of the peaks at 200 K for m/z 18, in Figure 4.3, as molecular water desorption and the ~430 K shoulder of the 475 K peak in m/z 28, in Figure 4.3, as the associative desorption of CO. The 475 K peak is analysed in more detail below as arising from subsequent reaction products on the surface.

The desorption of water at it normal desorption temperature after dosing formic acid and the presence of the carbon monoxide associative desorption suggests that the dehydration reaction (2) takes place at low temperature, in agreement with the assignment of carbon in the XPS at low temperatures. After quantifying the TPD data, explained below, the ratio of the associative desorption CO peak to the 475 K CO peak is 1: 2 and the ratio of water to CO is 1:1. These ratios suggest that a 1/3 of the CO was produced by the dehydration reaction, the remaining 2/3 were produced by the pathway including the 475 peak, and for all pathways water is formed below 200 K. The broad desorption peak of m/z 2 at 370 K is due to the molecular desorption of hydrogen[66] which can be attributed to background hydrogen.

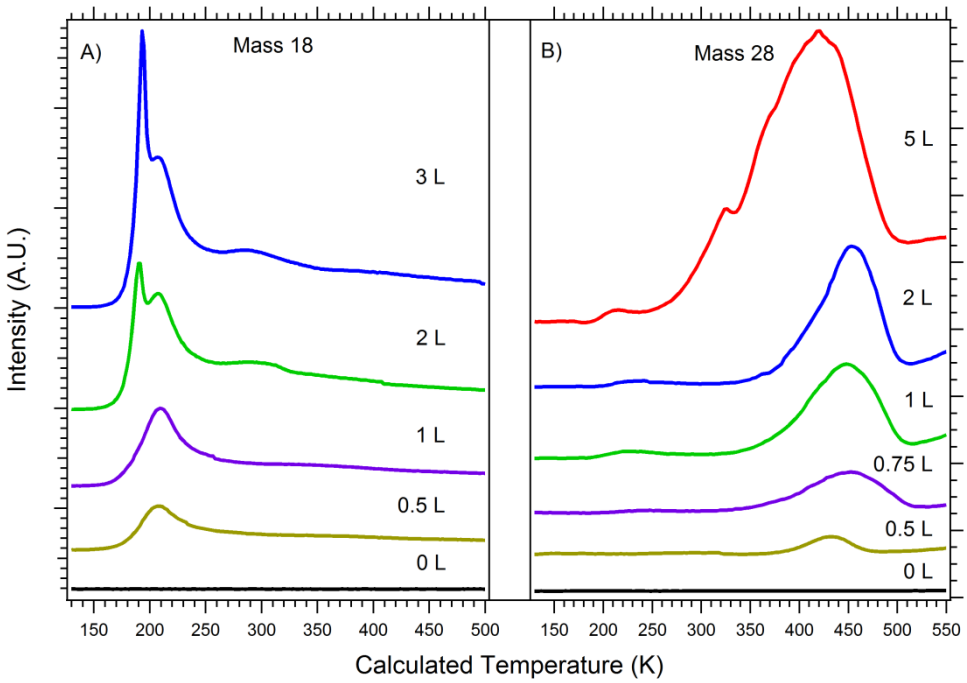

Figure 4.4:A) TPD spectrum of 0.5 - 3 L exposures of water on cobalt dosed at 130 K with a temperature ramp of 3.5 K/s. B) TPD spectrum of 0.5 - 5 L exposures of CO on cobalt dosed at 130 K with a temperature ramp of 3.5 K/s.

For the subsequent CO, CO_2, and H_2 peaks at 470 - 480 K, in Figure 4.3, it is postulated that only the HCOO and HCO species will be on the surface, as all other species have known desorption temperatures below this temperature range, as previously mentioned. After quantifying the TPD data, it was found that H_2, CO, and CO_2 were produced in a 1 H_2: 1.1 CO: 1 CO_2 ratio, with a small amount of water being produced. This suggests that HCO and HCOO react through pathway (4.8) in this temperature range.

$$HCOO_{ads} + HCO_{ads} \rightarrow H_2 + CO + CO_2 \quad (4.8)$$

$$H_2 + CO_2 \rightarrow H_2O + CO \quad (4.9)$$

The presence of water in the 470-480 K temperature range is difficult to explain. Although there is precedence for an Eley-Rideal mechanism for the reverse water-gas shift reaction (4.9)[67–70] between the products of reaction (4.8), it seems unlikely that such a process could occur to such an extent under UHV conditions. The reaction temperatures increase with

increasing exposure of formic acid. No significant amount of formate or formic acid was observed desorbing in this temperature range (all m/z 45 and 46 could be attributed as the standard peaks produced in the MS due to CO_2). Desorption energies were calculated by Redhead analysis using corrected vibrational frequency factors, based on the Campbell et al. model.[71] Desorption energies of each of the observed species are reported in Table 4.1.

To obtain mechanistic info we needed to quantify the TPD components and separate fragmentation signal originating from different molecules. For that purpose, the TPD data has been separated by molecule (i.e., water, CO, CO_2, H_2, and formic acid) and been converted to equivalent N_2 current allowing for direct comparison, not shown. Deconvolution of the currents for each molecule was achieved by using fragmentation patterns of each molecule measured independently in the MS and then adding the patterns of the molecules together until the observed currents were matched. This deconvolution is necessary because many of the m/z are shared by the molecules present such as m/z 46, 45, and 44 values being shared by both formic acid and CO_2, as well as m/z 28, 29, 16, and 14 values being shared by CO_2, CO, and formic acid.[66] The conversion of the currents to equivalent N_2 was achieved by using the deconvoluted currents of each molecule, summing the relevant currents of the fragmentation pattern and dividing by the relative sensitivity factor of ionization for the relevant molecule.[72]

Consider formic acid decomposition as the following concerted process corresponding to the 470 K reaction peak observed in the TPD:

$$2\,HCOOH \rightarrow CO + H_2 + H_2O + CO_2 \qquad (4.10)$$

From the deconvoluted N_2 equivalent current and knowing the ionization current the products can be expressed in units pressure.[72] With the major products expressed in pressure, surface coverage calculations of these products and a rate constant for formic acid decomposition

can be computed.

The mechanism for pathway (4.10), shown in Figure 4.5, can be explained by the following reactions:

$$HCOOH + 3S^* \underset{\leftrightarrows}{^{k_1}} HCOO_{(ads)} + H_{(ads)} \quad (4.11)$$

$$HCOOH + 3S^* \underset{\leftrightarrows}{^{k_{2a}}} CO_{(ads)} + H_2O_{(ads)} \quad (4.12a) \qquad HCOOH + 3S^* \underset{\leftrightarrows}{^{k_{2b}}} HCO_{(ads)} + OH_{(ads)} \quad (4.12b)$$

$$CO_{(ads)} + H_{(ads)} \underset{\leftrightarrows}{^{k_{3a}}} HCO_{(ads)} \quad (4.13a) \qquad OH_{(ads)} + H_{(ads)} \underset{\leftrightarrows}{^{k_{3b}}} H_2O_{(ads)} \quad (4.13b)$$

$$H_2O_{(ads)} \underset{\leftrightarrows}{^{k_4}} H_2O + 2S^* \quad (4.14)$$

$$HCOO_{(ads)} + HCO_{(ads)} \underset{rds}{\overset{k_5}{\leftrightarrows}} H_2 + CO + CO_2 + 4S^* \quad (4.15)$$

Where S^* is an available surface site on cobalt. Pathway a and b (for reaction 4.12 and 4.13) represent possible reactions that could occur to give the intermediates and products observed. Combining (4.11)-(4.15) with (4.15) as the rate determining step, as it requires the highest activation energy and has been previously predicted[40,41], the Langmuir-Hinshelwood type kinetic rate constant can be derived (4.16) and simplified to (4.17). Note that reactions (4.11) to (4.14) take place below 200 K, as water is seen to desorb at that temperature. The reverse reaction can be assumed negligible as it would require CO_2 to interact with the surface and under UHV conditions it is unlikely for the reaction to occur.

$$rate_{tot} = k_5\theta_{HCOO}\theta_{HCO} - k_{-5}P_{H_2}P_{CO}P_{CO_2}{\theta_{S^*}}^4 \quad (4.16)$$

$$rate_{tot} = k_5\theta_{HCOO}\theta_{HCO} \quad (4.17)$$

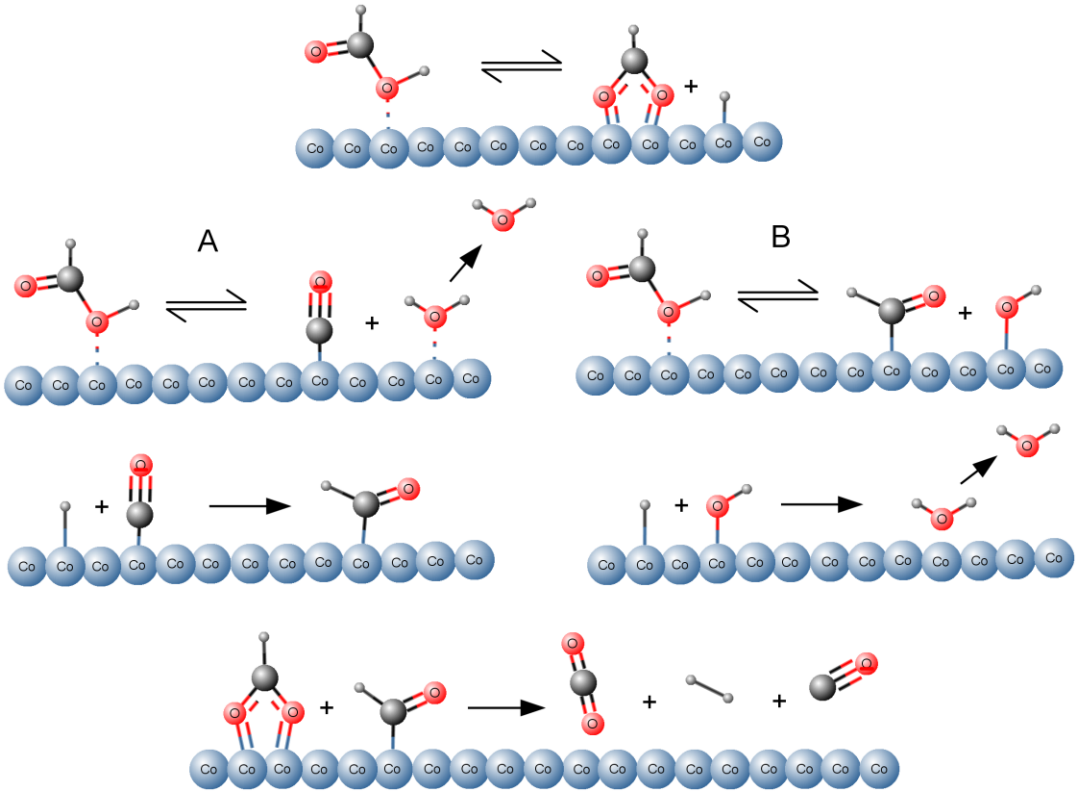

Figure 4.5: Illustration of the proposed mechanism for reaction (4.10).

Where θ_{S^*} is the concentration of available surface sites and is defined as the following:

$$\theta_{S^*} = 1 - \left(\theta_{HCOO} + \theta_{HCO} + \theta_{H} + \theta_{CO} \quad + \theta_{H_2O}\right) \tag{4.18}$$

The total number of surface sites can be estimated by summing the integration of the pressure of all products seen in the TPD for the exposures 1 L and above, correcting for the number of sites each molecule would occupy. For exposures 1 L and above, we observe the development of multi-layer peaks for formic acid and the selectivity of the reactions remains constant, this suggests that monolayer coverage has been achieved, therefore all surface sites occupied.

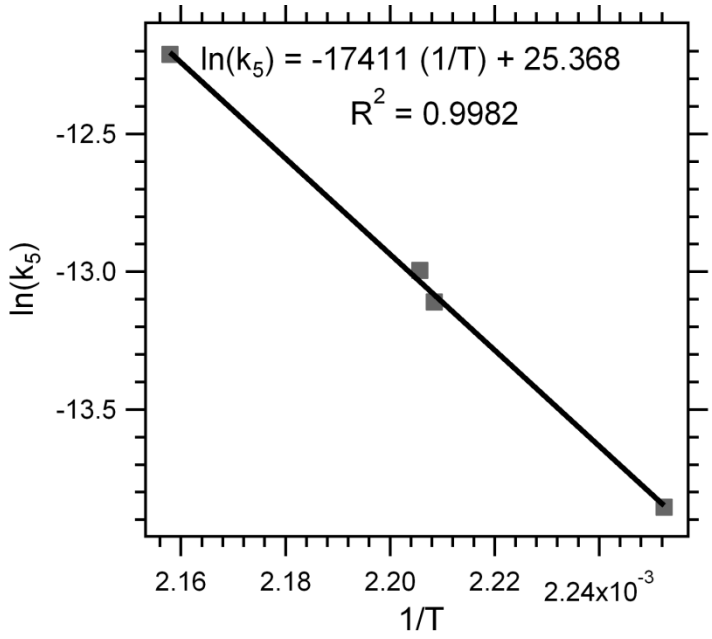

Figure 4.6: Fitted plot of ln(k_5) vs. 1/T at θ_{HCOO} = 0.15.

Surface coverage calculations assumed CO, H_2, HCOO, HCO, and H_2O occupied two surface atoms. CO_2 was used to find the rate of reactions as CO_2 adsorbs very weakly to the surface and has the lowest adsorption temperature of the products. A complete analysis was used to find the reaction energies and pre-exponential factors.[73] Only temperatures below the reaction peak at 475 K were used in the calculations in order to minimize the effects of the reverse water-gas shift reaction (4.9).The rates of reaction were found using the intensity of the CO_2 pressure at a temperature multiplied by the temperature ramp to give a reaction rate in units of CO_2 mbar/s. Using equation (4.17), the forward rate constant, k_5, was calculated at varying surface coverages for each exposure to obtain accurate values. Then plotting the ln(k_5) verses 1/T, the activation energies and pre-exponential factors were found for θ_{HCOO} = 0.15 - 0.1. Figure 4.6 shows the graph for θ_{HCOO} = 0.15. The activation energies and pre-exponential factors for reaction (4.15) are relatively constant for the coverages observed and well within experimental error. This suggests that there is no dependency on surface coverage within this range. The activation energy and pre-exponential factor are 147.2 ± 2.0 kJ/mol and $10^{11.3 \pm 0.2}$ mbar/s.

Table 4.1: Desorption energies of observed species calculated by Redhead analysis.

Species	Temperature (K)	υ_{des}[a]	Ea (kJ/mol)
Formic acid monolayer	230[b]	$10^{15.2}$	68.5 ± 1.5
Second layer	198	$10^{15.1}$	57.9 ± 3.1
Multilayer	178	$10^{15.0}$	52.2
Water	200	$10^{14.4}$	56.0 ± 2.4
Hydrogen (H_2)	370	$10^{14.3}$	105.3 ± 0.4
Carbon monoxide	450[c]	$10^{14.9}$	134.1 ± 1.3

[a]Preexponential factor derived by the method of Campbell et al.[71]
[b]Associative desorption.
[c]Reported associative desorption.[59]

4.5 Conclusion

Formic acid molecularly adsorbs on to cobalt below 160 K. However, a fraction of formic acid dissociates with carboxyl and formyl as intermediates, even at 110 K. Molecular formic acid decomposes to form formate above 160 K. The decomposition continues at low temperature as seen by the release of water at 200 K, its normal desorption temperature. Adsorbed hydrogen desorbs from the surface at 370 K, and adsorbed CO desorbs at 450-460 K. At 470-480 K the formate species reacts with formyl through a Langmuir-Hinshelwood mechanism in the rate limiting step (4.16) of the overall reaction (4.10). Desorption energies for all the components are reported, and the kinetic parameters for the reaction have been measured as: activation energy = 147.2 ± 2.0 kJ/mol and pre-exponential factor = $10^{11.3 \pm 0.2}$ mbar/s.

4.6 References

(1) El-Nagar, G. A.; Mohammad, A. M.; El-Deab, M. S.; Ohsaka, T.; El-Anadouli, B. E. Acrylonitrile-Contamination Induced Enhancement of Formic Acid Electro-Oxidation at Platinum Nanoparticles Modified Glassy Carbon Electrodes. *J. Power Sources* **2014**, *265*, 57–61.

(2) Choy M., M.; Hahn, F.; Léger, J.-M.; Lamy, C.; Ortega, J. M. In Situ Fourier Transformed Infrared Reflectance Spectroscopy Study of the Effect of Poly-pDMB Film Modified Platinum Electrodes on the Electrooxidation of Formic Acid. *Thin Solid Films* **2007**, *515*, 3611–3618.

(3) Habibi, B.; Delnavaz, N. Electrocatalytic Oxidation of Formic Acid and Formaldehyde on Platinum Nanoparticles Decorated Carbon-Ceramic Substrate. *Int. J. Hydrogen Energy* **2010**, *35*, 8831–8840.

(4) WANG, Z.; QIU, K. Electrocatalytic Oxidation of Formic Acid on Platinum Nanoparticle Electrode Deposited on the Nichrome Substrate. *Electrochem. commun.* **2006**, *8*, 1075–1081.

(5) Zhou, X.; Liu, C.; Liao, J.; Lu, T.; Xing, W. Platinum-Macrocycle Co-Catalysts for Electro-Oxidation of Formic Acid. *J. Power Sources* **2008**, *179*, 481–488.

(6) Marković, N. M.; Gasteiger, H. A.; Ross, P. N.; Jiang, X.; Villegas, I.; Weaver, M. J. Electro-Oxidation Mechanisms of Methanol and Formic Acid on Pt-Ru Alloy Surfaces. *Electrochim. Acta* **1995**, *40*, 91–98.

(7) Luo, Q.; Feng, G.; Beller, M.; Jiao, H. Formic Acid Dehydrogenation on Ni(111) and Comparison with Pd(111) and Pt(111). *J. Phys. Chem. C* **2012**, *116*, 4149–4156.

(8) Mazurkiewicz, M.; Malolepszy, A.; Mikolajczuk, A.; Stobinski, L.; Borodzinski, A.; Lesiak, B.; Zemek, J.; Jiricek, P. Pd/MWCNTs Catalytic Activity in the Formic Acid Electrooxidation Dependent on Catalyst Surface Treatment. *Phys. Status Solidi* **2011**, *248*, 2516–2519.

(9) Brandt, K.; Steinhausen, M.; Wandelt, K. Catalytic and Electro-Catalytic Oxidation of Formic Acid on the Pure and Cu-Modified Pd(111)-Surface. *J. Electroanal. Chem.* **2008**, *616*, 27–37.

(10) Mellinger, Z. J.; Kelly, T. G.; Chen, J. G. Pd-Modified Tungsten Carbide for Methanol Electro-Oxidation: From Surface Science Studies to Electrochemical Evaluation. *ACS Catal.* **2012**, *2*, 751–758.

(11) Hosseini, H.; Mahyari, M.; Bagheri, A.; Shaabani, A. Pd and PdCo Alloy Nanoparticles Supported on Polypropylenimine Dendrimer-Grafted Graphene: A Highly Efficient

Anodic Catalyst for Direct Formic Acid Fuel Cells. *J. Power Sources* **2014**, *247*, 70–77.

(12) Zhang, L.; Wan, L.; Ma, Y.; Chen, Y.; Zhou, Y.; Tang, Y.; Lu, T. Crystalline Palladium–cobalt Alloy Nanoassemblies with Enhanced Activity and Stability for the Formic Acid Oxidation Reaction. *Appl. Catal. B Environ.* **2013**, *138-139*, 229–235.

(13) Himeda, Y.; Miyazawa, S.; Hirose, T. Interconversion between Formic Acid and H(2)/CO(2) Using Rhodium and Ruthenium Catalysts for CO(2) Fixation and H(2) Storage. *ChemSusChem* **2011**, *4*, 487–493.

(14) Czaun, M.; Goeppert, A.; May, R.; Haiges, R.; Prakash, G. K. S.; Olah, G. A. Hydrogen Generation from Formic Acid Decomposition by Ruthenium Carbonyl Complexes. Tetraruthenium Dodecacarbonyl Tetrahydride as an Active Intermediate. *ChemSusChem* **2011**, *4*, 1241–1248.

(15) Czaun, M.; Goeppert, A.; Kothandaraman, J.; May, R. B.; Haiges, R.; Prakash, G. K. S.; Olah, G. A. Formic Acid As a Hydrogen Storage Medium: Ruthenium-Catalyzed Generation of Hydrogen from Formic Acid in Emulsions. *ACS Catal.* **2014**, *4*, 311–320.

(16) Abdur-Rashid, K.; Clapham, S. E.; Hadzovic, A.; Harvey, J. N.; Lough, A. J.; Morris, R. H. Mechanism of the Hydrogenation of Ketones Catalyzed by Trans-Dihydrido(diamine)ruthenium(II) Complexes †. *J. Am. Chem. Soc.* **2002**, *124*, 15104–15118.

(17) Rice, C. Catalysts for Direct Formic Acid Fuel Cells. *J. Power Sources* **2003**, *115*, 229–235.

(18) Fellay, C.; Dyson, P. J.; Laurenczy, G. A Viable Hydrogen-Storage System Based on Selective Formic Acid Decomposition with a Ruthenium Catalyst. *Angew. Chem. Int. Ed. Engl.* **2008**, *47*, 3966–3968.

(19) Menashe, N.; Shvo, Y. Catalytic Disproportionation of Aldehydes with Ruthenium Complexes. *Organometallics* **1991**, *10*, 3885–3891.

(20) Himeda, Y.; Miyazawa, S.; Hirose, T. Interconversion between Formic Acid and H(2)/CO(2) Using Rhodium and Ruthenium Catalysts for CO(2) Fixation and H(2) Storage. *ChemSusChem* **2011**, *4*, 487–493.

(21) Loges, B.; Boddien, A.; Junge, H.; Beller, M. Controlled Generation of Hydrogen from Formic Acid Amine Adducts at Room Temperature and Application in H2/O2 Fuel Cells. *Angew. Chem. Int. Ed. Engl.* **2008**, *47*, 3962–3965.

(22) Johnson, T. C.; Morris, D. J.; Wills, M. Hydrogen Generation from Formic Acid and Alcohols Using Homogeneous Catalysts. *Chem. Soc. Rev.* **2010**, *39*, 81–88.

(23) Fukuzumi, S.; Kobayashi, T.; Suenobu, T. Efficient Catalytic Decomposition of Formic

Acid for the Selective Generation of H2 and H/D Exchange with a Water-Soluble Rhodium Complex in Aqueous Solution. *ChemSusChem* **2008**, *1*, 827–834.

(24) King, R. B.; Bhattacharyya, N. K. Catalytic Reactions of Formate 4. A Nitrite-Promoted Rhodium (III) Catalyst for Hydrogen Generation from Formic Acid in Aqueous Solution. *Inorganica Chim. Acta* **1995**, *237*, 65–69.

(25) Balan, B. K.; Sathe, B. R. Significant Enhancement of Formic Acid Oxidation Using Rhodium Nanostructures. *J. Nanosci. Nanotechnol.* **2012**, *12*, 8994–8998.

(26) Somasunderam, A.; Alper, H. Use of Rhodium on Carbon and 1,3-Bis(diphenylphosphino)propane to Catalyze the Regioselective Hydroformylation of Alkenes with Formic Acid as the Hydrogen Source. *J. Mol. Catal.* **1994**, *92*, 35–40.

(27) Horozova, E.; Dimcheva, N.; Miteva, M.; Jordanova, Z. Rhodium Deposits on Graphite: The Impact of the Graphite Pad on the Electrocatalytic Activity in the Electrooxidation of Formic Acid. *Bulg. Chem. Commun. 40*, 129–136.

(28) Guseva, E. V.; Sokolova, A. V.; Saifutdinov, A. M.; Naumova, A. A.; Polovnyak, V. K. Kinetics of Homogeneous Dehydrogenation of Formic Acid in the Presence of Supramolecular rhodium(III) Complex with P-Functionalized calix[4]resorcine. *Russ. J. Gen. Chem.* **2012**, *82*, 827–834.

(29) De Martinez, M. C.; Beden, B.; Hahn, F.; Lamy, C. Effect of the Bulk Concentration of Formic Acid on the Distribution of the Adsorbates at a Smooth Rhodium Electrode in Acid Medium□: An EMIRS Investiga. *J. Electron Spectros. Relat. Phenomena* **1987**, *45*, 153–160.

(30) Fukuzumi, S.; Kobayashi, T.; Suenobu, T. Efficient Catalytic Decomposition of Formic Acid for the Selective Generation of H2 and H/D Exchange with a Water-Soluble Rhodium Complex in Aqueous Solution. *ChemSusChem* **2008**, *1*, 827–834.

(31) Wang, Z.-L.; Ping, Y.; Yan, J.-M.; Wang, H.-L.; Jiang, Q. Hydrogen Generation from Formic Acid Decomposition at Room Temperature Using a NiAuPd Alloy Nanocatalyst. *Int. J. Hydrogen Energy* **2014**, *39*, 4850–4856.

(32) Assaud, L.; Monyoncho, E.; Pitzschel, K.; Allagui, A.; Petit, M.; Hanbücken, M.; Baranova, E. A.; Santinacci, L. 3D-Nanoarchitectured Pd/Ni Catalysts Prepared by Atomic Layer Deposition for the Electrooxidation of Formic Acid. *Beilstein J. Nanotechnol.* **2014**, *5*, 162–172.

(33) Chang, J.; Feng, L.; Liu, C.; Xing, W.; Hu, X. An Effective Pd-Ni(2)P/C Anode Catalyst for Direct Formic Acid Fuel Cells. *Angew. Chem. Int. Ed. Engl.* **2014**, *53*, 122–126.

(34) Benziqer, J. B.; Schoofs, G. R. Influence of Adsorbate Interactions on Heterogeneous Reaction Kinetics. Formic Acid Decomposition on Nickel. *J. Phys. Chem.* **1984**, *88*,

4439–4444.

(35) Joyner, R. W.; Roberts, M. W. Photoelectron Spectroscopic Investigation of the Adsorption and Catalytic Decomposition of Formic Acid by Copper, Nickel and Gold. *Proc. R. Soc. A Math. Phys. Eng. Sci.* **1976**, *350*, 107–126.

(36) Hirota, K.; Kuwata, K.; Nakai, Y. Infrared Studies of Formic Acid, Chemisorbed on Copper, Nickel and Zinc. *Bull. Chem. Soc. Jpn.* **1958**, *31*, 861–864.

(37) IGLESIA, E. Decomposition of Formic Acid on Copper, Nickel, and Copper-Nickel Alloys I. Preparation and Characterization of Catalysts. *J. Catal.* **1983**, *81*, 204–213.

(38) Haq, S.; Love, J. G.; Sanders, H. E.; King, D. A. Adsorption and Decomposition of Formic Acid on Ni{110}. *Surf. Sci.* **1995**, *325*, 230–242.

(39) IGLESIA, E. Decomposition of Formic Acid on Copper, Nickel, and Copper-Nickel Alloys II. Catalytic and Temperature-Programmed Decomposition of Formic Acid on Cu/SiO2, Cu/Al2O3, and Cu Powder. *J. Catal.* **1983**, *81*, 214–223.

(40) Columbia, M. R.; Thiel, P. A. The Interaction of Formic Acid with Transition Metal Surfaces, Studied in Ultrahigh Vacuum. *J. Electroanal. Chem.* **1994**, *369*, 1–14.

(41) Xu, J.; Yuan, D.; Yang, F.; Mei, D.; Zhang, Z.; Chen, Y.-X. On the Mechanism of the Direct Pathway for Formic Acid Oxidation at a Pt(111) Electrode. *Phys. Chem. Chem. Phys.* **2013**, *15*, 4367–4376.

(42) Hosseini, H.; Mahyari, M.; Bagheri, A.; Shaabani, A. Pd and PdCo Alloy Nanoparticles Supported on Polypropylenimine Dendrimer-Grafted Graphene: A Highly Efficient Anodic Catalyst for Direct Formic Acid Fuel Cells. *J. Power Sources* **2014**, *247*, 70–77.

(43) Yin, M.; Li, Q.; Jensen, J. O.; Huang, Y.; Cleemann, L. N.; Bjerrum, N. J.; Xing, W. Tungsten Carbide Promoted Pd and Pd–Co Electrocatalysts for Formic Acid Electrooxidation. *J. Power Sources* **2012**, *219*, 106–111.

(44) Stevanović, S.; Babić-Samardžija, K.; Sovilj, S. P.; Tripković, A.; Jovanović, V. M. Oxidation of Formic Acid on Platinum Surfaces Decorated with cobalt(III) Macrocyclic Complexes. *Russ. J. Phys. Chem. A* **2009**, *83*, 1442–1446.

(45) Inglis, H. S.; Taylor, D. Decomposition of Formic Acid on Titanium, Vanadium, Chromium, Manganese, Iron, Cobalt, Nickel, and Copper. *J. Chem. Soc. A Inorganic, Phys. Theor.* **1969**, 2985.

(46) Toomes, R.; King, D. Potassium-Promoted Synthesis of Surface Formate and Reactions of Formic Acid on Co {1010}. *Surf. Sci.* **1996**, 43–64.

(47) Lewis, W. F. Magnetic Domain Behavior during the Hcp-to-Fcc Phase Transition in

Cobalt Using Lorentz Electron Microscopy. *J. Appl. Phys.* **1977**, *48*, 2980.

(48) Bidaux, J. E. Study of the H.c.p.-F.c.c. Phase Transition in Cobalt by Acoustic Measurements. *Acta Metall. 37*, 803–811.

(49) Didziulis, S. V.; Kim, H. I. Chemistry of Methyl Formate with TiC(100): Comparison of Experiment with Density Functional Calculations. *J. Phys. Chem. C* **2007**, *111*, 11275–11284.

(50) Frantz, P.; Kim, H. I.; Didziulis, S. V.; Li, S.; Chen, Z.; Perry, S. S. Reaction of Methyl Formate with VC(100) and TiC(100) Surfaces. *Surf. Sci.* **2005**, *596*, 144–162.

(51) Huang, J. Y.; Huang, H. G.; Lin, K. Y.; Liu, Q. P.; Sun, Y. M.; Xu, G. Q. The Structures of Physisorbed and Chemisorbed Formic Acid on Si(111)-7×7. *Surf. Sci.* **2004**, *549*, 255–264.

(52) Bowker, M.; Madix, R. J. XPS, UPS and Thermal Desorption Studies of the Reactions of Formaldehyde and Formic Acid with the Cu(110) Surface. *Surf. Sci.* **1981**, *102*, 542–565.

(53) Tanaka, K.; Matsuzaki, S.; Toyoshima, I. Photodecomposition of Adsorbed Methoxy Species by UV Light and Formaldehyde Adsorption on silicon(111) Studied by XPS and UPS. *J. Phys. Chem.* **1993**, *97*, 5673–5677.

(54) Fu, P.; Zhang, P. Characterization of Pt-TiO2 Film Used in Three Formaldehyde Photocatalytic Degradation Systems: UV254 Nm, O3+UV254 Nm and UV254+185 Nm via X-Ray Photoelectron Spectroscopy. *Chinese J. Catal.* **2014**, *35*, 210–218.

(55) Zafeiratos, S.; Dintzer, T.; Teschner, D.; Blume, R.; Hävecker, M.; Knop-Gericke, A.; Schlögl, R. Methanol Oxidation over Model Cobalt Catalysts: Influence of the Cobalt Oxidation State on the Reactivity. *J. Catal.* **2010**, *269*, 309–317.

(56) Attard, G. A.; Chibane, K.; Ebert, H. D.; Parsons, R. The Adsorption and Decomposition of Methanol on Pt(110). *Surf. Sci.* **1989**, *224*, 311–326.

(57) Shen, M.; Zaera, F. Methanol Adsorption on Clean and Oxygen-Predosed V(100) Single-Crystal Surfaces. *J. Phys. Chem. C* **2008**, *112*, 1636–1644.

(58) Shen, M.; Zaera, F. Coupling Reactions in Aldehydes Adsorbed on V(100) Single-Crystal Surfaces. *J. Am. Chem. Soc.* **2009**, *131*, 8708–8713.

(59) Wesner, D. A.; Linden, G.; Bonzel, H. P. Alkali Promotion on Cobalt: Surface Analysis of the Effects of Potassium on Carbon Monoxide Adsorption and Fischer-Tropsch Reaction. *Appl. Surf. Sci.* **1986**, *26*, 335–356.

(60) Chtaïb, M.; Delrue, J. P.; Caudano, R. Decomposition of HCOOH on Gold Studied by XPS and TDS Spectroscopies and Its Behaviour Under Very Low Energy Electron

Excitation. *Phys. Scr.* **1983**, *T4*, 133–137.

(61) Search, H.; Journals, C.; Contact, A.; Iopscience, M.; Address, I. P. The Reactive Chemisorption of Formic Acid at Al (111) Surfaces and the Influence of Surface Oxidation and Coadsorption with Water□: A Combined XPS and HREELS Investigation. **1991**, *237*.

(62) Hung, W.-H.; Bernasek, S. L. The Adsorption and Decomposition of Formaldehyde and Formic Acid on the Clean and Modified Fe (100) Surface. *Surf. Sci.* **1996**, *346*, 165–188.

(63) Yurderi, M.; Bulut, A.; Zahmakiran, M.; Kaya, M. Carbon Supported Trimetallic PdNiAg Nanoparticles as Highly Active, Selective and Reusable Catalyst in the Formic Acid Decomposition. *Appl. Catal. B Environ.* **2014**, *160-161*, 514–524.

(64) Qi, Y.; Zhu, R.; Zhang, D. Adsorption Behaviors of Monomer and Dimer of Formic Acid on Pt (111) in the Absence and Presence of Water. *J. Mol. Model.* **2014**, *20*, 2264.

(65) Xu, M.; Noei, H.; Buchholz, M.; Muhler, M.; Wöll, C.; Wang, Y. Dissociation of Formic Acid on Anatase TiO 2 (1 0 1) Probed by Vibrational Spectroscopy. *Catal. Today* **2012**, *182*, 12–15.

(66) US Department of Commerce, N. NIST Standard Reference Database 1A v14.

(67) Smith R J, B.; Loganathan, M.; Shantha, M. S. A Review of the Water Gas Shift Reaction Kinetics. *Int. J. Chem. React. Eng.* **2010**, *8*.

(68) Zhang, C.; Li, S.; Wu, G.; Huang, Z.; Han, Z.; Wang, T.; Gong, J. Steam Reforming of Ethanol over Skeletal Ni-Based Catalysts: A Temperature Programmed Desorption and Kinetic Study. *AIChE J.* **2014**, *60*, 635–644.

(69) Vesselli, E.; Rizzi, M.; De Rogatis, L.; Ding, X.; Baraldi, A.; Comelli, G.; Savio, L.; Vattuone, L.; Rocca, M.; Fornasiero, P.; et al. Hydrogen-Assisted Transformation of CO 2 on Nickel: The Role of Formate and Carbon Monoxide. *J. Phys. Chem. Lett.* **2010**, *1*, 402–406.

(70) Vesselli, E.; Schweicher, J.; Bundhoo, A.; Frennet, A.; Kruse, N. Catalytic CO 2 Hydrogenation on Nickel: Novel Insight by Chemical Transient Kinetics †. *J. Phys. Chem. C* **2011**, *115*, 1255–1260.

(71) Campbell, C. T.; Árnadóttir, L.; Sellers, J. R. V. Kinetic Prefactors of Reactions on Solid Surfaces. *Zeitschrift für Phys. Chemie* **2013**, *227*, 1435–1454.

(72) Nakao, F. Determination of the Ionization Gauge Sensitivity Using the Relative Ionization Cross-Section. *Vacuum* **1975**, *25*, 431–435.

(73) Kolasinski, K. K.; Kolasinski, K. W. *Surface Science: Foundations of Catalysis and*

Nanoscience; John Wiley & Sons, 2012; p. 574.

Chapter 5:

Engineering PM-IRRAS Reactor for Incorporation into UHV Vessel

5.0 Engineering PM-IRRAS Reactor for Incorporation into UHV Vessel

This chapter describes and gives technical drawings of a Polarization Modulation InfraRed Reflective Absorption Spectrometer (PM-IRRAS) reactor and a heat exchanger that was engineered as part of this thesis. The reactor is UltraHigh Vacuum (UHV) compatible and equipped with a PM-IRRAS for the characterization of surfaces in either UHV or high pressure systems. An introduction on infrared spectroscopy will also be given with interest in Fourier-Transform Infrared, Infrared Reflective Absorption, and PM-IRRAS. The heat exchanger is designed to connect the in situ liquid nitrogen cooling lines of either the PM-IRRAS reactor or the existing UHV vessel, to a high pressure (350 psia) liquid nitrogen Dewar.

5.1 Infrared Spectroscopy

Vibrational spectroscopy is a very important tool for the investigation of molecular adsorbates that form on metal surfaces during the course of chemical reactions, especially useful for the identification of intermediates in catalytic reactions. Infrared spectroscopy (IR), in its many incarnations, is probably the most appropriate type of vibrational spectroscopy for characterizing catalyst systems. As when compared to other surface techniques, like Raman spectroscopy or high-resolution electron energy loss, IR has a high surface sensitivity and resolution, approximately 0.1% of a monolayer of CO and ~1 cm^{-1} respectively.[1] IR can investigate any reflective surface, including model single crystals to industrial catalysts, under UHV or more realistic pressures. IR principle of operation is based on the vibrational excitement of molecules by the adsorption of infrared light. The vibrational spectra, obtained from IR, are related to the chemical nature of the observed chemical species, and thus it is possible to differentiate the adsorbed molecules, substrate, and adsorbate-adsorbate interactions.

Fourier-transform InfraRed (FTIR) spectrometers, such as the one incorporated into the PM-IRRAS reactor, measures an interference signal of a two-beam interferometer, also known as a traditional Michelson interferometer[2], and thus allows for the simultaneous detection of all observed frequencies. FTIRs consist of a beam splitter, fixed mirror, and moving mirror. The collimated (parallel beam) IR beam is split into two parts by the beam splitter, one part goes to the moving mirror and the other part goes to the fixed mirror. The reflected beams either constructively or destructively interfere with each other, which depends on the wavelength of the light and the so called retardation, δ. δ is the difference between the optical paths experienced by the two split beams between the mirror and the detector. δ is thus a variable of the beam intensity $I(\delta)$, known as a interferogram. If the difference between the split beams is zero, $\delta = 0$, constructive interference occurs leading to a maximum in the interferogram.[1] For all other values of δ a partial or total destructive interference occurs, which results in a fast oscillation decrease on both sides of the maximum in the interferogram. The interferogram is then converted to a traditional spectrum via Fourier-transform, hence FTIR name. Figure 5.1 shows an example of an interferogram and spectrum.

InfraRed Reflection Absorption Spectroscopy (IRRAS/IRAS), also known as Reflective Adsorption InfraRed Spectroscopy (RAIRS) measures the vibrations of molecules adsorbed on a planar surface (that reflects IR light) by the reflecting the IR beam off the surface at an angle of around 7^{o} from the surface.[1] The vibrational spectra of adsorbed molecules are normally different from the corresponding gas phase spectra, the observed frequencies, peak shapes, widths, and intensities are influenced by the interaction of the adsorbate and substrate. From this data it is possible to determine the adsorption state and adsorption geometry of the molecules.[1] Unfortunately IRRAS, although not theoretically, is practically speaking limited to UHV

conditions, as pressure increases (above 10^{-3} mbar)[1] the gas phase contribution typically obscures the much smaller contribution of adsorbed species.

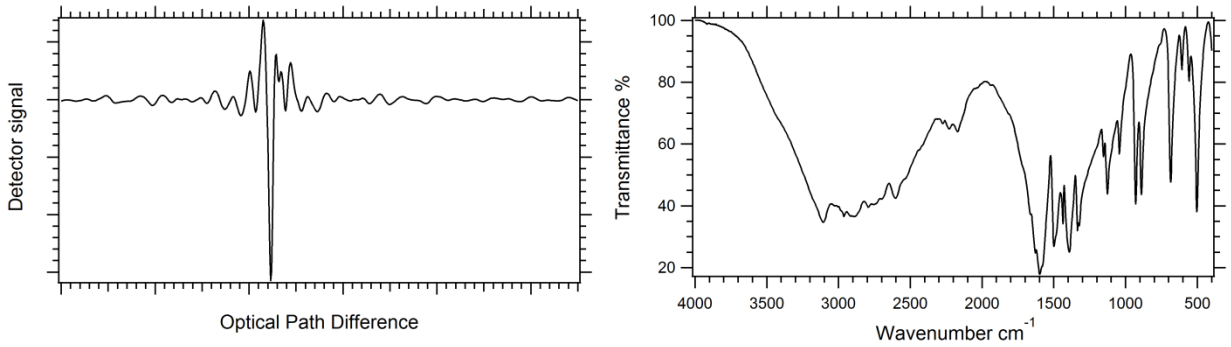

Figure 5.1: (Left) Interferogram of glycin (Right) Transmittance spectrum of glycin.

A technique that is able differentiate the adsorption contribution from the isotropic gas phase contribution is needed to probe high pressure systems. This is achieved through the use of PM-IRRAS. This technique is based on the fact that the absorption of IR light by a molecule adsorbed to a metal surface is influenced by the dielectric behaviour of the metal, producing what is known as the metal surface selection rule (MSSS).[3] Vibrations with a dynamic dipole moment component that is parallel to the surface won't be excited because the metal electrons effectively eliminate the electric field parallel to the surface thereby eliminating the possibility of exciting the parallel dipole moment. Only vibrations with a dynamic dipole moment component that is perpendicular to the surface will be excited and therefore observed. PM-IRRAS capitalizes on this phenomenon by the modulation of a linearly polarized IR beam, which is separated into an electric field that is perpendicular, p-polarized, or parallel, s-polarized to the sample surface. Both the p- and s-polarized light will induce the same excitation from the isotropic gas or liquid phase, but only the p-polarized light will excite the adsorbed molecules in accordance with the MSSS. By subtracting the spectrum obtained by the s-polarized light from the p-polarized spectra, the resulting difference is the contribution of the adsorbed molecules.

Due to the fact that PM-IRRAS relies purely on the MSSS, the medium in which the observation is made does not matter as long as the path is negotiable by IR light. Therefore PM-IRRAS can observe adsorption on metal surfaces at high gas pressure or in liquid mediums.

5.2 Design Considerations

The main objective of this reactor was to add another surface characterization technique to the repertoire of the lab, specifically to incorporate a PM-IRRAS/IRRAS reactor chamber into the multi-technique UHV vessel. There are design constraints and restrictions that follow naturally from the aforementioned objective, which have been separated into two sections; the experimental IRRAS/PM-IRRAS and UHV incorporation considerations.

The experimental requirements are:

- Large variable sample temperature range, from ~130 K to ~2000 K
- Measuring sample temperature and reactor pressure
- Reactor must allow an IR beam to penetrate and exit at a glancing angle to the sample surface
- The introduction of gas phase chemical species
- An IR spectrometer
- An external IR beam path that is not exposed to atmospheric humidity (adsorbed water on optics decreases the intensity of the IR beam thereby decreasing resolution)
- An external IR detector

The incorporation of the reactor into the existing UHV vessel requires:

- Compatibility of sample stage and manipulating arm with sample puck
- Turbo-molecular pump capable of attaining pressures 10^{-10} mbar

- Forepump for turbo-molecular pump
- Chamber must be able to attain UHV pressures and connect to the UHV vessel
- The reactor must have a method of transporting the sample puck from the UHV vessel into the reactor without breaking UHV conditions

With the above considerations and availability of equipment, a number of aspects of the reactor were already available and therefore used in the design. These aspects are as follows; A Bruker Equinox 55 FTIR used for the IR aspect of the reactor; A 18.5" manipulating arm compatible with the pre-existing sample puck and UHV vessel, with a travel of 12"; Copper sample stage with cooling reservoir; Varian TurboV 70 LP turbo-molecular pump and mechanical forepump; Gate valve; and a custom made UHV cube from Kimball Physics.

5.3 Reactor Design

With these requirements the basic reactor starts to take shape. In order to obtain UHV, use the available equipment, and incorporate the reactor into the UHV vessel, the main portion of reactor had to be made of 2.75" Conflat (CF) fittings. Conflat is a fitting type that uses a malleable metal gasket, such as copper or silver, to achieve a UHV seal and these fittings are made of stainless steel as to be UHV compatible. 2.75" CF fittings are the smallest CF fittings that will allow the passage of the sample puck; it is also the flange size of the previously mentioned cube, manipulating arm, gate valve, and turbo-molecular pump.

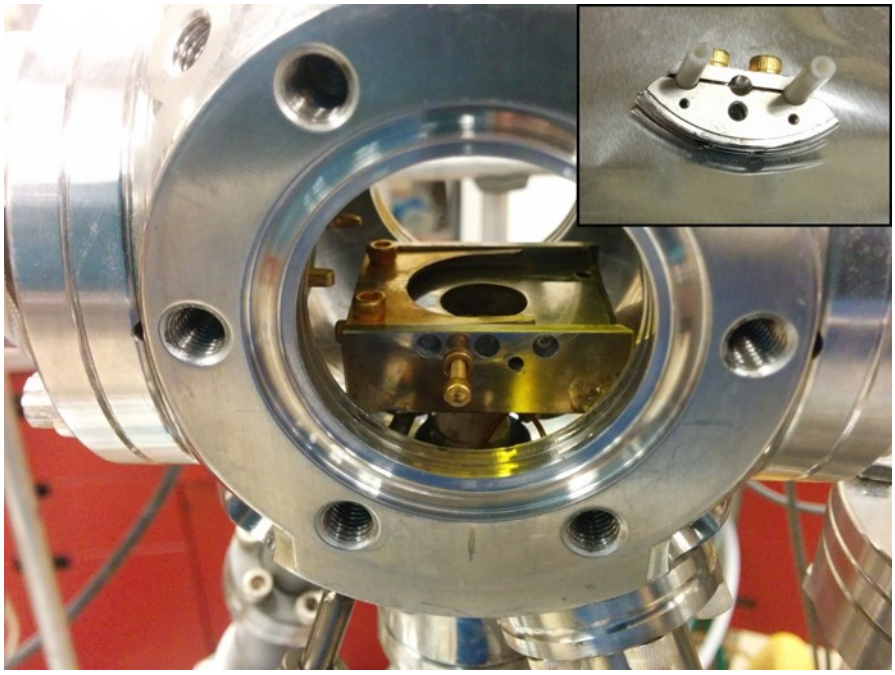

Figure 5.2: Photo of the unsupported sample stage sitting in the cube, with an inset photo of the groove clamps.

The cube is the only plausible place to put the sample stage, as it is the only place the sample stage will fit and also the only place that allows the possibility of a glancing angle for the IR beam. The cube was therefore chosen as the main chamber of the reactor (i.e., where the sample will sit and where the IR beam will contact the sample). The cube has 5 2.75" CF flanges each occupying one face of the cube and 5 1.33" CF flanges clustered on the last face. The sample stage is a copper block with the same horseshoe shape as the main manipulator, described in the experimental chapter, to hold the sample puck and is mounted so the bottom of the stage was above the cluster of 5 1.33" CF flanges of the cube. The sample stage is held in place by two groove clamps that clamp into the grooves on the windows of the cube. Figure 5.2 shows a close up of the sample stage in the cube.

The variable temperature requirement of the reactor was achieved by the addition of a tungsten filament on a 1.33" CF linear motion feedthrough mounted on the center 1.33"CF flange of the cube. The ends of tungsten filament were connected to a 1.33"CF copper wire

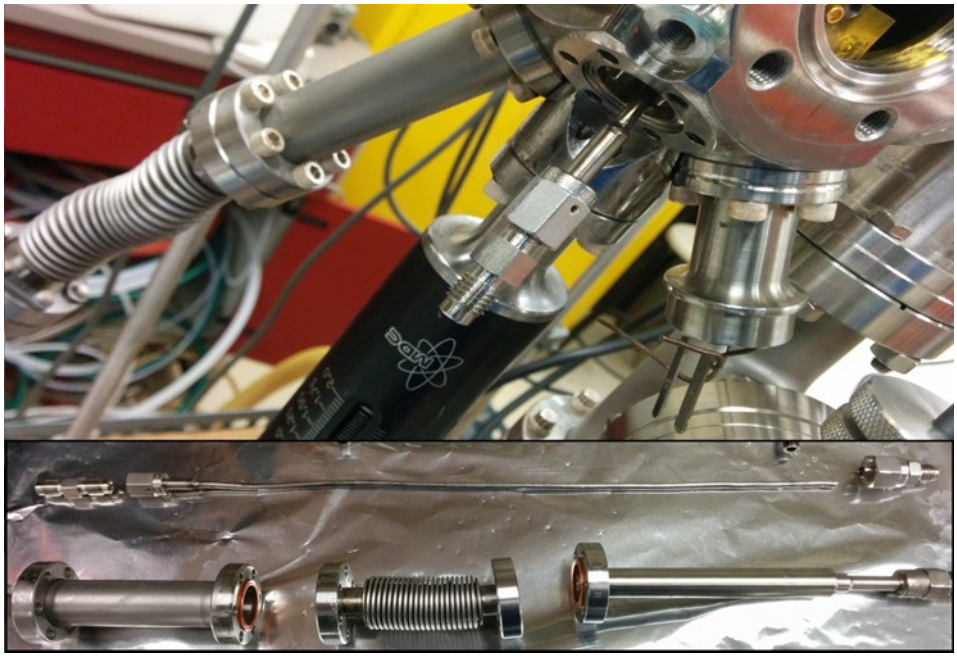

Figure 5.3: Picture of the one of the cooling lines taken apart. Showing how the 1/8" line goes all the way through the CF fittings to connect with the reservoir in the sample stage.

feedthrough that allows current to be placed on the filament, also mounted on one of the 1.33"CF flanges of the cube. These additions allow the filament to be raised up to and bombard the sample with electrons, thereby raising its temperature. The lower end of the variable temperature requirement is met by the addition of liquid nitrogen lines, via a series of connections to a Swagelok feedthrough on two of the 1.33"CF flanges of the cube, connected to the reservoir in the sample stage. The parts involved with the liquid nitrogen cooling system for one set of cooling connections is shown in Figure 5.3. The measurement of this temperature is achieved by the use of an IR temperature gun in concert with a 2.75"CF IR antireflection window. The window is mounted on the top of the cube that is directly above the sample stage. This method was chosen as there was not enough space in the cube for a thermocouple connector to be added.

The IR permeability requirement was met by differentially pumped IR windows. These windows have 2.75”CF flanges and use 38 x 6mm optical crystals, which are mounted by rubber gaskets and have a ¼” tube for differentially pumping. Differentially pumping the windows allows for the exchanging of different optical materials while still achieving UHV conditions in the cube. KBr optical crystals were chosen as the window material, as they have excellent IR transmission, ~90%, for an extremely wide IR range, 0.25-26 μm.[4] These windows are mounted

Figure 5.4: Image of unmounted differentially pumped IR windows with KBr crystals.

on the cube opposite each other on the sides of the sample stage. Figure 5.4 shows an image of the IR windows.

The 2.75”CF manipulating arm, as previously stated, has 12” travel but cannot be too close to the sample stage as the arm has a section that protrudes approximately 5.5” and must be close enough the UHV vessel to transfer a sample. These two requirements, as it turns out, do not physically overlap as such a linear translation section was added between the cube and the arm. When the sample is on the sample stage the linear translation is at its maximum and when the

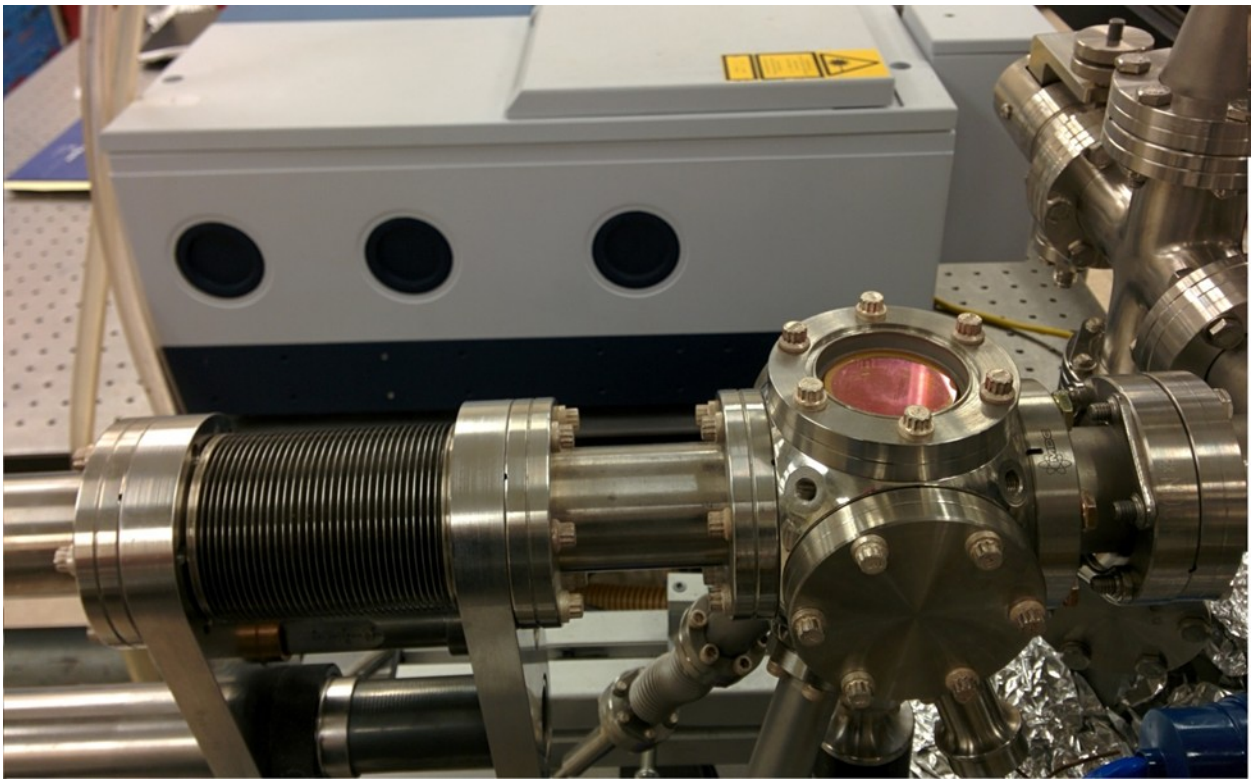

Figure 5.5: Old reactor configuration, showing the anti-reflection IR window on the top of the cube, as well as the linear translation bellows.

sample is being transferred the linear translation is at its minimum.

On the cube opposite the manipulating arm and linear translation section is 2.75" CF cross fitting. Parallel to the cube, on the cross is a gate valve separating the UHV vessel from the reactor. On the cross, perpendicular to the cube is a Pirani/cold cathode pressure gauge with a pressure range of $5x10^{-9}$ mbar to atmosphere, and a 2.75"CF tee fitting. On the tee is a MDC variable leak valve that allows for the introduction of gaseous chemical species, and the previously mentioned Varian turbo-molecular pump.

The equinox 55 IR beam must be at approximately the same level as the sample stage for measurements to occur, but due to the fact that the reactor had to be incorporated into the UHV vessel, the reactor window is about 6-8" higher than the IR when on the optics table. Figure 5.5 shows a version of the reactor and the height difference with the IR. I designed an adjustable IR

stage for the equinox 55 to sit on, that could be mounted on the optical table and moved up to 12” off the table. The IR stage is placed right beside the reactor, so the edge of the plate is about 2” from one of the KBr differentially pumped windows of the cube. On the IR stage is an optical plate beside the external port for the IR beam, which serves as the base for the purge box system and the encased external optical path. The purge box is made of Plexiglas and has a lid on hinges to allow easy access to the optics, as shown in Figure 5.6. I designed a number of additional pieces to build a bracket around the reactor to mount an external detector and ZnSe lens by the opposite KBr differentially pumped window. Thus allowing for the IR beam to follow the external optical path through the purge box to the reactor KBr window reflect of the surface of the sample through the other KBr window and focused by the lens to the external detector.

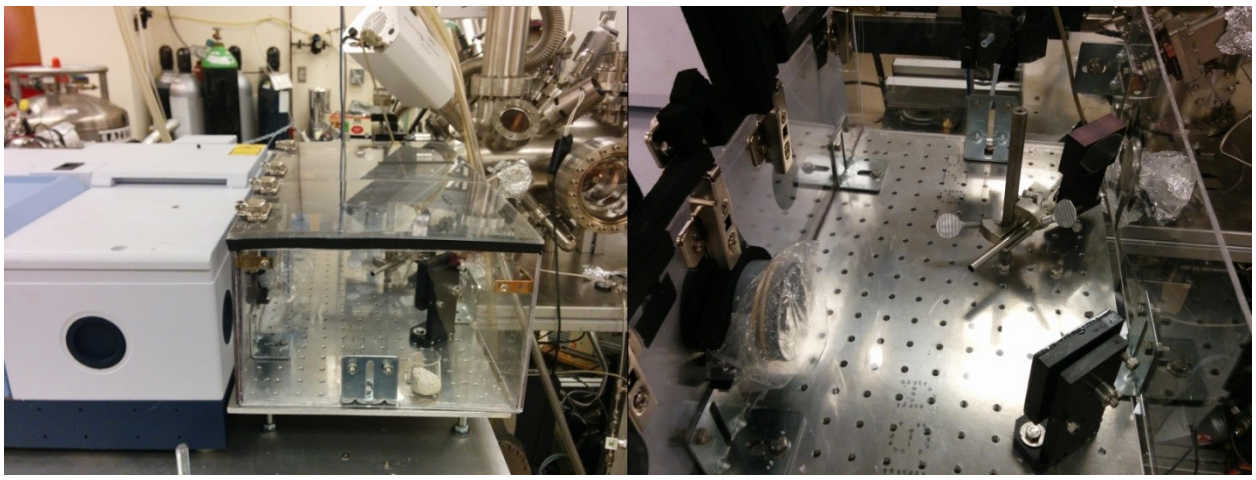

Figure 5.6: (Left) Purge box in place on the IR stage. (Right) Purge box with lid open and optics used in the external optical path.

5.4 Heat Exchanger Design

In comparison to the reactor, the heat exchanger had much less restrictions in its design. It only had to be able to be compatible with the existing liquid nitrogen cooling system, which are two ¼” tubes (one inlet, one outlet) on the end of the main manipulating arm of the UHV vessel. I made a simple counter current shell and tube heat exchanger using an inner tube of 1/8” tubing and an outer shell comprised two small sections of ¼” tubing (to seal around the 1/8”

inner tube) and a 1m long section of 1” flexible insulated tubing as the main shell of the heat exchanger.

5.5 Operation of Reactor

This section will follow the path of a sample that will be used in an IRRAS/PM-IRRAS experiment, starting from a sample that has been mounted and placed inside the UHV chamber on the main manipulating arm.

First the main arm must be moved to x=65, y = 5, z = 19. This positions the sample in the path of the manipulating arm of the reactor. Then the gate valve, separating the XPS chamber and the reactor, must be opened. IT IS IMPORTANT TO NOT OPEN THE GATE VALVE FULLY. If the gate valve is opened fully it will not close. To fix this apply constant pressure to the knob of the gate valve and repetitively strike the gate valve with a rubber mallet. When done correctly, the combination of hitting and applying pressure will make the gate valve slowly slip back into position and be able to close. After the gate valve is open, the linear translation bellows must be moved as close together as possible and then the reactor arm can enter the UHV vessel and be used to transfer the sample puck. When transferring the sample puck caution must be taken, as when the main arm is not in the correct position it will bend the reactor arm, which may damage the arm or sample.

When the sample is on the reactor arm, the linear translation bellows have to be moved as far apart as possible, which makes it possible to transfer the sample from the reactor arm to the sample stage of the reactor. When transferring the puck into the sample stage the sample may fall off the manipulating fork, to avoid this attention must be paid to the puck to see if it is slipping

off the fork and if it is slipping off the fork move the sample back to the UHV vessel and reposition the sample on the fork.

Once the sample is on the reactor sample stage, a cleaning cycle can begin to ensure the sample is free of surface contaminates. The cleaning can be accomplished by raising the filament to 0.25” on the linear motion micrometer and applying a current to the filament feedthroughs. The temperature can be read by an IR temperature gun from the top of the cube. The sample can be confirmed clean by an IRRAS/PM-IRRAS spectrum. After the sample is clean, the cooling can be applied to the reactor to achieve the desired temperature of observation or dosing. If exposure of a gas is required for the experiment it can be achieved by the use of the leak value and the dosage can be obtained by the pressure gauge.

Once the sample is under the required condition for the experiment, the IRRAS/PM-IRRAS spectra can be taken using OPUS FTIR software.

5.6 Technical drawings

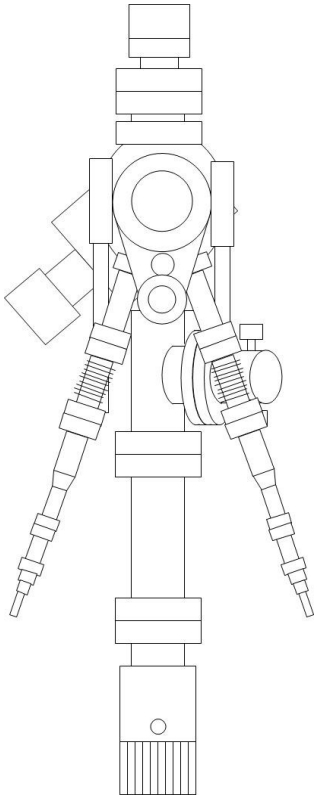

Figure 5.7: Front view of Reactor

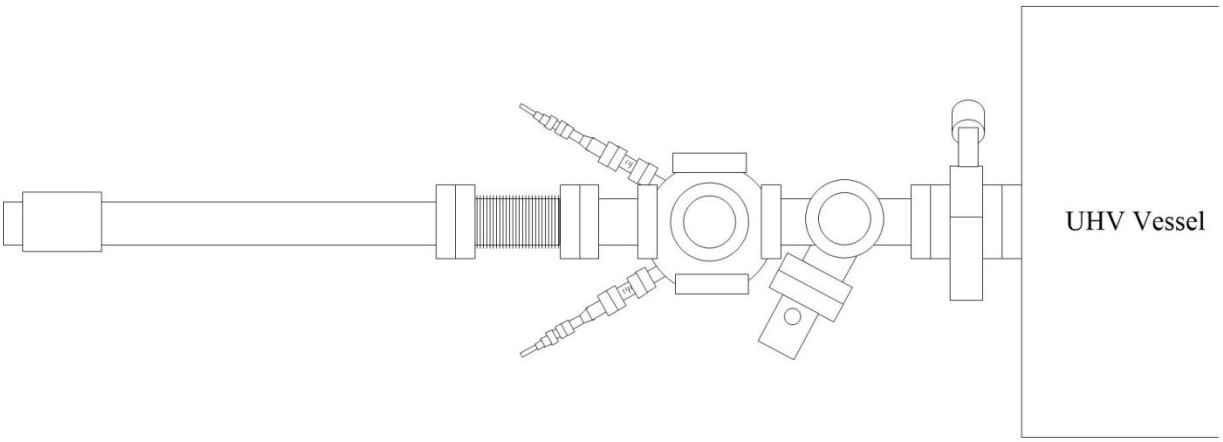

Figure 5.8: Top view of Reactor

1. Manipulating arm
2. Linear translation section
3. Minimum length CF fitting
4. Cube
5. Anti-Reflection IR window
6. Differentially pumped IR window
7. 2 ¾" CF cross fitting
8. Gate valve
9. Pfeiffer PKR 251
10. 2 ¾" CF tee fitting
11. Variable leak valve
12. 2 ¾" CF fitting
13. Varian TurboV 70 LP
14. Wire feedthrough
15. Linear motion feedthrough
16. 1 ⅓" CF fitting
17. 1 ⅓" CF bellows
18. Swaglok feedthrough
19. ¼" Swaglok tubing
20. Liquid nitrogen cooling lines

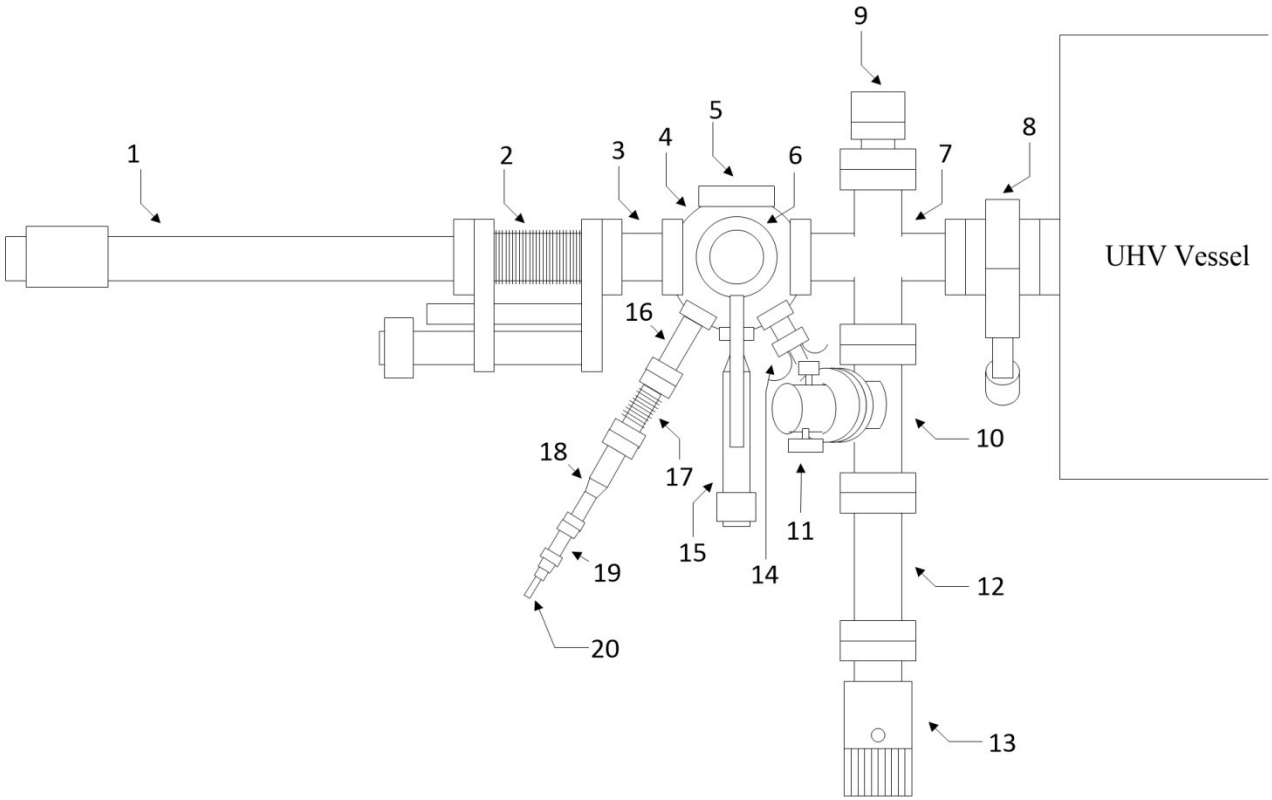

Figure 5.9: Side view of Reactor, with labels

Figure 5.10: Side view of IR stage

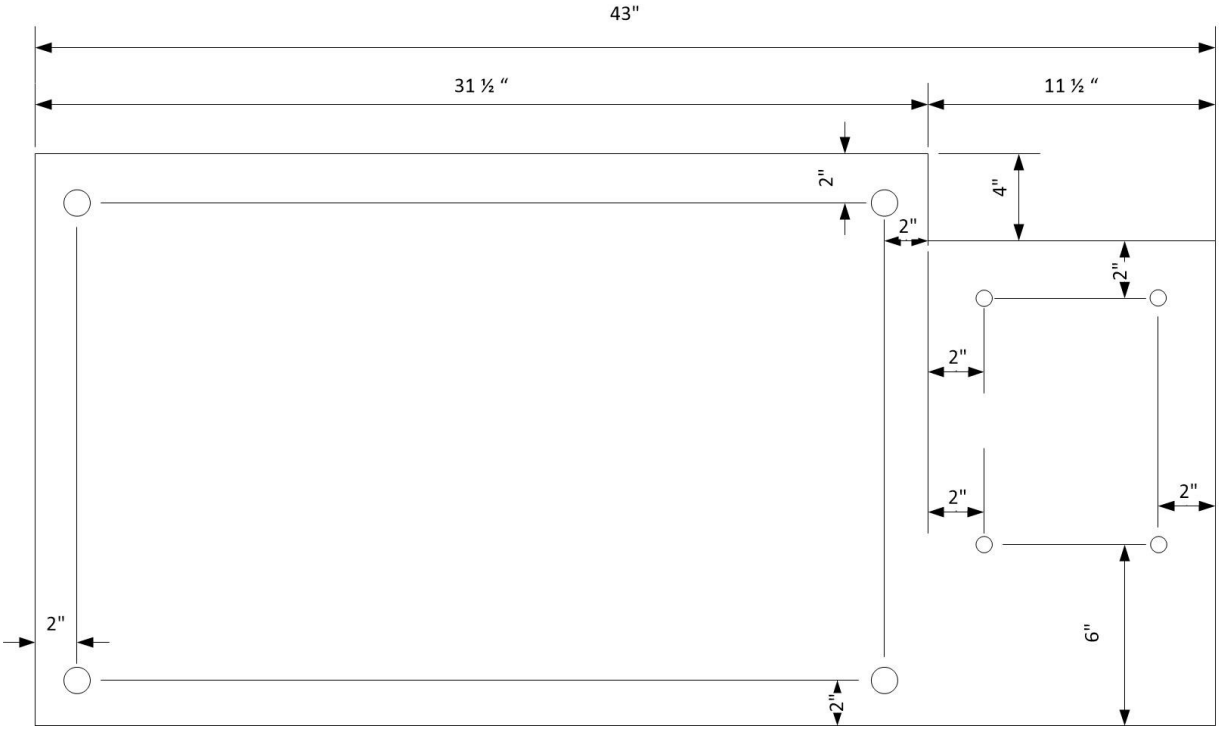

Figure 5.11: Top view of IR stage

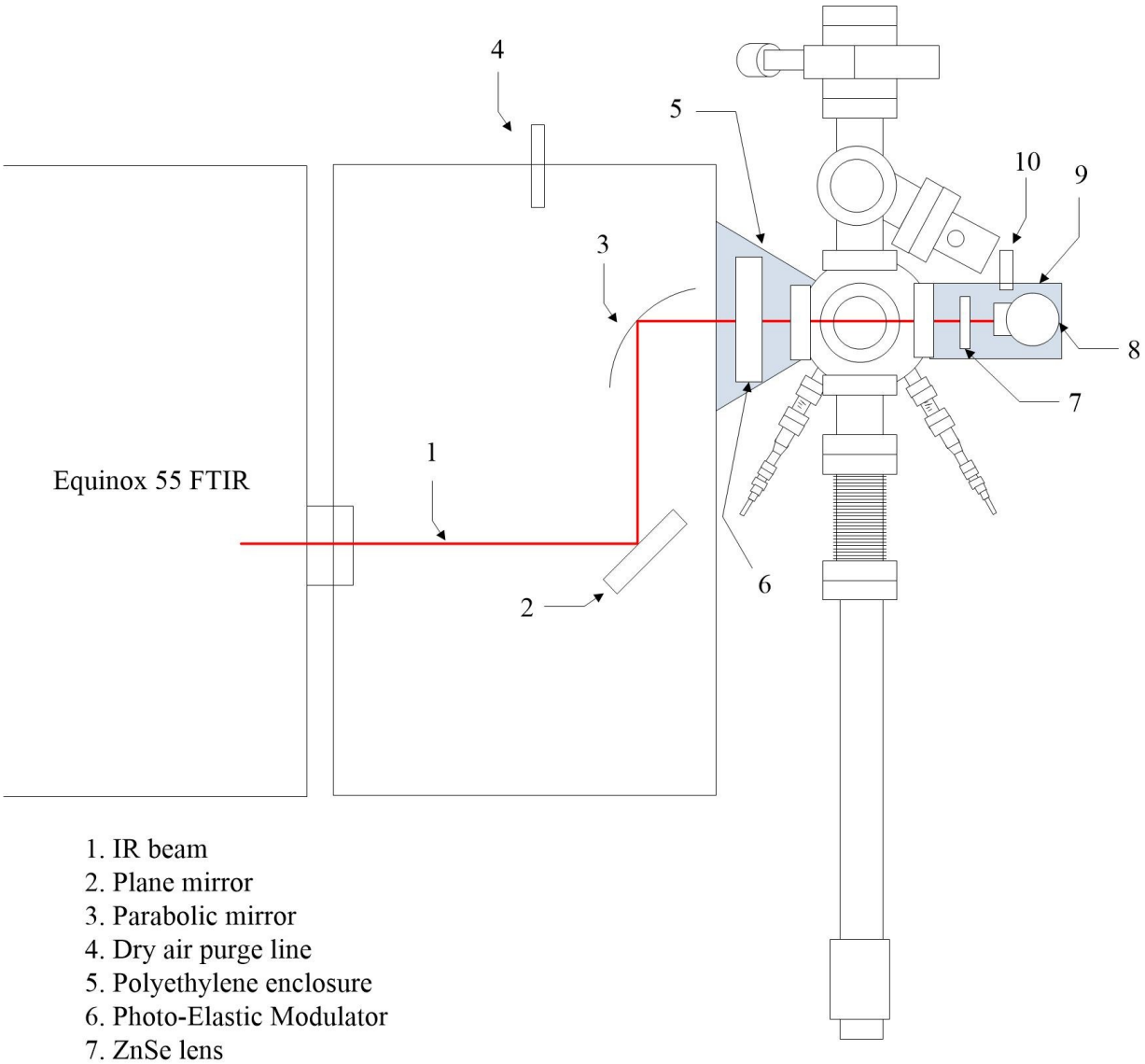

1. IR beam
2. Plane mirror
3. Parabolic mirror
4. Dry air purge line
5. Polyethylene enclosure
6. Photo-Elastic Modulator
7. ZnSe lens
8. MCT detector
9. Detector's polyethylene enclosure
10. Dry air purge line

Figure 5.12: Top view of the external beam path for the IR to the detector

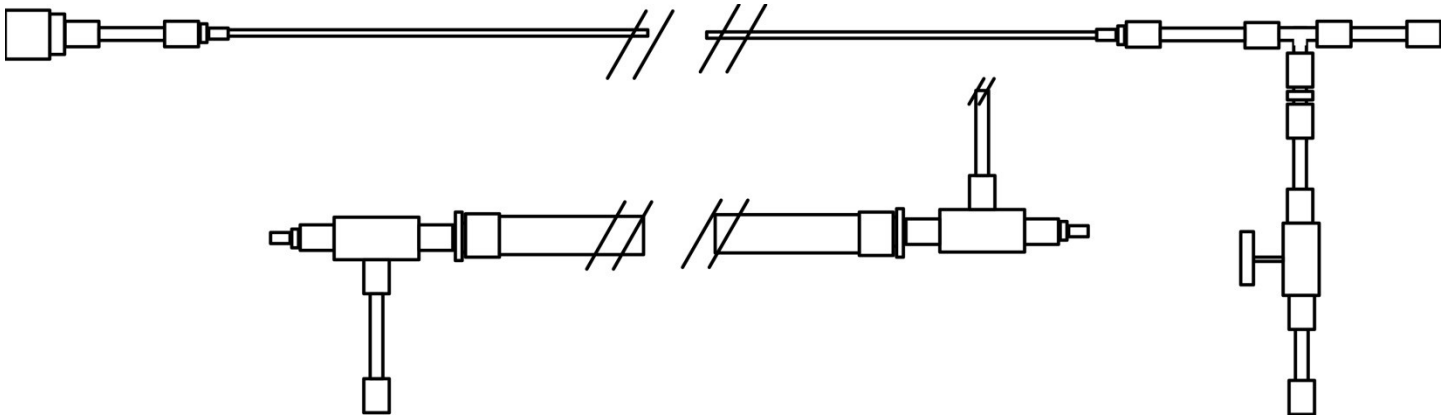

Figure 5.13: Shell and tube heat exchanger showing the shell and tube parts separated.

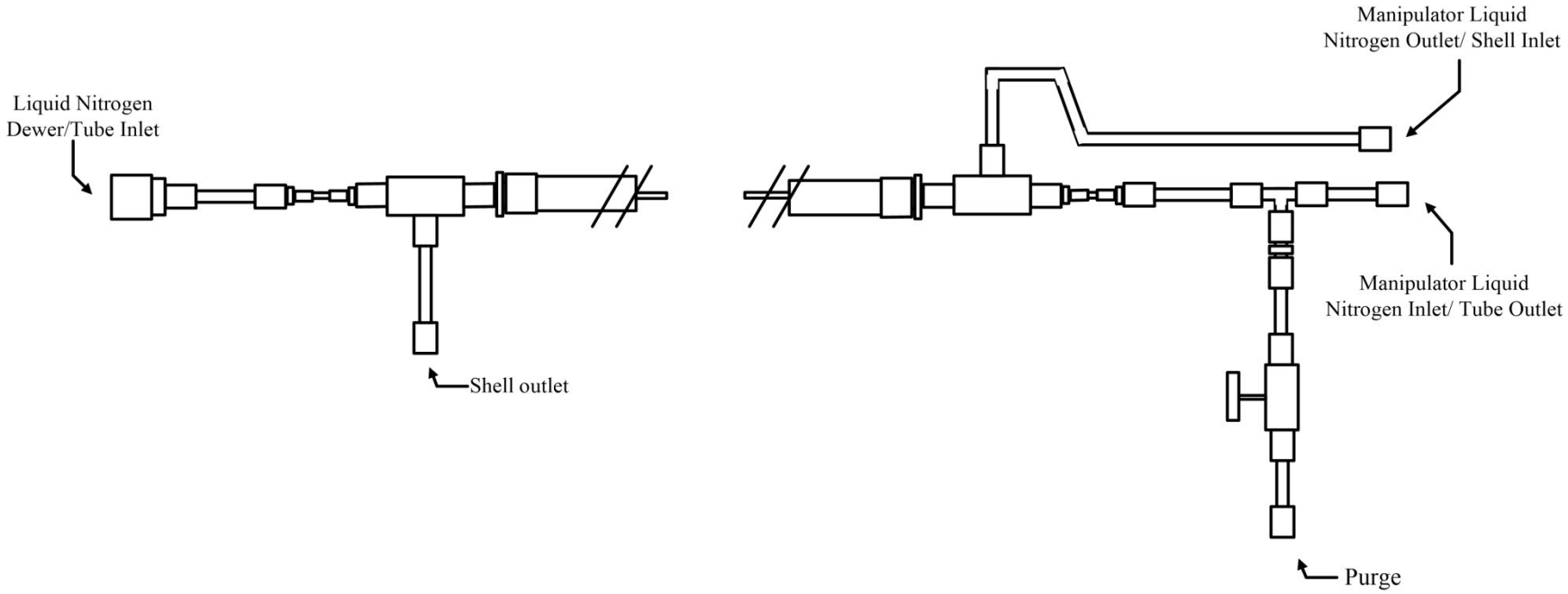

Figure 5.14: Shell and tube heat exchanger shown with labels identifying inlets and outlets.

5.7 Proof of Concept

Setting up and aligning the PM-IRRAS reactor is incredibly time-consuming and non-trivial. There are many aspects of the setup that can fail or for unknown reasons break. While working on this reactor, I have:

- Replaced the 5V and 12V power supplies and IR source for the equinox 55 IR
- Built a special computer for IR because the old computer's motherboard and hard drive died and the IR system interfaces with the computer using an ISA slot which is not present in conventional computers
- Taken the reactor apart and put back together more times than I would care to admit
- Replaced 3 pressure gauges and 1 MCT detector
- Repaired the tungsten filament twice and replaced it once
- Remounted the sample stage and aligned the fork for sample transfer too many times

Even with everything working and in place, aligning IR beam to reflect off a sample surface and into the detector is no trivial task. To ensure the highest beam intensity possible for alignment I chose to align in IRRAS mode. Using a Si(111) crystal, a reflective surface, I managed to align the system and the resulting spectrum in shown in Figure 5.15.

The heat exchanger posed much less of a problem, it worked right away with a little tightening. The minimum sample temperature capable in the chamber now is approximately 100-110 K down about 50 K from the old setup. A maximum temperature has not yet been seen in our system, the highest achieved is about 1300K.

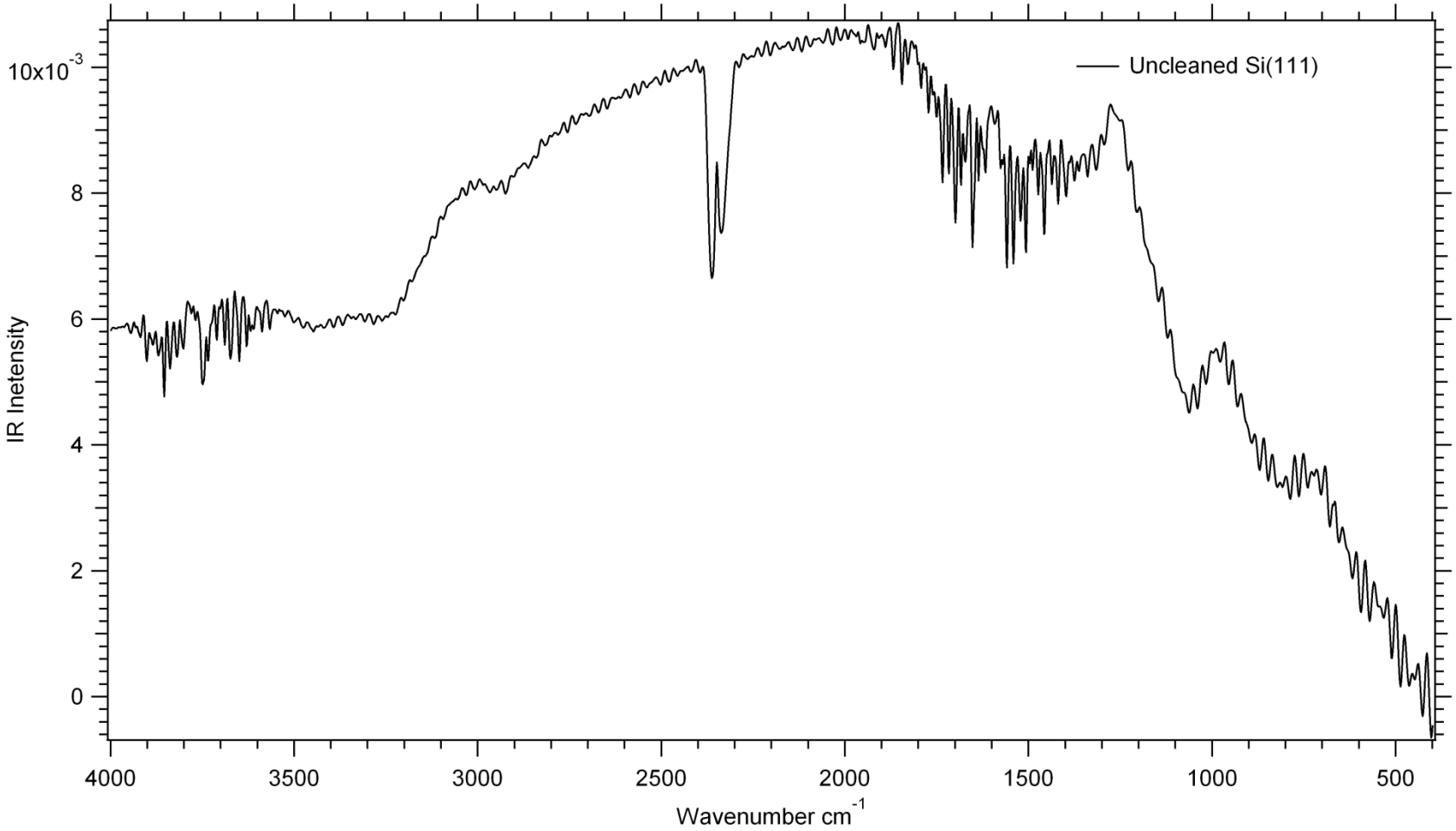

Figure 5.15: IRRAS spectrum taken in the PM-IRRAS reactor of unclean Si(111) crystal with a pressure of $1x10^{-5}$ mbar.

5.8 References

(1) Alkire, R. C.; Kolb, D. M.; Lipkowski, J.; Ross, P. N. *Advances in Electrochemical Science and Engineering: Diffraction and Spectroscopic Methods in Electrochemistry*; John Wiley & Sons, 2009.

(2) Nijholt, J. L. M. *Design of a Michelson Interferometer for Quantitative Refraction Index Profile Measurements*; Delft University Press, 1998.

(3) Wandelt, K. *Surface and Interface Science, Volumes 1 and 2: Volume 1 - Concepts and Methods; Volume 2 - Properties of Elemental Surfaces*; John Wiley & Sons, 2012.

(4) Nyquist, R. A.; Kagel, R. O. *Handbook of Infrared and Raman Spectra of Inorganic Compounds and Organic Salts: Infrared Spectra of Inorganic Compounds*; Academic Press, 2012.

Chapter 6:

Conclusion

6.0 Conclusion

Two objectives of this thesis were to fundamentally study the adsorption and decomposition of formic acid on a Co(0001) single crystal surface and highly stepped Co surface. In order to achieve this in-depth level of study, X-ray Photoelectron Spectroscopy (XPS) and Temperature Programmed Desorption (TPD) were used under UltraHigh Vacuum (UHV) conditions. From the combination of these techniques decomposition pathways were proposed for each surface. Also desorption energies and pre-exponential factors for chemical species and activation energies and pre-exponential factors for the reactions observed were reported, where applicable. The final objective of this thesis was the design and incorporation of a heat exchanger and a Photo Modulated InfraRed Reflective Adsorption Spectrometer (PM-IRRAS) reactor into the existing UHV vessel. The purpose of the reactor was for both high-pressure and UHV IR measurements, which can be used for further characterization of surface species.

On Co(0001) formic acid adsorption formic acid dissociated to formate at 160 K, molecularly desorbed from the surface above 160 K, and associatively desorbed at 236 K. Carbon monoxide desorbed from the surface at 400 K for small coverages and down to 300 K for large coverages. Water desorbed from the surface at 200 K. The dehydration reaction occurred at 140 K and 236 K. A bimolecular reaction occurred on the surface at 415-450 K, with an overall reaction of:

$$2\,HCOOH \rightarrow H_2O + C + OH + HCOO \rightarrow H_2O + CO + H_2 + CO_2 \quad (6.1)$$

The reaction has an activation energy of 44.3 ± 0.6 kJ/mol, pre-exponential factor of 0.7 ± 0.05 mbar/s and an order of -1 with respect to the surface coverages of formate and carbon and a 0^{th} order with respect to the hydroxyl.

On highly stepped Co formic acid follows similar trends as it does on Co(0001). Formic

acid molecularly adsorbs on to cobalt below 160 K. However contrary to the Co(0001) surface, a fraction of formic acid dissociates with carboxyl and formyl as intermediates, even at 110 K. The dehydration reaction occurs below 110 K. Molecular formic acid decomposes to form formate above 160 K. Water desorbs at 200 K, its normal desorption temperature on the highly stepped surface. Adsorbed hydrogen desorbs from the surface at 370 K, and adsorbed CO desorbs at 450-460 K. At 470-480 K the formate species reacts with formyl through a Langmuir-Hinshelwood mechanism with an overall reaction (2).

$$2\,HCOOH \rightarrow HCOO + HCO + H_2O \rightarrow CO + H_2 + H_2O + CO_2 \qquad (6.2)$$

Desorption energies for all the components are reported, and the kinetic parameters for the reaction have been measured as: activation energy = 147.2 ± 2.0 kJ/mol and pre-exponential factor = $10^{11.3 \pm 0.2}$ mbar/s.

The reactions of formic acid on both surfaces, although, have the same overall reaction have drastically different activation energies and different intermediates. It seems to follow that the highly stepped surface stabilizes the HCO intermediate which changes the pathway and reduces the number of molecules in rate determining step. This increases the energy required to achieve the transition state and thus increases the activation energy. Decreasing the number of molecules involved in the reaction also increases the likely hood of collisions which increases the pre-exponential factor.

A reactor with UHV and high pressure capabilities, for the characterization of surfaces using PM-IRRAS or IRRAS, was designed and a proof of concept reported within this thesis.

6.1 Future Research

As previously mentioned in the introduction chapter, in fuel cells for direct oxidation of carbon containing fuels, CO is believed to be the main poisoning species deactivating the

catalysts. Both of the reaction pathways for Co presented in this thesis, use CO as an intermediate, either as CO to react with H to form formyl or CO to dissociate to C and O. Due to CO being an intrinsic necessity for these surface reactions to occur it follows that doping a highly selective catalyst for the oxidation of carbon containing fuels with Co the resulting mixture should result in a catalyst with similar high selectivity but with reduced deactivation to the poisoning CO species. This trend has been seen in literature with Co doped platinum[1–4], palladium[5–9], tungsten carbide[10], and nickel[11] catalysts. To understand this process a number of experiments need to be conducted.

First a variable temperature IRRAS and high pressure PM-IRRAS study of formic acid decomposition on the highly stepped Co surface to both reinforce the research presented in this thesis and to provide insight into how the reaction proceeds under more realistic conditions. From this study the differences between formic acid decomposition on highly stepped Co in UHV vs. realistic pressure condition can be found. The next point of interest would be studying the reaction on a more realistic Co catalyst (i.e., Co nanoparticles).

The second study would be formic acid decomposition Co nanoparticles in UHV, similar to the studies presented in this work. Utilizing TPD, XPS, and IRRAS the mechanism of decomposition and major products can be identified and compared to the highly stepped Co and Co(0001) surfaces. This study would give a basis to understand the reaction under higher-pressures.

Next, formic acid decomposition on Co nanoparticles would be explored by variable temperature high pressure PM-IRRAS and variable temperature fixed bed catalytic reactor with mass spectrometer. From this and the previous study intermediates can be identified, a decomposition pathway found, and the effects of more realistic conditions can be seen.

From the aforementioned experiments the UHV studies identify intermediates and decomposition pathways which can then be related the high-pressure studies, thus getting the same fundamental understanding of UHV to realistic catalyst systems. This also allows for a comparison of UHV studies to realistic condition studies, as well as single crystal vs. nanoparticle studies. These studies then permit the investigation formic acid decomposition with variable doping or alloying nanoparticles of a well characterized catalyst, such as Pd, with Co and studying the alloying effects on the intermediates and decomposition pathways.

6.2 References

(1) Chen, Q.-S.; Sun, S.-G.; Zhou, Z.-Y.; Chen, Y.-X.; Deng, S.-B. CoPt Nanoparticles and Their Catalytic Properties in Electrooxidation of CO and CH(3)OH Studied by in Situ FTIRS. *Phys. Chem. Chem. Phys.* **2008**, *10*, 3645–3654.

(2) Gojkovic, S. Electrochemical Oxidation of Methanol on Pt3Co Bulk Alloy. *J. SERBIAN Chem. Soc. 68*, 859–870.

(3) Obradović, M. D.; Tripković, A. V.; Gojković, S. L. Oxidation of Carbon Monoxide and Formic Acid on Bulk and Nanosized Pt–Co Alloys. *J. Solid State Electrochem.* **2011**, *16*, 587–595.

(4) Obradović, M. D.; Tripković, A. V.; Gojković, S. L. Oxidation of Carbon Monoxide and Formic Acid on Bulk and Nanosized Pt–Co Alloys. *J. Solid State Electrochem.* **2011**, *16*, 587–595.

(5) Hosseini, H.; Mahyari, M.; Bagheri, A.; Shaabani, A. Pd and PdCo Alloy Nanoparticles Supported on Polypropylenimine Dendrimer-Grafted Graphene: A Highly Efficient Anodic Catalyst for Direct Formic Acid Fuel Cells. *J. Power Sources* **2014**, *247*, 70–77.

(6) Jang, J.-H.; Pak, C.; Kwon, Y.-U. Ultrasound-Assisted Polyol Synthesis and Electrocatalytic Characterization of PdxCo Alloy and Core–shell Nanoparticles. *J. Power Sources* **2012**, *201*, 179–183.

(7) Yin, M.; Li, Q.; Jensen, J. O.; Huang, Y.; Cleemann, L. N.; Bjerrum, N. J.; Xing, W. Tungsten Carbide Promoted Pd and Pd–Co Electrocatalysts for Formic Acid Electrooxidation. *J. Power Sources* **2012**, *219*, 106–111.

(8) Vafaei, M.; Rezaei, M.; Tabaian, S. H.; Mahboubi, F.; Haghshenas, D. F. Facile Synthesis of a Highly Active Pd/Co Bimetallic Nanocatalyst on Carbon Fiber Cloth via a Two-Step Electrodeposition for Formic Acid Electrooxidation. *J. Solid State Electrochem.* **2014**, *19*, 289–298.

(9) Morales-Acosta, D.; Ledesma-Garcia, J.; Godinez, L. A.; Rodríguez, H. G.; Álvarez-Contreras, L.; Arriaga, L. G. Development of Pd and Pd–Co Catalysts Supported on Multi-Walled Carbon Nanotubes for Formic Acid Oxidation. *J. Power Sources* **2010**, *195*, 461–465.

(10) Yin, M.; Li, Q.; Jensen, J. O.; Huang, Y.; Cleemann, L. N.; Bjerrum, N. J.; Xing, W. Tungsten Carbide Promoted Pd and Pd–Co Electrocatalysts for Formic Acid Electrooxidation. *J. Power Sources* **2012**, *219*, 106–111.

(11) Asgari, M.; Maragheh, M. G.; Davarkhah, R.; Lohrasbi, E.; Golikand, A. N. Electrocatalytic Oxidation of Methanol on the Nickel–cobalt Modified Glassy Carbon

Electrode in Alkaline Medium. *Electrochim. Acta* **2012**, *59*, 284–289.

Appendix I: XPS

The XPS system used in this body of work is a commercial unit from Specs. The system consists of an X-ray source, hemispherical analyser, PCU 300 detector unit, HSA 3500 power supply, CCX 50 water cooling control, EC 10 communication box, a XRC 1000 control unit, and Specslab2 XPS software.

The XRC 1000 control unit has a number of interlocks that prevent the X-ray source from receiving high voltage; these are to insure that if one of the main aspects of the XPS fail the X-ray source will not be damaged. The interlocks are as follows: “failure”, will light up if some hardware fails in the system; “HV lock”, will light up when the X-ray source cannot receive high voltage; “Vacuum”, will light up if the pressure in the system is too high; “Water”, this interlock is always engaged when the control box is first turned on and when the Water button is pressed the interlock will disengage if the X-ray source is receiving water at or above a flow rate of 2.5 L/min.

The following steps demonstrate how to prepare/start the system in order to take an XPS spectrum of a sample that is already in the UHV chamber.

1. Make sure the sample is grounded, either through a thermocouple or if it is grounded to the puck then through the reference potential. (See UHV section for how to ground samples)
2. Once the sample is grounded, move the sample under the hemispherical analyser, using the seeing glass at the top of the analyser to center it. Arm at (x = 69.55, y =11.5, z = 11) when arm is at room temperature.
3. Move the X-ray source in as close as possible to the sample without touching the arm, the source has aluminum foil covering the end of it that gets destroyed easily if touched.

The knob is located above the X-ray source, in-between two water hoses. It can be brought in by using your hand, but will require a ratchet to withdraw it.

4. Once the X-ray source is in, turn on the HSA 3500 power source.
5. Turn on the XPS computer and open Specslab2 (on the desktop).
6. Once Specslab2 has initialized, select "Phoibos-HSA 3500" from the drop down menu on the tool bar, or select analyser from the top menu, then select settings and then select "Phoibos-HSA 3500" from the drop down menu under analyser. If the power supply and analyser have connected, the power supply will have the CAN and HV lights lit up.

   If you receive the error message "ERROR ERROR unit 0x 1E CreateConnection failed: IClient: :OnError() from remote connection (3)" then restart the computer and the power supply and try again.

   NOTE: WHEN POWER SUPPLY HV LIGHT IS ON, THE ANALYSER IS RECEIVING HIGH VOLTAGE
7. Turn on XRC 1000 and press the water interlock button. The water interlock should turn off. If not, there is most likely a problem with water flow rate and it will need to be fixed before continuing.

   Note: There are two valves, on the east wall behind the electronics, that govern the intake and outtake of water to the cooling control unit, these need to be in the open position.
8. Press the Standby button on the XRC 1000, this allows the High voltage button to be pressed.
9. On the XRC 1000 press the High voltage button and wait till the voltage reaches 14.26 V. (During the ramp up, the box makes different high pitch frequencies as the voltage increases). The monitoring current should be 1.9 mA.

10. On the XRC 1000 press the Operate button. This increases the monitoring current to 22.9 and the emission current to 20.9. The XPS system is now ready to use.

In between scanning a sample, the system can be put into standby (X-rays off) mode by pressing the standby button on the XRC 1000. If this button is pressed and a scan is taking place or if the XRC 1000 is not on, the intensity of the data will be 0 giving a straight line.

Turning off the XPS system:

1. On the XRC 1000 press the standby button.
2. On the XRC 1000 press the High voltage button.
3. Turn off the XRC 1000
4. Disconnect the analyser and power source from the software, by deselecting "Phoibos-HSA 3500" from the drop down menu on the tool bar.
5. Once disconnected the power source should have a green blinking light, now turn off the HSA3500 power source.
6. Wait 3 minutes or so for the voltage in the X-ray source to come down before withdrawing it to around 35, using a ratchet.
7. Leave the water valves on the east wall behind the electronics, in the open position for 5 to 10 minutes after turning off the high voltage to the X-ray source, before closing them. This allows the source to cool and prevents damage.

Appendix II: STM

This section describes the basic procedure for setting up the STM system to allow for images to be taken, as well as general tips to reduce vibrational noise. Due to the variety of possible samples and surfaces, the precise details as to the settings of the STM to allow for good resolution images to be taken, cannot be given and must be found through trial and error.

Setting up the STM system (assuming sample preparation has already been completed):

1. Double check that all wires and cables on the SPM 1000 electrons, are in the appropriate spots for STM imaging. The hardware set up is detailed in the AFM/STM binder and the STM notes binder.
2. Place the prepared sample in position in the STM chamber.
3. Turn on the air to the vibration reducing legs, set the pressure to approximately 35-40 psia. The air controller is on the east wall of the lab, by the water pipes. (Not to be confused with the air controller that is above the compressed gas cylinders.)
4. Once the chamber is floating on the legs, bring down the tip elevator by turning the nob at the top of the chamber. MAKE SURE THE 3 LEGS OF THE TIP HOLDER LAND ON THE RAMPS OF THE SAMPLE HOLDER. Bring the tip down until the whole thing is resting on the sample holder. If you continue to bring the tip down after the tip has landed the legs can be crushed and broken.
5. Turn on the SPM 1000 control electronics and computer, if not already on, and open the RHK SPM software, located on the desktop labelled STM. The software will prompt you with editing the notes that will be attached to the saved image files, note this does not change the file name, only the note that will appear in the image info.
6. On the control electronics, set the Z offset to 0; the X and Y slopes to 5; the set point to 2;

the bias to a relatively high voltage, 5 V is usually a good starting point if unsure. On the computer desk there is a small grey box with a nob and X, Y, and Z labels, make sure the nob is pointing to the Z. This box controls in what direction the tip controller moves. Z is up (positive) and down (negative); Y is perpendicular to the Position Sensitive Device (PSD), positive moving away from the PSD and negative moving towards; X is the parallel to the PSD, positive moving to the right of the PSD and negative moving to the left. Figure 1 is a diagram of the Tip holder and the X and Y axis'.

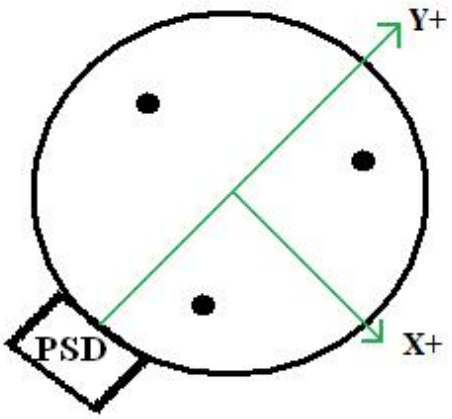

Figure 1: PSD and relative X and Y axis'

7. On the computer, left click background or press F1 to bring up the menu, click Tip approach, and then click approach. During the approach, make sure all the legs are moving down the ramp and that the elevator is low enough to not interfere with the approach. If the elevator is too high stop the approach, lower the elevator, and then continue the approach.

Once the tip approach is complete, the system is ready to take images.

In order to achieve good resolution the vibrational noise should be on the order of fA. To check the noise level of the system, a FTT noise spectrum must be taken. The FTT noise

spectrum is located in the spectroscopy menu, under the FTT tab. If the noise spectrum is too high the following list contains a number of options to reduce the vibrations:

- If there is a large spike in the spectrum between the frequencies of 0 and 10, it means the vibration reducing legs are not functioning properly. Double check that the legs are actually floating, if they are stop the air flow and re-center the legs. The legs tend to move slightly during normal chamber operations.
- Turn off the water cooling system, which is located at the far west wall of the lab.
- Turn off the power to the electronics rack, where the XPS control system is located.
- Turn off the pressure gauge in the STM chamber.
- CLOSE THE GATE VALVE; turn off the analysis chamber and the load lock pumps. Once the pumps have spun down, close the valve on the roughing pump for the analytical chambers turbo pump. This will make the chambers running off the ion pumps alone.
- Turn off the air conditioning in the lab. The air conditioning in the lab pressurizes the ceiling and then cascades down through the vents. The vents, as of August 2012, are positioned above the chamber causing the air to hit the chamber and the collisions cause vibrations when taking atomic resolution images. (This problem should be fixed in the near future.)
- Removing any unnecessary attachments to the chamber. (i.e., the liquid nitrogen connector or dry air tube.)

If all of the above suggestions did not reduce the noise level low enough, then running the system on weekends or after 5:30 pm on weekdays can help reduce the noise caused by the

building's electronics.

In order to put the chamber back under full pumping power, turn on all the pumps and open the valve of the roughing pump. Wait for about 10 hours, ideally longer, and then open the gate valve.